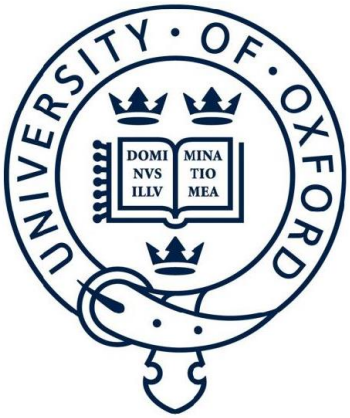
Investigating Loading Programmes for Tendon Tissue Engineering



Iain L. Sander
1201749

St. Peter's College
University of Oxford

Research Supervisors: Prof. Pierre-Alexis Mouthuy,
Dr. Julie Stebbins, and Prof. Andrew Carr

Date Submitted: Michaelmas 2020

This document is submitted to the Nuffield Department of Orthopaedics, Rheumatology, and Musculoskeletal Sciences (NDORMS), in partial fulfilment of the requirements for the degree of Master of Science by Research in Musculoskeletal Sciences.

Acknowledgments

I would like to express appreciation to my supervisors for their mentorship and consistent support throughout this research project. Andy – thank you for always having an open door and for the valuable insight you offered to the project. Your wisdom enhanced the clinical relevance of my work. Julie – I am so grateful to you for your immense technical expertise and for all the time and energy you put into helping develop my project. It was a privilege to collaborate with a world-leading expert in motion analysis and I will look back fondly on my time with you in the Oxford Gait Lab. Pierre – without you, none of this would have been possible. Thank you for giving me the opportunity to come to Oxford and take part in a cutting-edge research project. Your ability to think outside the box, take meaningful risks, and foster cross-disciplinary partnerships[1] provided me with a unique and wonderful academic experience. It was very rewarding to conduct research under your supervision.

This thesis is a result of the contributions of many people, to whom I would like to express my deepest gratitude. I would like to thank the wonderful team at the Oxford University Hospital Gait Laboratory (especially Amran S., Mike C., Andy L., and Julie W.), for helping to train me in using facility's equipment, troubleshooting and for providing a fun work environment. I am very grateful to James Fisk and David Salisbury in the IBME workshop and David Russell from Engineering Sciences for their help in designing and fabricating components for the humanoid robot. My lab mates in the Mouthuy Soft Tissue Engineering Research Group provided valuable feedback throughout the project and I am grateful to them for the time we spent together in Oxford.

Finally, I would like to dedicate this thesis to my family for their love and encouragement as I pursued my studies in Oxford. A special thanks goes to Dr. Rebecca Brassington, whose unwavering support has helped me stay grounded and motivated throughout the course of this research project.

[1] The research presented in this thesis contributes to the "Humanoid Bioreactor Project", a cross-disciplinary partnership which investigates the potential of musculoskeletal humanoid robots as a platform for biomedical applications. My research was generously supported by EPSRC Grant # EP/S003509/1 and the Rhodes Trust.

Abstract

Rotator cuff injuries are the most common cause of shoulder pain in adults and are growing in prevalence due to an aging demographic. These injuries present a substantial socio-economic burden. Despite a high prevalence of rotator cuff damage and symptoms, treatment outcomes are not promising; it is estimated that upwards of 40 % of rotator cuff repairs fail within the first few months post-operatively due to poor tissue healing. Development of engineered tendon grafts for clinical use is a promising strategy to address this growing challenge. To produce clinically relevant grafts, advanced bioreactor systems are needed.

This thesis presents a novel approach to develop physiologically relevant tendon grafts for eventual clinical application, using an advanced humanoid bioreactor platform to provide mechanical stimulation. The main objectives of this work were to investigate whether the humanoid robot could replicate the kinematic and kinetic profiles experienced by the supraspinatus tendon *in vivo* and whether loading from the humanoid robot could be effectively transmitted to scaffold material for growing tendon tissue.

To achieve the first objective, a motion study was conducted which involved the humanoid arm replicating abduction/adduction tasks that a group of 40 healthy human participants completed. Results from the motion study indicated that the humanoid arm was capable of replicating the kinematic profile or the kinetic profile of human participants during task completion, but not both simultaneously. The motion study helped identify future areas of development for the humanoid arm and further potential applications for musculoskeletal humanoid robots, such as implant testing.

Digital image correlation was used to accomplish the second objective. This investigation indicated that the humanoid robot is capable of providing strain ranges to the scaffold that have been shown to result in optimal tissue growth. The average strain values reported in this study were also within the range reported in studies examining supraspinatus deformation during abduction/adduction movements *in vivo*. Limitations associated with digital image correlation for characterisation of biological samples were discussed in this section.

This study represents a first step in exploring musculoskeletal humanoid robots as a platform for tendon tissue engineering. Although more work is necessary to enhance the humanoid model and further assess the viability of this strategy for development of clinically useful tendon grafts, the humanoid robot presented in this study has demonstrated the potential to overcome limitations associated with current bioreactor systems. This research has the potential to benefit individuals, healthcare systems, and society, by improving patient outcomes and quality of life following shoulder injury, thereby reducing the overall burden of tendon disease.

Table of Contents

Acknowledgments i
Abstract ii
List of Figures vi
1. Introduction 1
1.1 Clinical Context to Research 2
1.2 Thesis Goals and Overview 3
1.3 Outline of Thesis 4
2. Literature Review and Technical Background 5
2.1 Tendon Tissue and Shoulder Anatomy 6
2.1.1 Composition of Tendon Tissue 6
2.1.2 Tendon Structure and Biomechanical Properties 7
2.1.3 Cellular Response to Mechanical Stimulation in Tendon Tissue 9
2.1.4 Cellular Response to Mechanical Stimulation in Tendon Tissue 10
2.1.5 Overview of Shoulder Anatomy 12
2.2 Overview of Rotator Cuff Disease and Management 14
2.2.1 Epidemiology and Aetiology of Rotator Cuff Disease 14
2.2.2 Risk factors for Tendinopathy 16
2.2.3 Tendon Healing 17
2.2.4 Rotator Cuff Disease Management 19
2.3 Tendon Tissue Engineering 24
2.3.1 Overview of Tendon Tissue Engineering 24
2.3.2 Effect of Scaffold and Cell Type on Mechanical Environment 28
2.3.3 Provision of Loading by Bioreactors 29
2.3.4 Summary of Current Methods in Tendon Tissue Engineering 31
2.3.5 Musculoskeletal Robots for Tendon Tissue Engineering 32
2.4 Technical Background 33
2.4.1 Upper Extremity Motion Analysis 33
2.4.2 Upper Limb Musculoskeletal Modelling 38
2.4.3 Digital Image Correlation for Musculoskeletal Tissue Engineering 41
2.5 Chapter Summary 44
3. General Materials and Methods 45

3.1 Humanoid Robot 46
3.1.1 Original MSK Robot Shoulder 46
3.1.2 Joint and Actuator Modifications 47
3.2 Motion Study and MSK Modelling 51
3.2.1 Ethics Approval for Study 52
3.2.2 Study Participants for Motion Study 52
3.2.3 Equipment and Software Details 53
3.2.4 Quality Assurance and Calibration Procedures 54
3.2.5 Task Protocol 54
3.2.6 Kinematic Model 56
3.2.7 Motion Capture Data Processing 59
3.2.8 Kinetic Modelling for Human Participants 59
3.2.9 Force Measurements for Humanoid Robot 60
3.3 Analysis of Scaffolds Using DIC 60
3.3.1 Scaffold Description 60
3.3.2 Preparation for DIC 61
3.3.3 Equipment Details and Testing Protocol 62
3.3.4 Camera Setup and Calibration 63
3.3.5 Evaluation and Data 64
3.3.6 Validation 64
3.4 Statistical Analysis 65
4. Evaluation of Musculoskeletal Humanoid Robot as a Platform for Rotator Cuff Tendon Tissue Engineering 66
4.1 Introduction 67
4.2 Methods 69
4.2.1 Robotic Shoulder and Joint Configurations 69
4.2.2 Ethics Approval 69
4.2.3 Study Participants 69
4.2.4 Equipment and Software Details 69
4.2.5 Quality Assurance 69
4.2.6 Task Protocol 69
4.2.7 Kinematic Model 69
4.2.8 Human Force Data 69

4.2.9 Humanoid Force Data 69
4.2.10 Data Analysis 70
4.2.11 Statistical Analysis 70
4.3 Results 70
4.3.1 Actuator Configuration, Structure and Dimensions of System 71
4.3.2 Kinematic Profile 72
4.3.3 Comparison of Kinetic Profiles 78
4.4 Discussion 83
4.4.1 Interpretation of Key Findings 83
4.4.2 Implications of Key Findings 86
4.4.3 Limitations of Study 87
4.5 Chapter Summary 89
5. Strain Characterisation in Tendon Tissue Engineering Scaffold 90
5.1 Introduction 91
5.2 Materials and Methods 93
5.2.1 Robotic Arm Used for Study 93
5.2.2 Description of Scaffold 93
5.2.3 Scaffold Preparation for DIC 93
5.2.4 Data Collection and Evaluation 93
5.2.5 Validation of DIC Data 93
5.2.6 Statistical Analysis 93
5.3 Results 94
5.4 Discussion and Suggested Future Research 97
5.5 Chapter Summary 99
6. Conclusion 100
6.1 Summary of Thesis 101
6.2 Summary of Findings 104
6.3 Limitations and Suggested Work 104
6.4 Closing Remarks 106
References 107
Abbreviations Used in Text 131
Appendix A. Code for Kinematic UE Modelling 132
Static Code for Human Participants 132

Dynamic Code for Human Participants 135
Static Code for Humanoid Arm 138
Dynamic Code for Humanoid Arm 140
Appendix B. Pipeline for Collection and Analysis of Motion Study Data 142
Appendix C. Evaluation of MSK Model 143

List of Figures

Figure 1: Morphology of cells within tendon tissue. 6
Figure 2: Hierarchical structure of tendon tissue 7
Figure 3: Characteristic stress-strain curve for tendon tissue.. 8
Figure 4: Curves demonstrating the relationship between stress and strain for creep (left) and stress relaxation (right). 8
Figure 5: Mechanotransduction pathway in tendon tissue. 11
Figure 6: Joints and skeletal structure of the shoulder. 12
Figure 7: Posterior (left) and anterior (right) views of the rotator cuff tendons. 13
Figure 8: Generalised schema illustrating components commonly included in current tendon tissue engineering systems. 24
Figure 9: Humanoid musculoskeletal robots currently in use. 33
Figure 10: Inverse dynamics musculoskeletal modelling pipeline. 39
Figure 11: Workflow for DIC analysis of biological specimens. 43
Figure 12: Key components of Roboy arm-shoulder system 47
Figure 13: Configuration of actuating ‘tendon’ lines for the original joint on the MSK humanoid arm. 48
Figure 14: Adaptation of Roboy arm-shoulder system using clinical implant. 49
Figure 15: Reverse shoulder configuration. 50
Figure 16: Modified shoulder joint presented by Mouthuy et al. for tendon tissue engineering applications. 51
Figure 17: Equipment used in motion study. 53
Figure 18: Object used for calibration procedure and designation of capture volume origin. 54
Figure 19: Marker placement protocol used in study 58
Figure 20: Bioreactor chamber scaffold and attachment to 3D printed shoulder. 61
Figure 21: Speckle pattern applied to scaffold filaments. 62
Figure 22: Experimental Setup for DIC strain evaluation 63
Figure 23: Example of defined calibration target for system. 64
Figure 24: Joint configurations implemented in this study. 71
Figure 25: Kinematic trajectory plots for the slow movement tasks using the original ball and socket joint configuration. 73
Figure 26: Kinematic trajectory plots for abduction to 30^{o} in scapular plane, measured in degrees 75
Figure 27: Kinematic trajectory plots for abduction to 90^{o} in scapular plane, measured in degrees 76

Figure 28: Supraspinatus force profile for abduction to 30º in scapular plane, measured in Newtons (N). 79
Figure 29: Supraspinatus force profile for abduction to 30º in scapular plane, measured in Newtons (N). 80
Figure 30: Supraspinatus force values from abduction to 30º task completed over 2 s.. 81
Figure 31: Supraspinatus force values from abduction to 90º task completed over 6 s.. 82
Figure 32: Strain map taken midway through an abduction-adduction trial. 94
Figure 33: Comparison of tensile stress applied to tissue construct and resultant strain. 95
Figure 34: Results from Tensile Testing.. 96
Figure 35: Differences in supraspinatus muscle force during task completion 146
Figure 36: Supraspinatus muscle force as a function of muscle recruitment 147

List of Tables

Table 1: Movements of the shoulder 13
Table 2: Risk factors described in literature for developing tendinopathy 16
Table 3: Description of phases in wound-healing process 17
Table 4: Exercise programme based on recent guidelines for shoulder rehabilitation 22
Table 5: Recent tendon tissue engineering experiments involving provision of mechanical stimuli 26
Table 6: Comparison between native tendon tissue and engineered tendons from studies 31
Table 7: Techniques currently available for use in human motion capture 37
Table 8: List of exercises completed in motion study 55
Table 9: Marker locations used for motion study 57
Table 10: Comparison of the original MSK arm-shoulder robot joint and adult human shoulder anthropometric parameters. 72
Table 11: Kinematic outcome variables from slow movement 30º abduction/adduction task.. 74
Table 12: Kinematic outcome variables from slow movement 90º abduction/adduction task.. 74
Table 13: Kinematic outcome variables from 30º abduction/adduction task used to evaluate implant performance.. 77
Table 14: Kinematic outcome variables from 90º abduction/adduction task used to evaluate implant performance. 78
Table 15: Kinetic outcome variables from 30º abduction/adduction task used to evaluate implant performance.. 81
Table 16: Kinetic outcome variables from 90º abduction/adduction task used to evaluate implant performance.. 82
Table 17: Outcome parameters for movement trials. 96
Table 18: Differences in peak and average supraspinatus muscle forces as a function of recruitment synergy.. 147
Table 19: Peak and average GH joint reaction forces obtained from the AMS during task completion .. 148
Table 20: Peak and average GH joint moments obtained from the AMS during task completion 148
Table 21: Peak and average muscle force estimates obtained from the AMS during task completion 149

1. Introduction

1.1 Clinical Context to Research

Connective tissue injuries are a common cause of mobility related impairment and are increasing in prevalence with an aging demographic and growing rate of obesity [1]. Rotator cuff tears are of particular interest, given that they are present in approximately 15 % of the population between 50-60 years of age, increasing to upwards of 30 % of the population over 70 years of age [2, 3]. Tears most commonly occur in the supraspinatus tendon [4]. These injuries present a significant socio-economic burden, with individuals suffering from rotator cuff tendon tears taking significant amounts of sick leave to recover following surgery and reporting lower productivity upon return to work [5]. The lifetime cost of a rotator cuff tear to society has been estimated at $ 20,000-100,00/patient in the United States (US) and £ 20,000-30,000/patient in the United Kingdom, translating to billions of dollars in healthcare costs [5, 6].

With upwards of 250,000 rotator cuff surgeries performed per year in the USA alone, patient outcomes remain poor, with upwards of 40 % of tendon repairs failing post-operatively [7-11]. Revision surgeries further compound the social and economic impacts of rotator cuff tendon disease. Given the slow process of tendon healing and a lack of satisfactory surgical and medical therapies currently available for patients, there is growing need for the development of novel treatment options outside the realm of surgical repair.

A promising repair strategy is the development of engineered tendon grafts for clinical use. Tendon tissue engineering involves using a bioreactor system to generate tissue *in vitro* using patient cells, scaffolds, and mechanical stimulation [12]. A widely held view in this field is that viable bioreactors should successfully re-create the mechanical environment of native tendon tissue. While work in this field has progressed to optimise cell culture and scaffold materials for tissue engineering, the lack of bioreactor systems that provide physiologically relevant loading has been a major gap in the development of engineered constructs for clinical use. To address this challenge, a translational approach to tissue engineering involving the use of a musculoskeletal robot humanoid bioreactor has been proposed, hypothesising that by mimicking natural multi-axial stressors on tendons in the human body to stimulate tendon cell proliferation, more optimal tissue grafts will eventually be available for clinical use [13].

1.2 Thesis Goals and Overview

My thesis comprises two sub-tasks which work towards achieving the overarching goal of developing a humanoid bioreactor system capable of performing novel physiologic loading programmes in tendon tissue engineering.

Sub-Task 1: Motion analysis to optimise and validate loading programmes

When optimising the humanoid bioreactor to adequately simulate a human shoulder, numerous parameters such as range of motion, movement speed, tensile force, and joints involved in effectuating movement need to be considered. The purpose of this task is to use motion analysis to determine whether the robotic arm used for providing mechanical stimulation adequately replicates the forces and motion profile of a healthy adult human shoulder. To limit the scope of this task, the motion study specifically examines abduction in the scapular plane. Abduction movements were of particular interest as they are predominantly actuated by the supraspinatus, which is the most commonly injured rotator cuff tendon.

Sub-Task 2: Develop method to quantify strain of samples in the bioreactor chamber

Given that tendon tissue is highly responsive to mechanical cues, whereby excessive or insufficient strain results in suboptimal tissue development, being able to quantify and measure strain is crucial. Although tendon tissue engineering has moved towards real-time strain measurement, most current studies do not adequately account for non-uniform strain distributions within their scaffolds. The objective of this task is to investigate a method for approximating multiaxial non-uniform strain distributions in real-time for the humanoid bioreactor system.

Using these sub-tasks, two key hypotheses of this thesis will be evaluated: a). That the humanoid arm provides similar movement and force profiles to those experienced by the supraspinatus tendon *in vivo*; and b). the method used for approximating strain in the tissue construct will report average strain values consistent with conventional methods of strain characterisation.

1.3 Outline of Thesis

The content discussed in each chapter of this thesis has been outlined below:

Chapter 2: This chapter consists of four sections: an overview of tendon structure and shoulder anatomy, the clinical context of rotator cuff disease and management, tendon tissue engineering practices, and a technical background to the technology used in chapters 4 and 5 of this thesis.

Chapter 3: This section describes the robotic arm used in this thesis as well as general materials and methods used for the motion study and strain characterisation study (chapters 4 and 5, respectively).

Chapter 4: Results from the motion study, used to validate whether the humanoid musculoskeletal robot adequately represents the kinematic and kinetic profile of a healthy human shoulder during a series of abduction movements in the scapular plane, are presented here. The subsections to this chapter include a discussion of kinematic outputs obtained from the Vicon Nexus™ motion capture software and *in vivo* loading estimates for human participants, obtained using a commercially available MSK modelling programme developed by AnyBody™ Technology.

Chapter 5: This chapter presents results from an investigation using Digital Image Correlation (DIC) to characterise strain within scaffolds on the humanoid arm as it undergoes loading. This study discusses the validity of DIC for strain characterisation by comparing the results from this method with those obtained using a conventional method of strain measurement.

Chapter 6: Contributions to this field of research, limitations to the work presented in this thesis, and suggested future work are presented here. This chapter provides concluding remarks for this thesis.

Bibliography and Appendices: Presented following chapter 6.

2. Literature Review and Technical Background

2.1 Tendon Tissue and Shoulder Anatomy

2.1.1 Composition of Tendon Tissue

Tendons are approximately 70 % water weight and 30 % dry weight. Collagen comprises 85 % of this dry weight, with Type I collagen making up 90 % of this total content and the majority of the fibril subunits, while Type III collagen makes up approximately 10 % of the collagen within the tendon and serves to assist in formation of cross-links between fibrils [14, 15]. These rigid structural proteins provide the tendon with linear alignment and tensile strength [16]. Other key components of tendon include elastin, which serves to help tendons store energy from kinetic loads and deform following stress [15] and proteoglycans, whose negatively charged side chains attract water and positively charged ions to the tendon tissue, thus contributing to the tissue's viscoelastic and compressive properties [17]. The chemical composition of tendon varies by anatomic location and within local areas of the tissue.

The primary cells constituting tendon tissue are tenocytes, a fibroblast class which produces the structural proteins and extracellular matrix. Tenocytes reside within the fascicles and form networks with adjacent cells via gap junctions [18]. These communication networks enable tenocytes to react to external stimuli, such as inflammatory markers and mechanical forces, and correspondingly adapt production of structural proteins and extracellular matrix. It is worth noting that there are other cell populations residing within tendon tissue which remain poorly understood (Figure 1) [19].

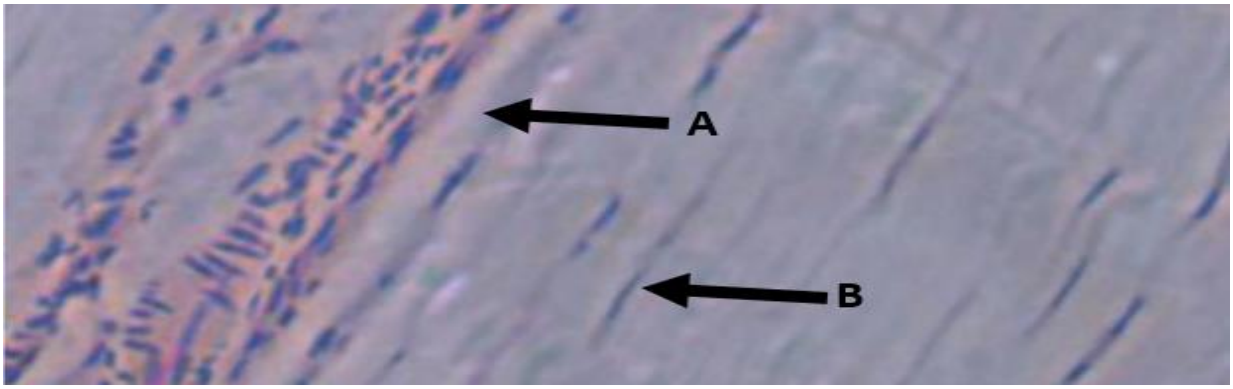


Figure 1: Morphology of cells within tendon tissue. The more densely packed cells indicated by arrow A exist within the interfascicular matrix and are poorly defined in function. The elongated cells indicated by B are tenocytes (adapted from Thorpe and Screen) [15].

2.1.2 Tendon Structure and Biomechanical Properties

Tendons are the viscoelastic connective tissues which attach muscle to bone. Hierarchically structured, tendon tissue consists of collagen fibres tightly organised in parallel, linearly arranged fascicles (Figure 2). These fascicles are held together by a sheath composed of two layers: a synovial membrane and an external fibrous layer. This sheath maintains lubrication of the tendon, provides flexibility to the tendon, and prevents fascicles from losing their configuration [14].

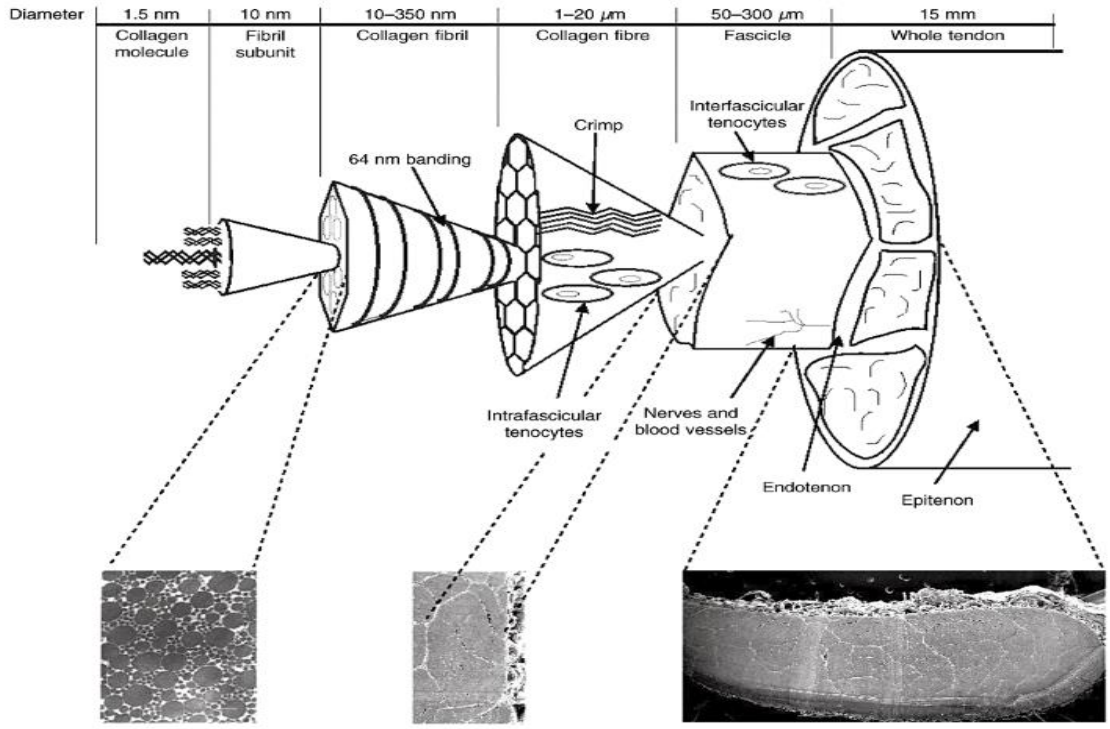


Figure 2: Hierarchical structure of tendon tissue (reproduced from Thorpe et al.) [20]

Tendon tissue demonstrates anisotropic properties, given that its response to stress is directionally dependent. While tendon tissue has poor resistance to transverse and shear stress [14], the tightly organised linear structure of tendon tissue enables it to withstand longitudinal tension over 1000 times greater than its resistance to shear and transverse stress [21]. Tendons can therefore effectively transmit muscular forces to the skeletal system for locomotion with minimal deformation. When a longitudinal stress is applied to tendon tissue, there are three distinct regions that can be observed on a stress-strain curve, as given in Figure 3.

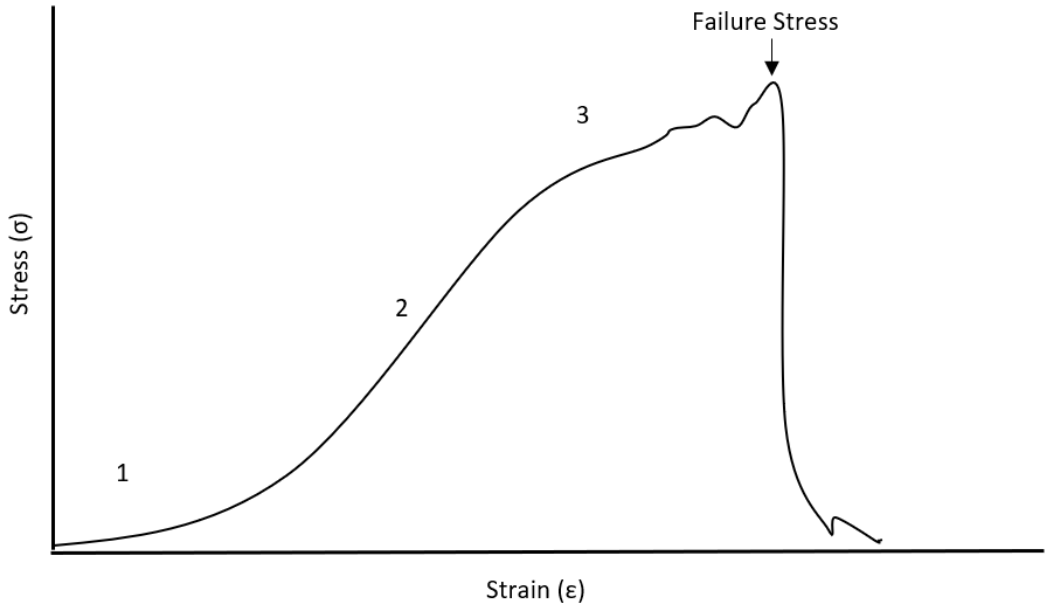


Figure 3: Characteristic stress-strain curve for tendon tissue. Region '1' is the toe region, whereby appreciable strain results from minimal stress loading. Structurally, this represents the crimped collagen fibres within the fascicles being stretched. Once the collagen fibres are fully straightened, the tendon fascicles experience linearly proportional linear deformation, as described by region '2'. Following continued stress, inelastic deformation (region '3') of the tendon occurs until eventual rupture of the tendon (failure stress) [14].

Elastic materials exhibit an immediate linearly proportional strain when stress is applied, whereas viscous materials resist strain linearly as stress is applied. Given that tendon tissue has components that contribute to both elastic and viscous behaviours, tendon is characterised as a viscoelastic material. This viscoelasticity enables tendon tissue to exhibit the mechanical properties of stress relaxation and creep. Stress relaxation occurs when stress gradually decreases over time in response to a constant deformation. Creep is defined by increasing deformation of a material that is kept under a constant stress. These behaviours are shown in Figure 4.

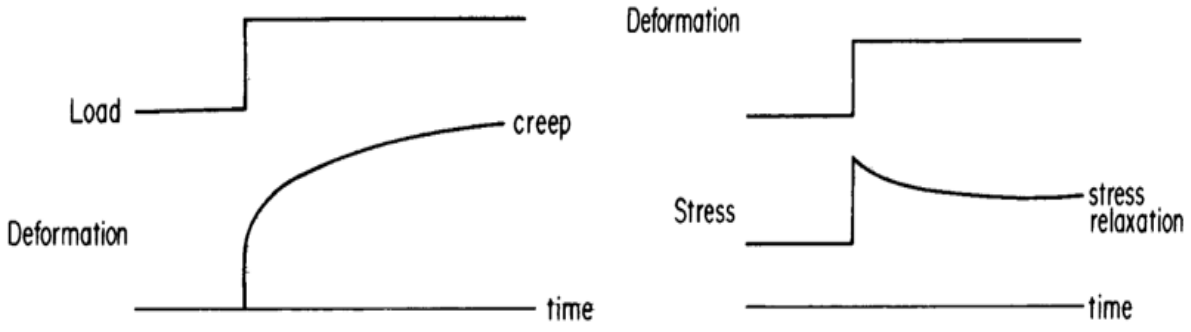


Figure 4: Curves demonstrating the relationship between stress and strain for creep (left) and stress relaxation (right) (reproduced from Kirkendall and Garrett) [14].

In addition to force transmission for locomotion, certain tendons have a specialised role of facilitating kinetic energy storage and transfer, thus improving movement efficiency during locomotion. Given these two distinct roles, the mechanical properties of energy storing tendons and positional tendons have notable differences. Energy storing tendons, such as the Achilles tendon, can experience strains upwards of 10-12% during use, whereas positional tendons, such as those of the rotator cuff, experience strains around 1-3% during use [14, 16, 22]. Furthermore, studies of equine tendon tissue have demonstrated that positional tendons experience failure when exposed to stresses and strains of 120-200 MPa and 15-22%, respectively, whereas energy storing tendons fail at stresses and strains of 90-145 MPa and 18-28%, respectively [15, 19, 20, 22].

Given these differences in mechanical properties, variations in molecular composition and structural configuration exist which assist these tissues in completing their respective roles. To behave in a more elastic manner, energy storing tendons tend to have greater proteoglycan content, more elastin, and less cross-linking of collagen fibres [16]. Furthermore, energy storing tendons have been shown in literature to have a slight helical structure to their fascicles [23], thus assisting in storage of elastic potential energy.

2.1.3 Tendon Loading *In Vivo*

There are numerous limitations to *in vivo* imaging of tendon tissue, such as the inability to observe tendon properties at a scale smaller than the tissue level, a lack of accuracy for complex movements, and limited availability of software programs that provide quantitative estimates of deformation [24]. Despite these limitations, *in vivo* characterisation plays an important role in validating the results of *ex vivo* mechanical studies. Box 1 provides case studies of *in vivo* tendon characterisation done using 2D ultrasound strain elastography (2D-USE).

Box 1. Case studies characterising tendon loading *in vivo*

i). Chernak and Thelen investigated Achilles tendon tensile strain profiles under passive stretching and eccentric loading conditions. A custom-made device was used to induce plantarflexion to dorsiflexion movement consistently across participants and to ensure that the ultrasound probe did not change direction throughout the loading programme. The methodology used to collect *in vivo* ultrasound data from this study was validated in previously published work [25]. The study reported non-uniform distal deformation during both passive stretching and eccentric loading, with deep regions of the tendon consistently demonstrating larger displacement than superficial regions. Greater deformation was also noted in older participants compared to younger participants [26].

ii). Chimenti et al. assessed strain along the longitudinal axis of the Achilles tendon *in vivo*. A custom-made device was developed to ensure that the probe did not change direction throughout participant movement. Ultrasound data collected in this study were validated through comparison with calibration measurements done using a caliper. The primary findings of this study were that deep regions of the tendon tissue experienced greater deformation, with deep tissue exhibiting 4-6 % more strain than the superficial tissue across three different movement tasks involving compressive loading of the Achilles tendon [27].

iii). Kim et al. provided *in vivo* strain analysis of the supraspinatus tendon as participants completed isotonic and isometric elevation in the scapular plane. Kim et al. observed non-uniform strain profiles for both exercises, with mean peak longitudinal strains of 15.7 ± 2.4 % in the deep tissue region and 4.7 ± 0.74 % in the superficial tissue during isotonic motion and mean peak longitudinal strains of 17.03 ± 1.69 % in the superficial region and 3.42 ± 0.49 % in the deep tissue region during isometric contraction [28]. While the results from this study were compared to related cadaver studies, this investigation must be interpreted with caution as the results were reported without any validation experiments.

In vivo imaging studies demonstrate that tendon tissue deforms heterogeneously during physiologic loading. This heterogeneity may result from architectural differences within the tendon tissue that contribute to differing levels of compliance and non-uniform tensile loading *in vivo* [26].

2.1.4 Cellular Response to Mechanical Stimulation in Tendon Tissue

The interplay between mechanical stimulation, cellular response, and changes to tendon extracellular matrix (ECM) is a growing area of interest for researchers and clinicians involved in benchtop science research. As with bone and muscle tissue, tendon tissue appears to experience multiaxial loading (numerous directions of loading) and is sensitive to a variety of mechanical stimuli [29]. These mechanical stimuli are then translated to provide cues to cellular pathways which are responsible for ensuring maintenance and development of healthy tendon tissue, as shown in Figure 5.

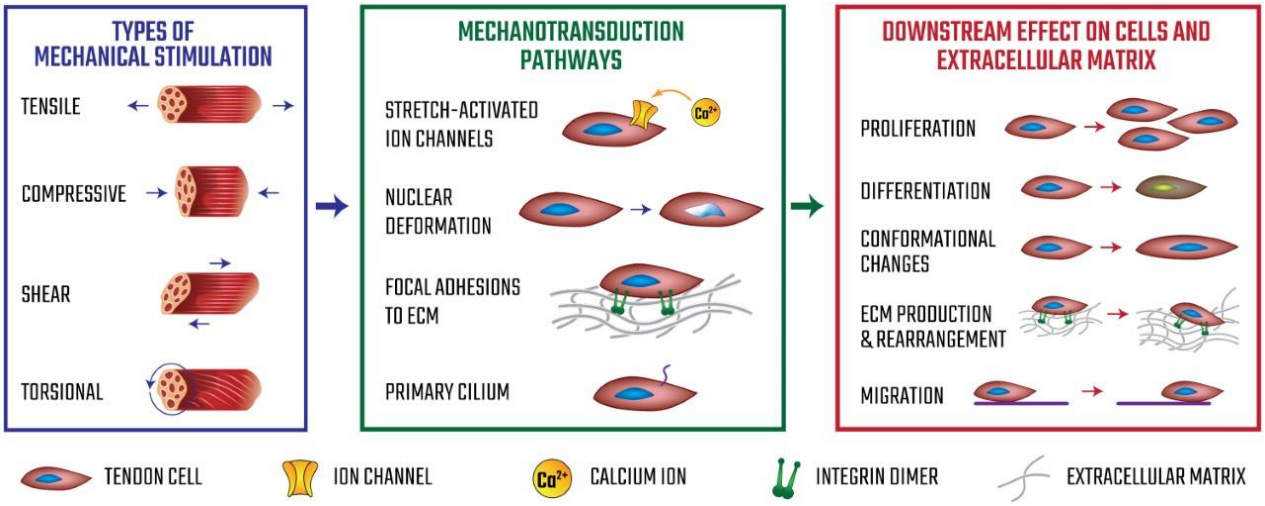


Figure 5: Mechanotransduction pathway in tendon tissue. Tendon tissue experiences a variety of mechanical stimuli during physiological loading (left), including tensile, compressive, shear, and torsional loading [29, 30]. These stimuli are then transduced into cellular cues (middle). The transduced signals upregulate various biochemical pathways, influencing important physiologic processes for tendon tissue such as proliferation, differentiation, homeostasis, ECM production, and conformational changes to tendon cells present within the tissue (right) [17, 30].

While the various cellular pathways through which mechanotransduction occurs in cells are not yet fully understood, models supported by empirical data suggest that the type and direction of mechanical stimulation will have distinct effects on tendon properties at a cellular level. Stretch-activated ion channels are sensitive to multiple types of mechanical loading, including tensile, compressive, and shear stress, and respond primarily by regulating cell volume [31]. Many types of mechanical stimulation, such as torsional, compressive, and tensile stress induce nuclear deformation. Although consequences of nuclear deformation are not fully elucidated, it is known to modulate crucial signalling pathways and influence gene expression [32]. Focal adhesions respond to changes in collagen fibre tension with downstream effects such as cellular differentiation and migration [17]. Tenocyte primary cilia are hypothesised to respond to shear stress and influence a variety of properties, including cell orientation, ECM integrity, and tissue repair [29]. Emerging research suggests that modulation of surrounding immune cells can also influence tenocyte behaviour [33]. Collectively, a growing body of research within mechanobiology suggests that a variety of multiaxial stimuli are required for healthy tendon tissue development. In consideration of mechanobiology studies, which demonstrate that tendon tissue responds

to multiple types and directions of mechanical stimulation, and *in vivo* imaging studies, which describe how tendon tissue deforms non-homogenously, it is important to closely mimic the native tissue mechanical environment for development of healthy tendon constructs.

2.1.5 Overview of Shoulder Anatomy

The clavicle, head of the humerus, and scapula constitute the skeletal structure of the shoulder. There are four joints that comprise the shoulder: the sternoclavicular joint (SC), the acromioclavicular (AC) joint, the scapulothoracic (ST) joint, and the glenohumeral (GH) joint (Figure 6). The principal joint in the shoulder is the GH joint. It is structurally described as a ball and socket joint with three rotational degrees of freedom (DoF).

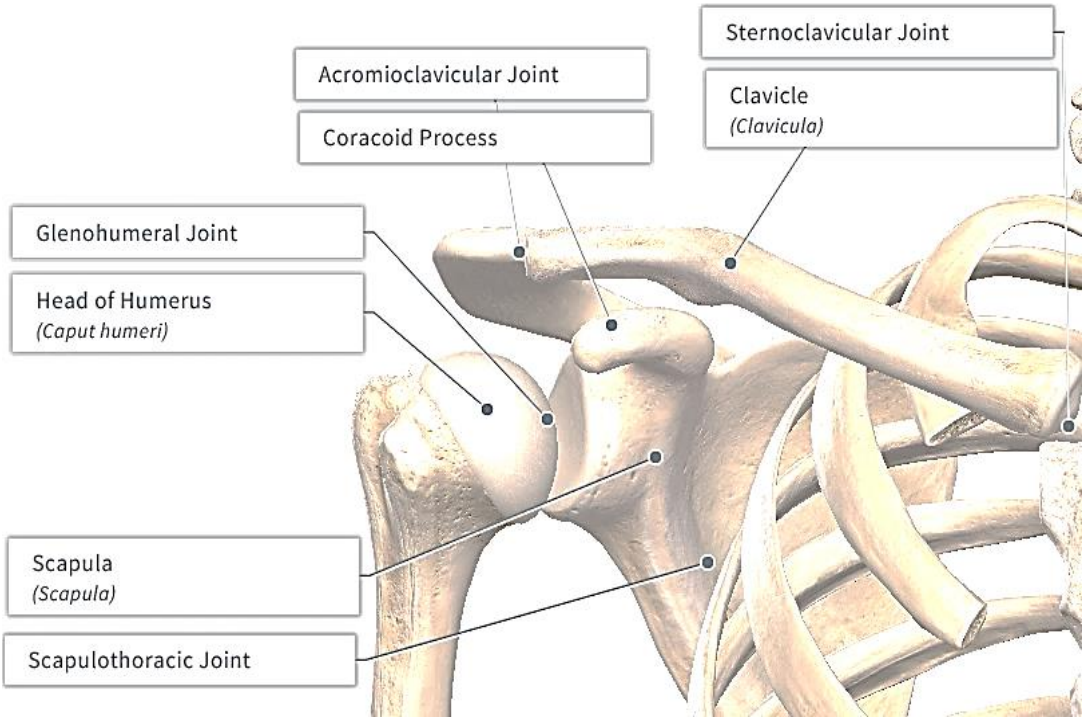


Figure 6: Joints and skeletal structure of the shoulder (reproduced from 3D4Medical) [34].

The GH joint is a shallow structure whose articulating surface consists of scapular components acting as a socket, with the humeral head fitting within the socket of the joint. Connective tissues, including the labrum, ligaments, and encapsulating structures confer stability to the GH joint. Immediately superficial to these

stabilising connective tissues lie the rotator cuff muscles and tendons. The tendons of the rotator cuff surrounding the GH joint are shown in Figure 7.

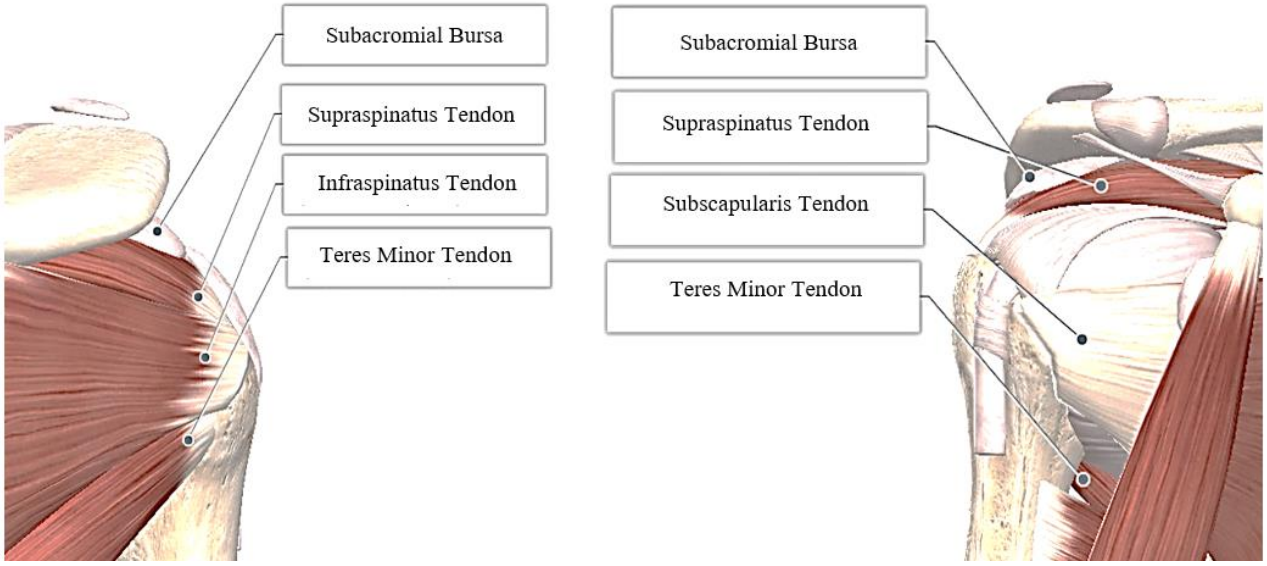


Figure 7: Posterior (left) and anterior (right) views of the rotator cuff tendons (reproduced from 34DMedical) [34].

Rotator cuff muscles function collectively to ensure stability in the GH joint throughout motion [35]. The rotator cuff muscles work alongside other muscles, including the deltoid, trapezius, and biceps brachii, to actuate the upper extremity. Different shoulder movements are described in Table 1. Although certain rotator cuff muscles are more commonly associated with specific movements – such as the supraspinatus tendon being associated with abduction in the scapular plane – it is important to note that all four rotator cuff muscles are recruited for stabilisation and movement of the glenohumeral joint [36-39].

Table 1: Movements of the shoulder. In measuring ROM (Range of Motion), the degree of movement is considered relative to an initial starting position of the arm kept at the side of the body with the dorsal aspect of the hand facing outwards [40-42].

Movement	Description	ROM	Rotator Cuff Muscles Involved
Abduction	Abduction involves moving the upper extremity laterally in the coronal plane	135-150º	Supraspinatus, Subscapularis, Teres Minor
Adduction	Adduction involves moving the upper extremity medially in the coronal plane	30-50º	Teres Minor, Supraspinatus
Flexion	Flexion involves raising the upper extremity in front of the body anteriorly in the sagittal plane	170-180º	Supraspinatus
Extension	Extension involves moving the upper extremity behind the body posteriorly in the sagittal plane	45-60º	-

Medial (Internal) Rotation	This movement involves bending the elbow 90º and moving the forearm towards the centre of the body while keeping the elbow pressed against the side of the body	75-90º	Subscapularis
Lateral (External) Rotation	This movement involves bending the elbow 90º and moving the forearm away from the centre of the body while keeping the elbow pressed against the side of the body	75-90º	Supraspinatus, Infraspinatus, Teres Minor

While the composition of tendon tissue enables it to be well-suited for load bearing, the wide ROM around the shoulder joint means that rotator cuff tendons are exposed to a range of multi-directional stresses and strains, predisposing them to degeneration and eventual failure [43].

2.2 Overview of Rotator Cuff Disease and Management

This section provides an overview of rotator cuff injury and treatment following injury. For the purposes of this review, the term 'tendinopathy' is used to refer to a broad category of disorders affecting tendons, including rupture, tendonitis, and degenerative tendon disease.

2.2.1 Epidemiology and Aetiology of Rotator Cuff Disease

Despite traditionally being viewed as an affliction primarily affecting athletes, it is now known that rotator cuff injuries are the most common cause of shoulder pain in the general adult population [44]. Rotator cuff tears present most commonly in the supraspinatus tendon [4]. In a study conducted by Tempelhof et al., approximately 13% of the population aged 50+ years in the study had a supraspinatus cuff tear, with the figure increasing to over 30% in the population over 70 years [2]. Similar results are published in later studies, demonstrating that supraspinatus tears are a significant cause of pain and debilitation in the adult population [45, 46].

While many studies have been conducted to better understand the mechanisms underlying tendon disease, its aetiology and pathogenesis are poorly understood due to its complex nature [17]. Non-traumatic tendinopathy has traditionally been described as a result of overuse and excessive mechanical stimulation. In a model developed by Archambault et al., repetitive excessive tensile stress induces degeneration in tendon matrix, leading to transient tissue weakness [47]. During this transient weakness phase, non-

reversible damage occurs until tendinopathy results. *In vitro* investigations conducted by Wang et al. and Skutek et al. on the overuse model suggest that tendinopathy occurs secondary to overstimulation, whereby excessive loading induces cell apoptosis, inflammatory cytokines at the site of injury, and degradative matrix metalloproteinase (MMP) production [48, 49].

An *in vivo* animal study conducted by Soslowsky et al. compared the biomechanical and histologic findings in rat supraspinatus tendon tissue following 1-3 months of activities leading to overuse injuries. Histologic findings included more rounded, 'chondroid' cells and fewer spindle-shaped cells, characteristically found in healthy tendon tissue, and a lack of longitudinal alignment of collagen fibres [50]. Furthermore, the elastic modulus and maximum tensile stress of supraspinatus tendon in the "overuse injury" rats were found to be significantly less than those in the "normal use" control group [50], thereby further validating overuse as a cause of tendinopathy. Altogether, *in vitro* investigations and *in vivo* animal studies have provided a reasonable case for the overuse hypothesis.

Paradoxically, under-stimulation of tendon tissue has also been described in more recent literature as another aetiology for tendon injury. *In vitro* studies from Arnoczky et al. have shown that in states of under-stimulation, tendon load bearing capability becomes reduced [51]. Mechanistically, under-stimulated tendon cells were found to upregulate genes responsible for collagenase expression, which then degraded the pericellular matrix of the tenocytes and impaired cell-matrix communication, which is necessary for physiologic mechanobiological signalling [51].

Periods of under-stimulation have also been shown to lead to morphological and functional changes to tendon tissue architecture in human studies, with increased tendon stiffness being noted within two weeks of tissue unloading [52, 53]. Collagen synthesis significantly decreases following immobilisation, further supporting the existing body of knowledge that describes the importance of mechanical loading for homeostatic collagen turnover within tendon tissue [54].

While spontaneous tendon rupture is possible, histological specimens of recently ruptured human and animal tendon often indicate longer term degradative changes in the tissue, suggesting that subclinical trauma had occurred in the tissue prior to the final incident which ultimately resulted in tendon failure [17, 55]. Current research therefore suggests that tendinopathy can occur due to excessive or insufficient mechanical stimulation and is frequently associated with chronic damage rather than acute trauma.

2.2.2 Risk factors for Tendinopathy

Given that tendon tissue is sensitive to mechanical stimulation and uses a range of mechanisms to transduce these signals into meaningful cellular actions, such as cell differentiation and tissue homeostasis, the risk factors for developing tendinopathy are multi-factorial. Established risk factors for tendinopathy have been described in Table 2.

Table 2: Risk factors described in literature for developing tendinopathy

Risk Factor:	Proposed Mechanisms of Action:
Quinolone-class antibiotic use	-Reduced collagen and glycosaminoglycan synthesis, combined with decreased cellular proliferation [56]. -Production and accumulation of cytotoxic reactive oxygen species (ROS), leading to tenocyte apoptosis [57].
Long-term glucocorticoid use	-In patients using glucocorticoids for a 3+ month period, proposed mechanisms contributing to tendon rupture include deterioration of collagen via collagenase activation and decreased ability to repair tendon tissue following repetitive microtrauma [58-60].
Hypercholesterolemia	-Given that hypercholesterolemia is often associated with an inflammatory state, underlying mechanisms of tendon damage may be linked to increases in inflammatory cytokines, pro-inflammatory monocytes, and degenerative metalloproteinase production . -In animal models, hypercholesterolemia has been linked to decreased tendon repair capacity, increasing risk of failure following repetitive tensile stress [61-63]. -Paradoxically, management of hypercholesterolemia using statins can also increase risk of tendon injury. Cell experiments have shown that statin use decreases migration of human tenocytes, alters mRNA expression, and impairs their functional communication network [64].
Diabetes	-In a meta-analysis which established an association between diabetes and tendinopathy, a possible mechanism for the development of tendinopathy was tissue ischaemia due to microvascular disease [65]. -Another hypothesis put forward is that patients with metabolic syndrome tend to be in a pro-inflammatory state, thereby increasing risk of injury and reducing native tissue healing ability [66].

Genetics	-Gwilym et al. conducted a sibling study that suggested that genetics have a role in development and progression of rotator cuff tears [67]. Elements under genetic influence that might affect risk of developing a tendinopathy include differing anatomic conformations, collagen-producing gene polymorphisms, and variations in signalling gene expression, such as Tenascin-C and Tissue Growth Factor-β (TGF- β) [68].

Proteomic analysis of tendon matrix has shown that distinct differences exist between young, healthy tendon tissue and older tissue. Decreased levels of proteins that are required for collagen fibre genesis and force transfer have been noted [69]. Aging tendon tissue is also found to have a greater degree of cross linking, thereby reducing the tensile properties of the tissue, and increasing risk of tendon disease from damage acquired through overuse [17, 70]. Decreased levels of proteins with anti-inflammatory and anti-apoptotic roles have also been observed in aging tendon tissue [69]. This in turn suggests that aged tendon tissue has reduced ability to self-repair following microtrauma, thereby increasing risk of tendon injury.

2.2.3 Tendon Healing

Like other soft tissue injuries, the wound healing process following tendon rupture or tear can be broadly classed into four phases, summarised in Table 3.

Table 3: Description of phases in wound-healing process [71]

Phase	Event Description
Haemostasis	Immediately following trauma, vasoconstriction occurs and blood flow to the area of injury is reduced to minimise loss; thrombocyte plug forms to block leak and coagulation cascade is initiated. This occurs in the first 0-12 hours following injury.
Inflammation	Neutrophils and monocytes migrate to the site of injury and assist in cleaning up debris and dead tissue at the site of injury; cytokines and complement proteins are released which trigger an inflammatory reaction, characterised by redness, heat, swelling, and increased blood flow to site of injury. This process is most prominent in the first week following injury, but inflammation can persist in patients with chronic tendon injuries [70].
Proliferation	Angiogenesis and granulation tissue formation occurs in this phase. Macrophages and fibroblasts modulate this phase and provide damaged tissue with structural integrity and a template which guides the remodelling phase. This predominantly occurs in the first 2 weeks following injury.
Remodelling	Granulation tissue is replaced by collagen and elastin fibres to form scar tissue; remodelling is modulated by macrophages, endothelial cells, fibroblasts, and tenocytes. While this process is initiated 1-2 weeks following injury, remodelling can continue in the order of months or years

	and result in chronic scarring [17]. A significant amount of tensile strength can be restored, but the consensus among most researchers is that repaired tissue does not recover its full pre-injury mechanical integrity. This phase is still very poorly understood and is the area of focus for many benchtop tendon research groups.

As described in Table 3, tendon remodelling involves a combination of intrinsic factors, such as matrix structure and composition, and extrinsic factors, such as vascular supply, inflammation, and mechanical stimulation [17, 72]. Research surrounding the structural changes in healing tendon tissue draws numerous parallels to the structural changes occurring in newly developing tendon. In the remodelling process, tenocytes synthesise ECM tendon components (e.g. collagen, GAG proteins, and elastin), with the reorganisation of these components being modulated by growth factors, matrix enzymes, and tenocytes [73]. As described by Dean et al., growth factors such as Vascular Endothelial Growth Factor (VEGF) and TGFβ are upregulated in chronic tendon disease [74]. Interestingly, these growth factors are also shown to be upregulated in foetal tendon [17, 75, 76], thereby supporting the parallel pathways between tendon healing and new tissue formation. TGFβ's role is described as helping to recruit and sustain tendon progenitor cells, while VEFG serves to differentiate vascular and avascular zones within developing and healing tendon [75].

As discussed in Section 2.1, animal and human studies have established that mechanical stimulation plays a vital role in tendon healing [77]. These changes are controlled through cellular mechanotransduction pathways, including stretch activated ion channels, cytoskeletal structure alteration, focal adhesion-mediated signalling, uptake of soluble factors, and stimuli on the primary cilia of the cells [17]. Controlled movement of the injured tendon enhances its tensile strength and ensures a return to physiologic tissue proliferation and cellular metabolism [78]. Furthermore, mechanical stimulation of fibroblasts helps increase ECM production and improve the alignment of collagen in damaged tissue [79].

In the remodelling phase, sequential changes in the mechanical properties of tendon tissue over the course of numerous months have been observed in animals. In a study examining rabbit Achilles tendon over a

12-week period, injured tissue with only one fifth the tensile strength and elastic modulus of healthy tendon was able to recover 60 % of its uninjured tensile strength and 80 % of its elastic modulus after 12 weeks of repair [80]. These findings were consistent with macroscopic and histologic changes noted, including a return to healthy tendon diameter at 12 weeks post-injury and increasing parallel alignment of collagen fibres [80]. Other animal models for tendon repair, such as equine, ovine, and rat, have similarly demonstrated that tendon remodelling and strengthening continues months to years following injury [81-83]. These findings of continuous remodelling have also been seen in human tissue, where chronic tendon injury specimens were found to share greater histologic similarity with intact tendon than acute injury specimens when comparing cellularity, alignment, and immune cell presence [84].

2.2.4 Rotator Cuff Disease Management

Drug-based treatment, physical rehabilitation, and surgery are currently used for managing tendon injuries. While each of these methods are adopted in clinical practice, limitations to each approach are documented in academic literature.

Medical Treatment

Opinions are divided regarding medical management of rotator cuff injury and there is currently inadequate high-quality evidence surrounding a definitive drug-based treatment plan for rotator cuff injury [85]. Current drug treatments include non-steroidal anti-inflammatory drugs (NSAIDs), cyclooxygenase (COX-2) inhibitors, and corticosteroid injections. A systemic review of oral NSAID use for rotator cuff tendinopathy found that while these medications can provide short term pain relief to patients with rotator cuff disease, there is no evidence of long term benefit or functional improvement related to these medications [86]. Commonly offered by rehabilitation physicians and sports physicians as a treatment option for rotator cuff tendinopathy, corticosteroid injections have similarly been found to only offer short-term pain relief [87, 88].

Glucocorticoids, local anaesthetic (often lidocaine), hyaluronic acid, and Platelet-Rich Plasma (PRP) are injectable therapies which are currently used in clinic for treating rotator cuff pathology. Dry needling, a frequent comparator to these injectable compounds, does have support in literature for the acute management of rotator cuff tears [89]. The use of PRP remains contentious in patients, with some studies suggesting that "PRP injection is safe and useful for rotator cuff disease," [89], while several Level I randomised control trials have shown that PRP "did not improve clinical outcomes" [90] and that "PRP injection was found to be no more effective […] than placebo in patients with chronic rotator cuff tendinopathy" [91]. Meta-analysis of clinical PRP use suggests marginal clinical difference in favour of injection [92]. Local anaesthetic and hyaluronic acid were similarly found to provide no clinically relevant difference in treatment to placebo alternatives [93, 94]. These contradictory findings are challenging for clinicians to navigate, which in turn leads to inconsistent practices when providing patients with localised injections.

The role of biologics, genetic material, and stem cell products as therapeutic agents is currently being explored. In animal models, 5-fluorouracil, a biologic currently used in cancer treatment, was shown to reduce undesirable adhesions during the tendon repair process in chicken tendons [95]. Gene therapies such as Platelet Derived Growth Factor (PDGFβ) have also been tested in animal models and have shown to increase angiogenesis and collagen deposition in damaged ligament tissue [96]. While these treatments show promise, safety and ethical concerns have limited their ability to enter the marketplace.

Given current literature surrounding oral treatment, injections and emerging technology, there are limited evidence-based medical treatments for rotator cuff disease that offer long-term benefit to patients.

Physiotherapy

The evidence supporting physical therapy for tendon disease is more favourable. It is almost always included in the treatment plan and has been shown in literature to reduce pain and increase long term functional improvement following tendon injury [97-99]. A key mechanism underlying musculoskeletal physiotherapy is controlled provision of multiaxial loading to injured tissues to stimulate healthy tissue

development [78]. A four-phase therapy rehabilitation programme, consistent with the phases of wound healing discussed in Section 2.2.4, is standard practice among musculoskeletal physiotherapists [100-103].

The first phase of rehabilitation is a 1-4 week period focussed on reducing inflammation, pain management, and optimising tendon healing by providing mechanical cues to guide tenocyte alignment. The first phase of rehabilitation is also focussed on avoiding undesirable complications, such as the formation of adhesions and stiffness, if surgical intervention was required [101]. The important established relationship between tendon integrity and mechanical stimulation provides a case for starting physical therapy as early as possible. Early rehabilitation must also be counterbalanced by increasing risk of tissue failure, however, especially following surgical repair of rotator cuff tears. Given surgical repair rates of failure are between 20-90 % [7-10], with many of these re-tears occurring within the first 6 months post-operatively, it is essential that the healing tissue be protected from excessive loading.

Phase II therapy takes place 4 weeks following the first phase of rehabilitation and is characterised by the transition from passive ROM to assisted active range of motion exercises (AAROM), with the goal of transitioning to independent active range of motion [100]. During this phase, inflammatory and proliferative phases of wound healing will largely be complete and remodelling of the tissue continues. The strength of repair has been described in literature as being around 20-30 % of normal strength at 4-6 weeks post-operatively [100]. Thigpen et al.'s targeted 4 key exercises for Phase II rehabilitation are: external rotation (infraspinatus and teres minor), internal rotation (subscapularis), row (posterior deltoid and periscapular muscles), and forward reaching tasks (anterior deltoid and supraspinatus) [100].

Increased tendon-bone fibre connections will have formed at 8-12 weeks following injury and animal studies suggest that tendon integrity is at 30-50 % of its pre-injury strength [100, 104]. The transition from restoring adequate range of motion to rotator cuff strengthening is the main objective of phase III rehabilitation. These exercises will include isolated strengthening of the rotator cuff muscles, isometric

exercises, and use of elastic bands. This phase of rehabilitation may last anywhere from 8-20 weeks, depending on the initial degree of injury and whether surgical intervention was required [99, 101, 102].

At 12-20 weeks following cuff repair, phase IV strengthening begins. Criteria for beginning this phase include good tolerance of basic strength training from phase III, a lack of stiffness, and no pain when completing activities of daily living. Goals of this phase include return to sport for athletes, maximum tensile stress isometric exercises, and resistance training with weights [99, 100, 102]. Strengthening of surrounding muscle groups, including the trapezius, scapular stabilising muscles, and deltoid ensures stability of the glenohumeral joint. Using the four phases of rehabilitation described above, a sample exercise routine has been provided in Table 4.

Table 4: Exercise programme based on recent guidelines for shoulder rehabilitation [99-102, 105]

Phase	Exercises Recommended
Phase I – Protective Motion with Physical Therapist guidance (0-4 weeks post-operative)	-PROM abduction -PROM forward elevation -PROM external and internal rotation <30º -Supported pendulum exercise -Scapular retraction/depression
Phase II – Transition to Active Range of Motion with Guidance (4-8 weeks post-operative)	-Forward elevation in therapy pool to 120º -Slow, controlled abduction in scapular plane (maximal speed of 30º/second) -"Salute exercise" -Reaching tasks -Side lying external rotation (no weight) -Alternating external-internal rotation -Cross arm stretch
Phase III – Basic Strength Training (8-20 weeks post-operative)	-Internal and external rotation with small free weights -Triceps Extensions -Forward flexion with resistance band -Rolling ball on wall -Upright wall slide -Light-weight scapular rows
Phase IV – Advanced Strength Training (12+ weeks post-operative)	-Push-ups -Forward flexion to 90º with free weight -Internal and external rotation with free weights to 45º -"Bear Hug" exercise -Proprioceptive neuromuscular facilitation with resistance band (diagonal pattern across body)

Although the phases of rehabilitation have been generally well established in literature, there is still uncertainty as to the optimal frequency of rehabilitation for patients. In the randomised control trials examined, exercise programme frequency ranged from 3 sessions per week, to 3-4 sessions daily, depending on the exercise type and the phase of rehabilitation [99, 106-108]. Furthermore, physical therapy is often not sufficient for large tears and surgical reattachment of the damaged tendon is required.

Surgical Management

Surgical rotator cuff tendon repair can be considered when a patient cannot be treated using rehabilitation and medical therapy alone. Current operative procedures available for rotator cuff repair include open surgery, arthroscopic procedures, or mini-open arthroscopically assisted surgery, whereby the torn rotator cuff tendon is reattached to the insertion site on the humerus. While arthroscopic surgery has gained popularity due to ease of operation and perceived lower risk of surgical complication, current evidence from clinical trial data suggests that there is no difference in clinical effectiveness or cost-effectiveness between open and arthroscopic repair of torn rotator cuffs [109].

There is growing evidence that surgical outcomes following rotator cuff repair remain poor. Literature examining post-operative results has shown that patients who have a rotator cuff repair will experience rates of failure upwards of 40 %, depending on the degree of the initial supraspinatus tendon tear [7-10]. Reasons for post-operative failure include poor tissue healing, donor site morbidity, and mechanical failure of the suture. While pain relief has been noted following surgery, post-operative functional outcomes are estimated to be poor in up to 35 % of patients following surgery [102, 110]. With the increasing prevalence of tendon injury due to an aging population and poor treatment outcomes, there is a growing need for knowledge from other disciplines, such as tissue engineering and regenerative medicine, to inform and advance therapy for tendon injuries.

2.3 Tendon Tissue Engineering

Given that tissue engineering is a broad topic, this section is limited in scope to focus on mechanical stimulation and future strategies to improve the physiologic relevance of loading programmes.

2.3.1 Overview of Tendon Tissue Engineering

Tissue engineering involves the complex interplay of gas exchange, nutrient and waste transfer through the system, temperature and pH control, and maintenance of a sterile environment. Unlike conventional methods of tissue culture, *in vitro* tendon tissue engineering additionally involves provision of mechanical cues to the culture. Figure 8 describes key components for successful tendon tissue engineering.

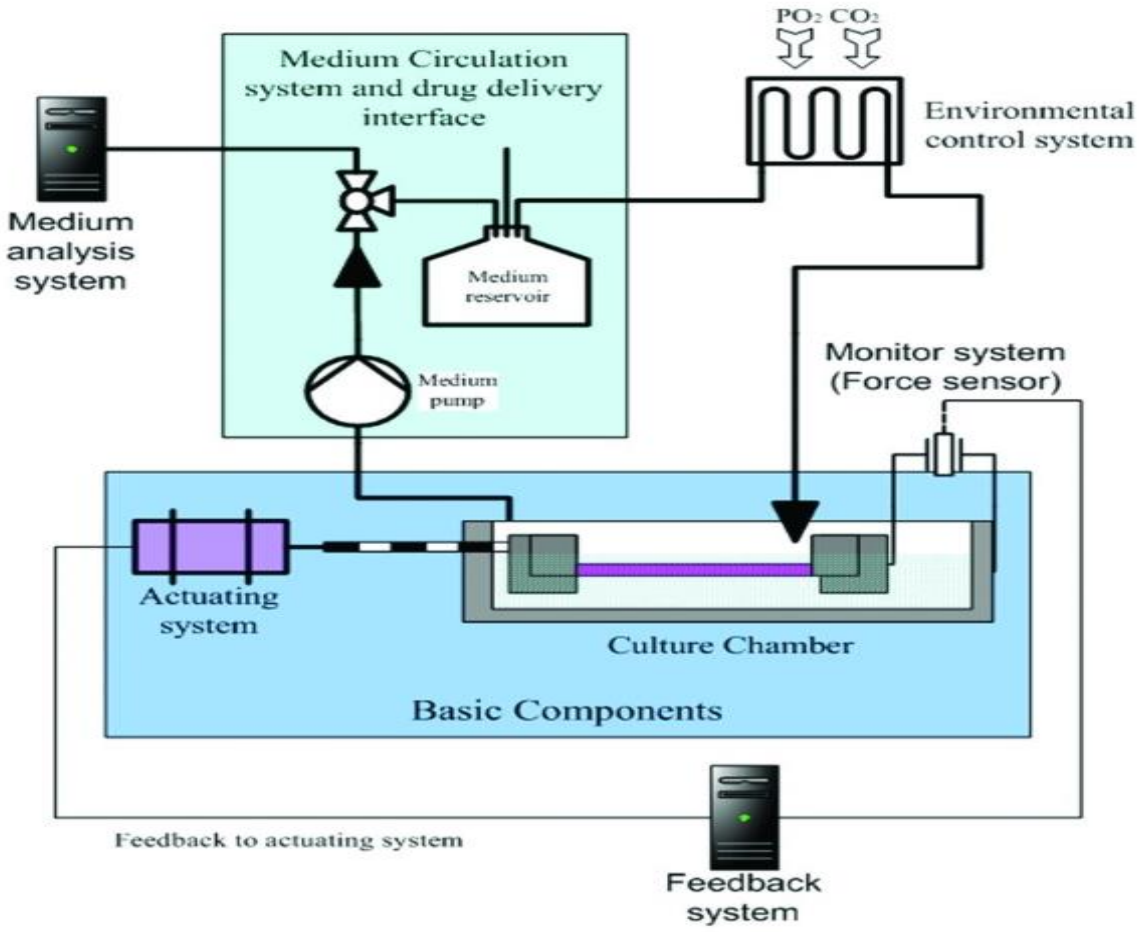


Figure 8: Generalised schema illustrating components commonly included in current tendon tissue engineering systems (reproduced from Wang et al.) [12].

As shown through *in vitro* studies investigating tendon healing and mechanobiology, tendon tissue requires mechanical stimulation to grow and develop properly. It is therefore important to provide tendon tissue constructs with the right amount of tensile stress and appropriate mechanical cues; insufficient stimulation has been shown to lead to catabolic gene expression and eventual loss of structural integrity [16, 29], while excess loading of tendon tissue leads to inflammation, degradative enzyme production, undesirable fibroblast differentiation and programmed cellular death [51]. *In vivo* imaging studies have estimate that peak tendon deformation for physiologic motion ranges from 3-15 % depending on tendon location and individual anatomy [22, 27], while tendon tissue engineering studies prior to 2014 suggest that 2-10 % strain applied cyclically at a frequency in the range of 0.1-2 Hz results in optimal engineered constructs [12].

To explore recent advances in tendon tissue engineering, a list of studies in the PubMed database related to tendon tissue engineering from January 2014 to December 2019 was compiled. Earlier studies were excluded from this compilation as they have already been summarised in previous review articles [12, 111-114]. Search terms for these articles included “tendon tissue engineering”, “tendon mechanobiology”, or “tendon bioreactor”. A total of 1435 articles were initially found matching these search terms. From this initial group, 43 articles were shortlisted. Articles that did not involve tissue culture or mechanical stimulation were removed, thus limiting this compilation to the 22 studies provided in Table 5.

Table 5: Recent tendon tissue engineering experiments involving provision of mechanical stimuli

Publication	Loading Direction and Type	Loading Frequency and Duration	Loading Quantity Provided to Constructs	Strain Measured	Strain Distribution	Cell Source and Scaffold Material (scaffold dimensions)
Sawadkar et al., 2019 [115]	Uniaxial tensile	Dynamic trial: 15 minute cyclic loading followed by 15 minutes unloading, repeated over 24 h period; Static Trial: constant loading in static conditions over 24 h period	0-3700 μN (dynamic) 3250 μN (static)	0-10% (dynamic) 10% (static)	Modelled as uniform	Rabbit tibial tendon fibroblasts seeded to collagen lattice derived from rat tail (75 × 25 × 15 mm)
Sensini et al., 2019 [116]	Uniaxial tensile	Cyclic loading applied twice over a 7 day culture at 1 Hz	Not available	5%	Modelled as uniform	Human foreskin fibroblasts seeded to electrospun polylactic acid (PLLA)/collagen (cross-section: 1.46 ± 0.08 mm; length: 89.4 ± 2.1 mm)
Hsiao et al., 2019 [117]	Uniaxial tensile	Cyclic loading applied over an 8 h period at 0.5 Hz	Not available	4 or 8 %	Modelled as non-uniform using finite element analysis (FEA)	Rat patella tenocytes, cultured in wells on a tensile plate (no scaffold)
Morita et al., 2019 [118]	Uniaxial tensile	Cyclic loading applied over a 2 day period at 1 Hz	Not available	2-8 %	Modelled as non-uniform using digital image correlation (DIC)	Human bone marrow mesenchymal stem cells (hBMSCs) seeded to glass membrane
Nakanishi et al., 2019 [119]	Uniaxial tensile	Static loading over 4 and 8 week period	Not available	Not available	Modelled as uniform	Human dermal fibroblasts (HDF) seeded into 3-D printed Dulbecco's modified Eagle medium (DMEM) spheroids (diameter 500 μm–600 μm)
Talò et al., 2019 [120]	Uniaxial tensile	Cycle of 15-30-60 min loading alternated by 15-30-60-min rest 2 times/day over 7 day culture at 0.33 Hz	4-25 N	1-7 %	Modelled as uniform	Rabbit BMSCs seeded to decellularised equine tendon tissue (43 x 5 x 3 mm)
Rinoldi et al., 2019 [121]	Uniaxial tensile	Static loading applied over 7 day culture period	Not available	15 %	Modelled as uniform	hBMSCs seeded to a wet spun gelatine methacryloyl alginate hydrogel
Raveling et al. [122]	Uniaxial tensile	Cyclic loading over 3 day period at 0.05 Hz	0-190 kN/m^2	0-10 %	Modelled as uniform	Mouse MSC cells seeded to type I collagen sponges (length: 12mm, width: 4mm)
Mubyana et al. [123]	Uniaxial tensile	Cyclic loading over 7 day culture at 0.1 Hz	0-100 kN/m^2	0-0.70 %	Modelled as uniform	HDF seeded in agarose growth channels
Raimondi et al., 2018 [124]	Uniaxial tensile	Cyclic and static loading applied over 7-14 day culture period at 0.5-2 Hz	1.5-4.5 N	3-10 %	Modelled as uniform	Porcine Achilles tenocytes, seeded to type I equine collagen sponge scaffold (40 × 5 × 5 mm)

Engebretson et al., 2018 [125]	Uniaxial tensile	Cyclic loading applied 0.5-2 h/day for culture of up to 7 days at 0.01-0.03 Hz	Not available	2 %	Modelled as uniform	Rat BMSCs seeded to decellularised human umbilical vein (diameter: 6.75 mm length: 6.5 cm)
Testa et al., 2017 [126]	Uniaxial tensile	Cyclic loading applied over 1 h/day over 15 day culture period at 0.5 Hz	Not available	10 %	Modelled as uniform	Mouse fibroblast cells seeded to Polyethylene glycol-Fibrinogen hydrogel (10 × 3.3 × 1.5 mm)
Wu et al., 2017 [127]	Uniaxial tensile	Cyclic loading applied for 2h/day over 12 day culture period at 0.5 Hz	Not available	4 %	Modelled as uniform	Human adipose MSCs seeded to electrospun polycaprolactone (PCL) scaffold (thickness: 180 µm)
Grier et al., 2017 [128]	Uniaxial tensile	Cyclic loading for 10 min every 6 h over 6 day culture period at 1 Hz	Not available	10 %	Modelled as uniform	Human MSCs seeded to collagen-GAG scaffold (6 x 6 x 15 mm)
Adekanmbi et al., 2017 [129]	Uniaxial tensile	Dynamic trial: tissue loaded for 1 h/day over 5-day culture period, at 1 Hz, 20 Hz Static trial: tissue loaded for 1 hr/day over 5-day culture period	-0.04-0.12 N	No	Not Applicable (Stain not reported)	Rat tail tendon fascicles
Joo Kim et al., 2016 [130]	Uniaxial tensile	Cyclic loading for 1 hr at 0.5 Hz	Not available	2-4 %	Modelled as non-uniform using digital image correlation (DIC)	Rat tail tenocytes seeded onto moulded polydimethylsiloxane scaffold (26 x 19 x 1 mm)
Cook et al., 2016 [131]	Uniaxial tensile	Cyclic loading for 1 h/day over 5-day period at 0.5 Hz	0-5 mN	1-9 %	Non-uniform strain characterization using fluorescent DIC	Human adipose derived stromal cells seeded to fibrin scaffold
Burk et al., 2016 [132]	Uniaxial tensile	Cycle of 15-30-60 min loading alternated by 15-30-60-min rest at 1 Hz	Not available	2 %	Modelled as uniform	Subcutaneous equine adipose tissue seeded to decellularised equine tendon scaffold (10 x 1 x 2 mm)
Nam et al., 2015 [133]	Uniaxial tensile	Cyclic loading for 6-72 h period at 0.5-1 Hz	Not available	4-12 %	Modelled as uniform	HMSCs seeded to silicon chambers
Youngstrom et al., 2015 [134]	Uniaxial tensile	Cyclic loading for 0.5-1 h/day over 8 days at 0.33 Hz	Not available	0-5 %	Modelled as uniform	Equine MSCs seeded to decellularised equine tendon scaffolds (10 x 45 x 0.4 mm)
Qin et al., 2015 [135]	Uniaxial tensile	Cyclic loading at 20 min/hr over a 12 h for up to 7 days of culture at 0.2 Hz	Not available	3 %	Modelled as uniform	Canine MSCs seeded to decellularised canine tendon (length: 40 mm; width: 300 µm)
Huisman et al., 2014 [136]	Biaxial Tensile	Cyclic loading for up to 1000 cycles at 0.1 Hz	Not available	10 %	Modelled as non-uniform using finite element analysis (FEA)	Human hamstring cells suspended in DMEM and tested in type I collagen-coated bioreactor wells

2.3.2 Effect of Scaffold and Cell Type on Mechanical Environment

As described in existing literature, ideal cells in tendon tissue engineering will satisfy the following criteria: their ability to differentiate into *in situ* cells, the ability to deposit extracellular matrix with properties similar to that of native tissue, their ability to successfully proliferate within the engineered construct, their availability for research purposes, and no ethical or legal concerns associated with their use [137]. The broad categories of cells currently being used include stem cells, tenocytes, and dermal fibroblasts [138]. While the native tenocytes and *in situ* fibroblasts – used in seven of the studies listed in Table 5 – represent the most clinically relevant cell source for tendon engineering, obtaining these cells can be challenging in practice. Tendon cell extraction poses a significant risk of donor morbidity and extracting a satisfactory quantity of tendon cells is challenging given their low cell number in native tissue [138]. With these practical limitations, other cell types are also currently being used for tendon tissue engineering.

Non-tendon stem cells, including embryonic stem cells (ESCs), bone marrow mesenchymal stem cells (BMSCs), and adipose derived mesenchymal stem cells (ASCs) have been used in twelve of the studies listed in Table 5. Advantages of these cell types include their potential to differentiate and high proliferative capacity. Limitations for translational applicability in the use of BMSCs and ASCs include the risk of ectopic bone formation within the constructs and senescence with increased cell passaging. Pluripotent ESCs are appealing due to their proliferative ability but have limited availability due to strict policy and ethical concerns surrounding their use. Dermal fibroblasts, used in three of the twenty-two studies listed in Table 5, are collagen producing cells with similar morphology to tenocytes that readily proliferate. These cells can be readily sourced via skin punch biopsy and have low risk of donor site morbidity [137]. Disadvantages of this cell type include the risk of fibrotic scar formation and suppression of tendon-like healing in absence of tenocyte biomarkers [12, 137]. Overall, dermal fibroblasts and non-tendon stem cells are generally easier to obtain and proliferate than tendon cells but may not be as suitable

for producing ECM with mechanically similar properties to that of native tendon. This trade-off is important to consider and account for when selecting a cell line for tendon tissue engineering.

The scaffold used for the tissue construct is also important to consider. Previously, tendon tissue engineering consisted of two-dimensional (2D) constructs, whereby cells were cultured in petri dishes. While this method permits effective cell proliferation and easier control of nutrient and gas exchange, 2D models for tendon tissue lack physiologic relevance as they do not have similar dimensions or architecture to native tissue. A physiologically relevant microenvironment should assist in providing cues that influence the alignment, migration, loading and gene expression of tendon cells [30].

Over the past five years, an encouraging trend in tendon tissue engineering has been the transition towards using biocompatible three-dimensional (3D) polymers and decellularised tendon tissue as scaffolds, as seen in most of the studies listed in Table 5. Furthermore, increased sophistication in manufacturing techniques for synthetic materials, such as electrospinning, has allowed synthetic constructs to replicate the microstructure of native tissue more closely, providing cues for cellular alignment and load transmission more like that of biological tissues. As tendon tissue engineering continues to evolve, it will be important for scaffolds to have similar dimensions and biomechanical properties to native tissue.

2.3.3 Provision of Loading by Bioreactors

Recognising the importance of maintaining a tightly regulated range of values for strain in tendon tissue engineering, studies from the past six years have increasingly focussed on quantifying the deformation of their constructs in real-time. Twenty of the twenty-two studies examined in this paper provided strain measurements in their construct, in contrast to less than half of the studies quantifying strain in earlier literature [12]. Common methods of approximating strain in the samples which have been used in recent literature include use of strain gauges, extensometers, and manually setting the displacement of the bioreactor by measuring the sample. This increased emphasis on quantitatively monitoring strain

demonstrates significant progress in tendon engineering, building upon previous results from literature suggesting that 2-10% strain at a frequency of 0.1-2 Hz over multiple days of culture will result in more optimal engineered constructs.

The force or stress applied to constructs is less consistently reported in current literature. While strain has been identified as the primary metric for assessing health of a tissue construct, force or stress values would be valuable as the amount of loading required for strain within an optimal range is highly dependent on the individual tendon tissue samples [14, 16, 19, 20, 22, 23]. Furthermore, recording and reporting the real time force values would allow for validation of the results through comparison of stress-strain data provided in studies examining the mechanical properties of tendon tissue *ex vivo*.

In addition to providing the appropriate quantity of mechanical stimulation, the direction and types of mechanical stimulation provided to tissue constructs should mirror the deformation this tissue experiences during physiologic loading. While *ex vivo* and *in vivo* studies have consistently demonstrated that tendon tissue deforms non-uniformly and experiences multiaxial stress during physiologic loading, there is negligible peer-reviewed work examining the effect of different strain modules and multiaxial strain on the development of tendon tissue constructs. Some researchers have suggested that uniaxial tensile strain is the only required loading programme for optimal engineered tendon growth [111, 112], but since the effects of different types and directions of strain on tendon tissue engineering cultures have been minimally explored in literature, this suggestion has not been validated. Furthermore, it has been shown that the connective tissue in many human joints experiences multi-axial strain *in vivo*, even in hinge joints that primarily move in one axis, such as the knee [139]. The current lack of bioreactor systems that can provide multiple forms of stress and multiaxial strain to constructs could be a major barrier to developing physiologically relevant tissue engineering systems.

Although tendon tissue engineering has moved towards real-time strain measurement, most current studies do not adequately account for non-uniform deformation in their systems; only five of the studies

in Table 5 discussed non-uniform strain to their construct and four of these studies modelled the non-uniform deformation pattern [117, 118, 130, 131]. Non-uniform deformation needs to be more consistently examined and accounted for in future tendon engineering studies and should ideally be examined using tools like quantitative ultrasound, which can provide estimates of deformation across the thickness of the tissue construct [140].

2.3.4 Summary of Current Methods in Tendon Tissue Engineering

The increasing number of tendon engineering studies corresponds to the growing interest in tissue mechanobiology. Encouraging trends in recent literature include better understanding of the advantages and limitations of the various cell types available for tissue culture, improved physiologic relevance in scaffold design, and more attention to providing appropriate quantities of mechanical stimulation for tissue constructs. There are significant barriers that need to be addressed before tissue engineering can be translated to clinical practice, however. To produce more physiologically relevant engineered tissue, next steps include development of bioreactor systems that are capable of: i) providing multiaxial loading. ii) adapting the loading regime for individual tissues in consideration of anatomic location, and iii) providing loading which results in the non-uniform strain profiles observed *in vivo* [13]. A summary comparing native and engineered tendons since 2014 is provided in Table 6.

Table 6: Comparison between native tendon tissue and engineered tendons from studies conducted between 2014-2020

	Native Tendon Tissue	**Engineered Tendon**
Direction and Type of Loading	Multiaxial compressive, torsional, tensile, and shear loading	Uniaxial tensile loading
Magnitude of Strain Under Loading	3 – upwards of 15 % (depends on location of tissue and individual)	2-10 %
Strain Distribution	Non-uniform, with variation in strain along the length and thickness of the tissue	Generally assumed to be uniform throughout construct

2.3.5 Musculoskeletal Robots for Tendon Tissue Engineering

Robotic technology is being used clinically for a variety of applications, including orthopaedic surgery, advanced prostheses, and powered exoskeletons for rehabilitation following neurological injury [141]. There is also growing interest in using advanced robotic systems in musculoskeletal tissue engineering. To address the lack of current bioreactor systems which can provide physiologically relevant mechanical stimuli, our research group has proposed using musculoskeletal humanoid robots to assist in growing tissue grafts for clinical application, with a specific focus on the rotator cuff tendons [13].

Initially designed for applications such as crash test dummies, prosthesis, and athlete enhancement, there are four characteristics of human musculoskeletal anatomy and functionality that humanoid musculoskeletal robots imitate to be suitable for these applications: "i) body proportion, ii) skeletal structure, iii) muscle arrangement, and iv) joint performance[†]" [142, 143]. Humanoid robots currently in use include "Eccerobot", developed by a cross-European partnership, "Kenshiro", developed by the Asano group in Japan, and "Roboy", developed at the Technical University of Munich [142-145]. Prototypes of these systems are shown in Figure 9.

Robotic limbs have conventionally been articulated by rigid joints that restrict movement, have limited energy storing capacity, and provide kinematically constrained motion [146]. In contrast, musculoskeletal robots, such as "Roboy", rely on tendon-driven systems, whereby tension applied via a string cord causes the actuation system to compress an energy-storing spring and respond to the tensile stress correspondingly [147, 148]. By having similar dimensions and weights to human limbs, humanoid robots can also imitate the range of forces observed *in vivo* while actuating these structures. Furthermore, since the number of degrees of freedom and arrangement of actuators is designed according to the anatomic position of analogous muscles, the direction and types of loading experienced by musculoskeletal robot joints might be physiologically relevant [13, 145].

[†] To imitate joint performance, range of motion, rigidity, and number of degrees of freedom are considered.

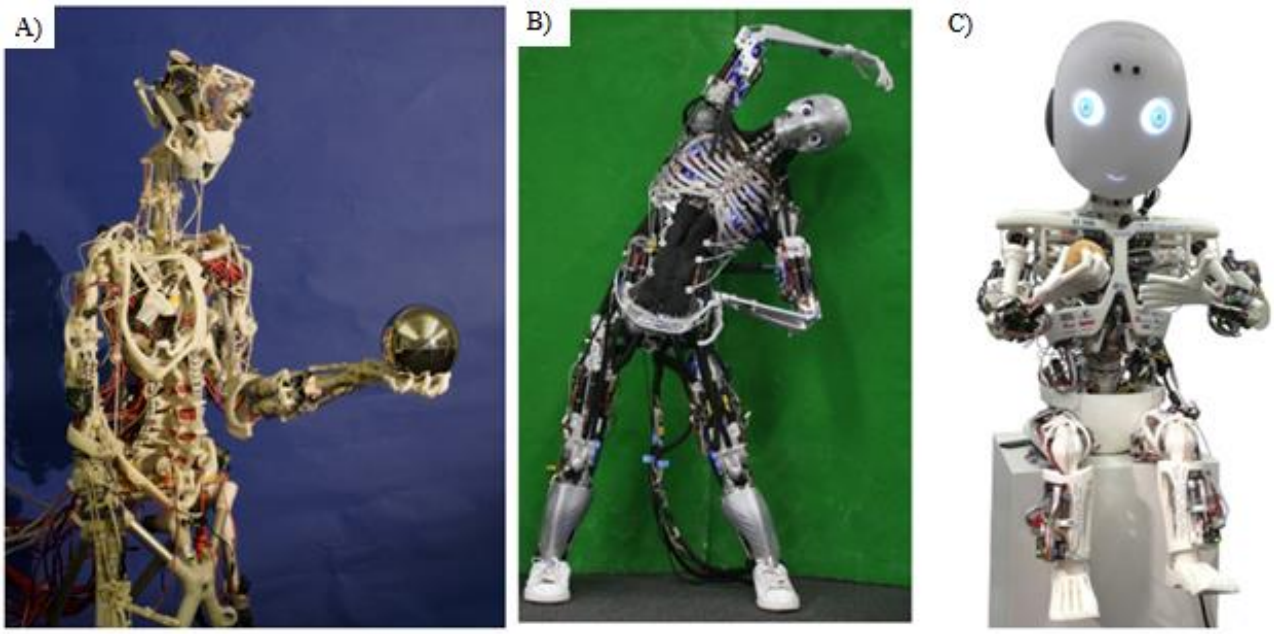


Figure 9: Humanoid musculoskeletal robots currently in use: A). Eccerobot, B). Kenshiro, and C). Roboy (images obtained from Diamond et al., Asano et. al., and Devanthro GmbH) [142-145].

While the intersection of musculoskeletal robotics and tendon tissue engineering is largely unexplored, the opportunity to provide multidirectional stresses and to develop loading programmes that consider the anatomic location of tendon tissue being incubated [13] makes application of humanoid robots a promising strategy within tissue engineering.

2.4 Technical Background

This section of the thesis is intended to provide context to the theory and current research surrounding technology used in this thesis, including upper limb motion analysis, musculoskeletal modelling, and digital image correlation (DIC).

2.4.1 Upper Extremity Motion Analysis

Non-invasive motion analysis (MA) is a powerful tool through which consecutive images from a sequence captured by video can be interpreted to yield valuable kinematic information. MA is used clinically to diagnose pathology, inform treatment of musculoskeletal conditions, and inform the development assistive technology, such as protheses or musculoskeletal humanoid robots [149, 150].

Despite a growing clinical interest, upper limb MA remains a challenging task. MA is often described as a well-established and objective "gold standard for evaluating lower limb function during gait" for a variety of conditions, such as cerebral palsy (CP) [151-153]. Gait can be objectively assessed and quantified through MA because it consists of one standard movement that repeats cyclically across a limited range of motion. Furthermore, complementary equipment, such as force and pressure plates, allow for reasonable lower limb kinetic parameter estimates, such as joint moment [154]. In contrast, upper extremity (UE) MA is widely considered to be more technically challenging [155, 156]. Unlike gait, no single task represents functional UE use. UE modelling is further complicated by the large ranges of motion, increased variability in physiologic movement paths during task completion, and complexity of UE joints such as the shoulder [156].

There is a significant body of literature proposing tasks which accurately represent functional UE use. Examples of tasks proposed in UE MA can be categorised into four groups:

i) Basic ROM Tasks (e.g. for the shoulder- abduction, adduction, flexion, extension, internal rotation, and external rotation) [157-159]

ii) Reaching Tasks (e.g. reach to opposite axilla, sideways reach, upwards reach, forward reach to grab object) [151, 160-162]

iii) Activities of Daily Living (ADLs) (e.g. brush opposite side of head, lift block from shoulder level, hand to mouth for eating/drinking, hand to back pocket, throwing to a target) [160, 161, 163]

iv) Tasks which evaluate hand and finger function using fine motor tasks [164]

In clinical practice, there are several validated tests for limited patient populations, such as the Shriners Hospital for Children Upper Extremity Evaluation (SHUEE) for children aged 3-18 years with CP [164]. The SHUEE consists of 16 tasks and is evaluated by a single clinician. Despite being widely used in clinical practice, tests such as the SHUEE are lengthy, limited in scope, and require subjective expert

analysis to score [151]. Furthermore, many of these tasks rely on 2D video data, therefore being prone to out of plane errors during interpretation. Researchers have consistently identified the lack of standardisation in task protocol as a major bottleneck in UE MA [155, 165, 166]. With the plethora of tasks available to quantify UE function and lack of standardisation in protocol, individuals conducting UE MA should have a clear idea about which aspects of functionality they want to explore. This will guide the development of task protocol for their study if no clinical test exists for the intended application.

The challenge of finding a suitable method for modelling the UE must be addressed once a task protocol has been established for the motion study. The human body is an "extremely complex, highly articulated, self-occluding, and only partially rigid entity" [167]. MA software therefore employs simplifying assumptions to facilitate human body analysis. One notable simplification commonly made is that the human body gets divided into segments represented by rigid bodies (i.e. no segment deformation under external loading) which are connected by ideal, frictionless rotational joints with up to 3 DoF, depending on joint type. This simplification is reasonable as it is difficult to accurately describe geometric translations within joints using non-invasive MA [168].

Cutti and Kontaxis have described segments of interest for UE modelling as being the thorax, clavicle, scapula, humerus, forearm, and carpus of the hand to provide an anatomically representative model [155, 168]. Correspondingly, joints of interest for these segments would comprise the GH (3 DoF), SC (2 DoF), AC (3 DoF), elbow (2 DoF), and wrist (2 DoF) – with 12 DoF in total [168]. These segment and joint definitions are consistent with those put forth by the International Society of Biomechanics (ISB) Standardization and Terminology Committee, whose goal is to standardise modelling in MA studies [169]. Despite the physiologic relevance of this recommendation, development of a practical model comprising all these segments is challenging in practice; reliably capturing the behaviour of the clavicle and scapula has been described as "almost impossible to track noninvasively" [168] and "difficult to track with external markers due to the large amount of movement under the skin" [170].

To overcome these challenges, model simplifications include a fictitious linking of the sternum and glenohumeral head to provide a “shoulder girdle” segment and assumption of coordinated movement between the scapula and humerus during elevation (scapulohumeral rhythm) to approximate scapular position throughout a movement [168]. Other models are further simplified – because the GH joint is the primary articulating structure of the shoulder, a widely adopted assumption within UE literature is to “approximate the shoulder kinematics to the GH joint” rather than consider contributions to ROM from the other two joints (i.e. SC and AC), thereby reducing the model to 7-DoF [166]. While this approach may not be as physiologically representative as a model with scapular and clavicular segments, this simplification is popular due to ease of use and can be adopted when relative positioning of bones in the shoulder complex is not of primary importance – such as study of ADLs in healthy populations [166, 170].

Once segments and joints have been defined, a coordinate system must be chosen to represent the position of segments relative to each other and the global coordinate system (i.e. the motion laboratory). Although various forms can be used to describe 3D segment rotations, such as quaternions and rotation matrices, Euler angles are the standard convention for describing joint coordinate systems (JCS) in UE MA [169]. While this method is more intuitive for UE research, a major limitation is the risk of gimbal lock, whereby one degree of rotational freedom is lost during certain movement patterns due to two axes aligning in one plane, with resulting unstable UE motion interpretation [171]. It is therefore important to select a JCS appropriate for the functional tasks and segment definitions chosen for the model to reduce risk of gimbal lock. Although standardisation protocols have been recommended by the ISB for consistency in JCS across upper limb studies, some experts in UE MA have proposed different JCS to avoid gimbal lock [168, 169].

To obtain useful kinematic data from the motion protocol, an effective method of tracking the motion must be selected. Within UE motion capture, an ideal motion tracking system should be capable of collecting accurate kinematic information in a timely manner without encumbering participants or

influencing their natural movements [167]. In consideration of these criteria, Table 7 provides a non-exhaustive list of commonly used methods used for motion capture.

Table 7: Techniques currently available for use in human motion capture

Method	Description	Advantages	Disadvantages
Markerless Tracking [167]	There are two main tracking methods. In manual digitisation, operators sequentially track movement for a segment of interest. In automated systems, computer algorithms track movement throughout task execution.	Compact evaluation system, completely noninvasive and no influence on participant movement	Labour-intensive (manual), low precision, prone to error, not validated for biomechanics
Skin Marker [167]	Most commonly involves stereo-photogrammetric or optoelectronic systems triangulating position of retroreflective markers during movement. Markers are placed on the skin above body anatomical landmarks of interest and/or marker clusters are used to calculate functional joint centres	Relatively noninvasive and little influence on participant movement; validated for bio-mechanical applications	Subject to marker occlusion during movement; susceptible to soft-tissue artefacts
Intra-Cortical Pins [172, 173]	With local anaesthetic, pins mounted with retroreflective markers are inserted into cortical bone tissue anatomical landmarks of interest	Greater accuracy than skin-based markers for modelling movement; no soft-tissue artefacts	Painful and invasive procedure; may alter motion trajectory; requires medical expert for safe pin insertion
Inertial Systems [174]	Electromagnetic devices such as accelerometers, gyroscopes are attached to the body and measure parameters such as orientation, angular velocity, and acceleration	Affordable; very portable (i.e. possible to use for "in the field" analysis)	Devices not consistently reliable and accurate enough for clinical decision making
Wearable Technology [175, 176]	An exoskeleton or soft robotic device is attached to a participant. Potentiators or sensors detect motion as the device is actuated	Provides estimates of dynamic forces in addition to kinematics; can be relatively low cost	Constrains motion; variable accuracy; challenging to use for atypical anatomy

In consideration of all factors, skin-based marker tracking is the favoured technology for human motion capture [167]. As described in Table 7, the movement of markers attached to defined segments is tracked by optoelectrical software in this method. While there is a lack of consensus among experts on an optimal protocol for UE marker placement, multiple factors are taken into consideration when developing a marker protocol, such as risk of marker occlusion, participant comfort, and ease/accuracy of joint centre determination. For 3D-MA, each segment requires at least three non-colinear markers visible throughout

task execution to track position and orientation of the segment. Redundant markers are often placed on a segment to compensate for marker occlusion during task execution [168].

To obtain accurate results in a kinematic study, accurate estimates of joint motion must be obtained. This is typically done by placing markers on bony anatomic landmarks, from which it is possible to approximate the joint centre and principal axes of the underlying bone. Drawbacks to this method are the lack of sensitivity to normal variations in individual UE anatomy and introduction of soft tissue artefacts (STA) [156]. STA are the result of skin movement masking bony motion during task completion, thus introducing error to the model [167]. To overcome this limitation, another method of measuring joint motion involves use of a "functional model". The principle of this method is "to determine joint centres and axes in technical frames using calibration movements", whereby joint centres are estimated by optimisation following repetition of the specified calibration task [156, 177, 178]. This method is further described by Rettig et al. [156]. A marker protocol can also incorporate elements of both methods if it will improve the accuracy of the model.

2.4.2 Upper Limb Musculoskeletal Modelling

Unlike gait analysis, it is difficult to obtain reasonable estimates of external UE joint forces using force plates and MA kinematic data [177]. Furthermore, UE *in vivo* muscle and joint loading is nearly impossible to accurately measure non-invasively. Computational musculoskeletal (MSK) models are a promising tool to overcome this challenge. MSK models are broadly classified in two categories: finite element and rigid body models. While finite element model analysis offers more complexity, these models tend to be more computationally intensive and rely on a greater number of assumptions, which can therefore reduce the accuracy of the model [179]. Furthermore, fewer validated finite element models currently exist for UE analysis. For these reasons, only rigid-body musculoskeletal models were explored for this project.

Rigid body models can be driven either by forward dynamics, whereby forces are input for a body and resulting motion is predicted, or inverse dynamics, which predict muscle and joint loading from kinematic data and environmental elements as shown in Figure 10 [180]. An inverse dynamics approach is well-suited for estimating muscle and joint forces using UE MA data. Using motion data, joint moments and reaction forces are solved using laws of basic (Newtonian) mechanics. In many MSK models, muscle-tendon units are differentiated into smaller segments, given that tendon moment arm length and direction of action can vary considerably within muscle tissue [179]. Force contributions are simultaneously calculated using a load-sharing optimisation procedure which attempts to recruit muscle groups selectively to minimise an objective physiologic criterion, such as total muscle force, stress, fatigue, or energy consumption [180]. While it is hypothesised that the nervous system uses similar muscle recruitment criteria *in vivo*, electromyography (EMG) validation experiments have been unable to confirm this [181].

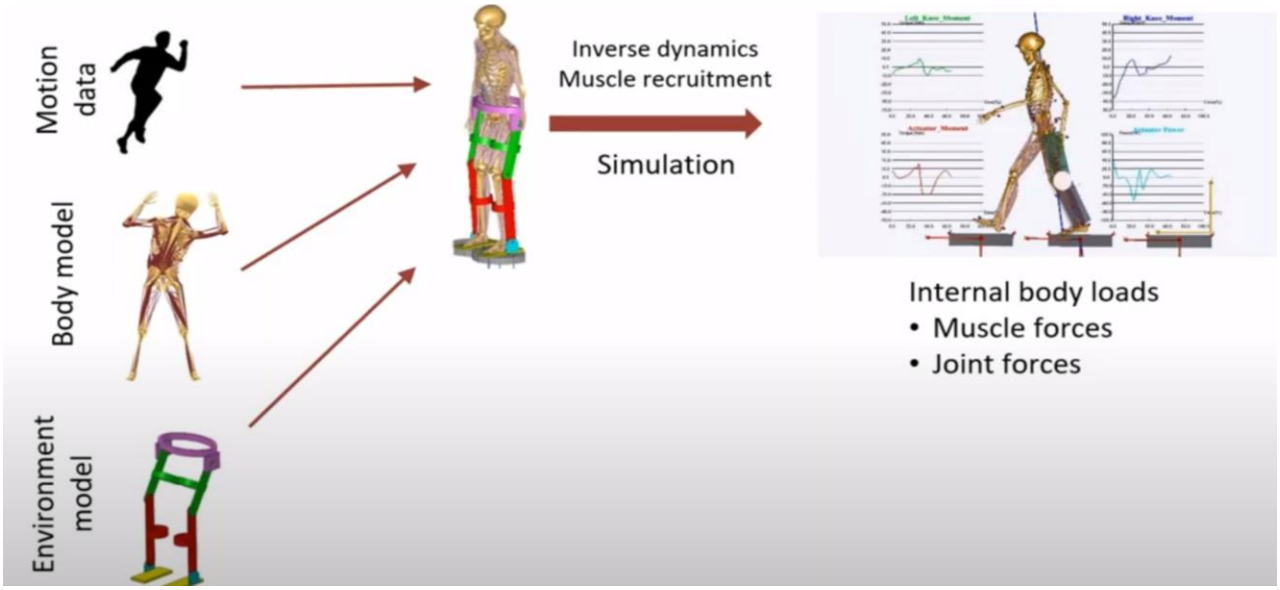


Figure 10: Inverse dynamics musculoskeletal modelling pipeline (reproduced from AnyBody™ Technology) [182].

Significant work has gone into developing appropriate models to represent human muscle behaviour. The Sliding Filament Theory, or Huxley Muscle Model, postulates that muscle proteins (actin and myosin) slide past each other, driven by adenosine triphosphate (ATP), to generate movement, [183]. This model

has been widely accepted in scientific literature as the underlying mechanism of muscle contraction. While this model directly describes the microphysical phenomena of muscle movement and force generation, the complexity and computationally demanding nature of this model has prevented it from being widely adapted in MSK modelling software. Instead, "muscles are typically modelled as Hill-type one-dimensional structures (lines) that, dependent on the complexity of the muscle model, consist of a passive (viscoelastic) and active (contractile element) part" [180]. Despite not attempting to directly replicate muscle behaviour, the Hill Muscle Model can reasonably represent many properties of human muscle, such as length, contraction velocity, fibre length, pennation angle, and tendon elasticity [184, 185]. The sacrifices in realism of the Hill Model are counterbalanced by the greater numerical efficiency of this approach for MSK modelling software.

UE inverse dynamics MSK models are available across several open-source and commercially available software platforms, including SIMM, OpenSim, and AnyBody™ Technology. Comparative studies between these platforms have shown reasonable concurrence in simulation results [186-188]. Given good consistency between platforms, selection of modelling software can be dictated by user preference. AnyBody™ Technology was the musculoskeletal model chosen for this study, because of the validated shoulder model used in the platform and the ability to interface with MA files, allowing for direct importation of kinematic data into the UE model for analysis.

The AnyBody™ Modeling System (AMS) allows users to either develop new body models or use models currently available in their library – the AnyBody Managed Model Repository (AMMR). By default, the body model available in the AMMR is based on the dimensions of a 50^{th} percentile European male (1.75m, 75kg), but the model can be scaled for individual anthropometry. To input motion and scale anthropometric data automatically, AnyBody can directly import this data from motion capture systems, such as Vicon, using .c3d files. AMS then uses this motion (and external forces if applicable) to simulate internal loads in the body and subsequently estimate force distribution among contributing muscles.

For UE modelling, the shoulder arm model provided in the AMMR is an application of the Delft Shoulder and Elbow Model (DSEM) in combination with a rigid-body lumbar spine model developed by Zee et al. [189, 190]. The DSEM has been extensively researched and improved since its introduction 25 years ago and is also implemented in other popular musculoskeletal modelling software packages, such as OpenSim [191]. Alterations to the current shoulder model in the AMMR from the original DSEM include wrapping of deltoid muscles around the GH joint to provide a more physiologically accurate actuating path and insertion [192]. The current shoulder model comprises 7 rigid body segments (thorax, scapula, humerus, clavicle, ulna, radius, and hand) with 10 DoF, actuated by over 115 muscle elements. As a rigid-body MSK modelling software, bones are represented by segments that do not undergo deformation throughout the simulation [179]. Passive elastic elements such as cartilage and ligament are neglected, which is a limitation as these elements have a key role in stabilising joints throughout movement *in vivo* [193].

As with other MSK models, the AMS has many limitations and operates using many simplifications to improve computational efficiency, which must be considered when interpreting model outputs. MSK modelling software provides estimates of muscle loading that are nearly impossible to measure experimentally; it is therefore difficult to validate results obtained from this software. Next steps for advancing current MSK models include improvement in computing power to allow for models with increased complexity, and improved methods of accurately measuring *in vivo* forces to validate model predictions.

2.4.3 Digital Image Correlation for Musculoskeletal Tissue Engineering

Increasing prevalence of MSK disease has motivated researchers to use tissue engineering as a strategy for understanding and treating these conditions. It has been well established in literature that MSK tissue requires an appropriate quantity of mechanical stimulation to develop properly; insufficient stimulation can result in catabolic gene expression, while excessive stimulation results in degradative enzyme production and inflammatory processes [51]. Being able to measure and characterise loading in tissue engineering constructs is therefore paramount. Although widely used in tissue engineering, conventional

strain measurement tools such as extensometers or strain gauges do not adequately capture the non-homogenous and multiaxial nature of biological tissue loading [194]. Other important considerations for monitoring biological tissues include sufficient resolution to detect small deformations in a sample and minimal contact to avoid disturbing the biomechanical environment of samples during tissue culture. Given these requirements, Digital Image Correlation (DIC) has emerged as a promising technology for strain characterisation in musculoskeletal tissue engineering.

DIC was first developed in the 1970's and innovations within this technology have allowed this technique to be applied to an expanding number of fields, such as biomechanics. DIC is a non-destructive and non-contact method of characterising material strain. The basic principle of DIC involves recording the configuration of a random specular marker pattern on the surface of a sample, taking a series of images as the sample is being deformed, and tracking the movement of the pattern via cross-correlation throughout the deformation cycle [195]. Using two or more cameras, it is also possible to use this technology for 3D strain evaluation. This method is particularly useful for tissue engineering as it allows for characterisation of samples with complex surface geometries and multiaxial strain evaluation. A sample workflow for analysing biological samples with 3D DIC is provided in Figure 11.

There are an increasing number of biomechanical applications for which DIC has been tested and evaluated. One of the earliest musculoskeletal studies using DIC involved cartilage tissue specimens. Wang et al. examined the anisotropic properties of cartilage and demonstrated that the elastic (Young's) modulus of cartilage differs based on the direction of loading [196]. In bone tissue, DIC has been compared to strain gauges used to identify high strain zones and fractures in mouse tibia undergoing uniaxial compression [197]. Results from this study concluded that DIC was able to more reliably map tibial strain and fracture zones than the strain gauges [197]. Evaluating tendon tissue with DIC has been of growing interest to researchers; a study showed evaluated strain distribution across an entire human Achilles tendon, providing an alternative to the past method of only measuring average strain with extensometers [198]. When compared with quantitative ultrasound strain measurement for tendon tissue,

DIC has shown good consistency [140, 199]. An emerging body of work has also started using DIC in tendon tissue engineering [118, 130, 131]. This represents a promising trend. As discussed in Section 2.3 of this document, most recent tendon tissue engineering studies have been limited to reporting average strain values in their constructs.

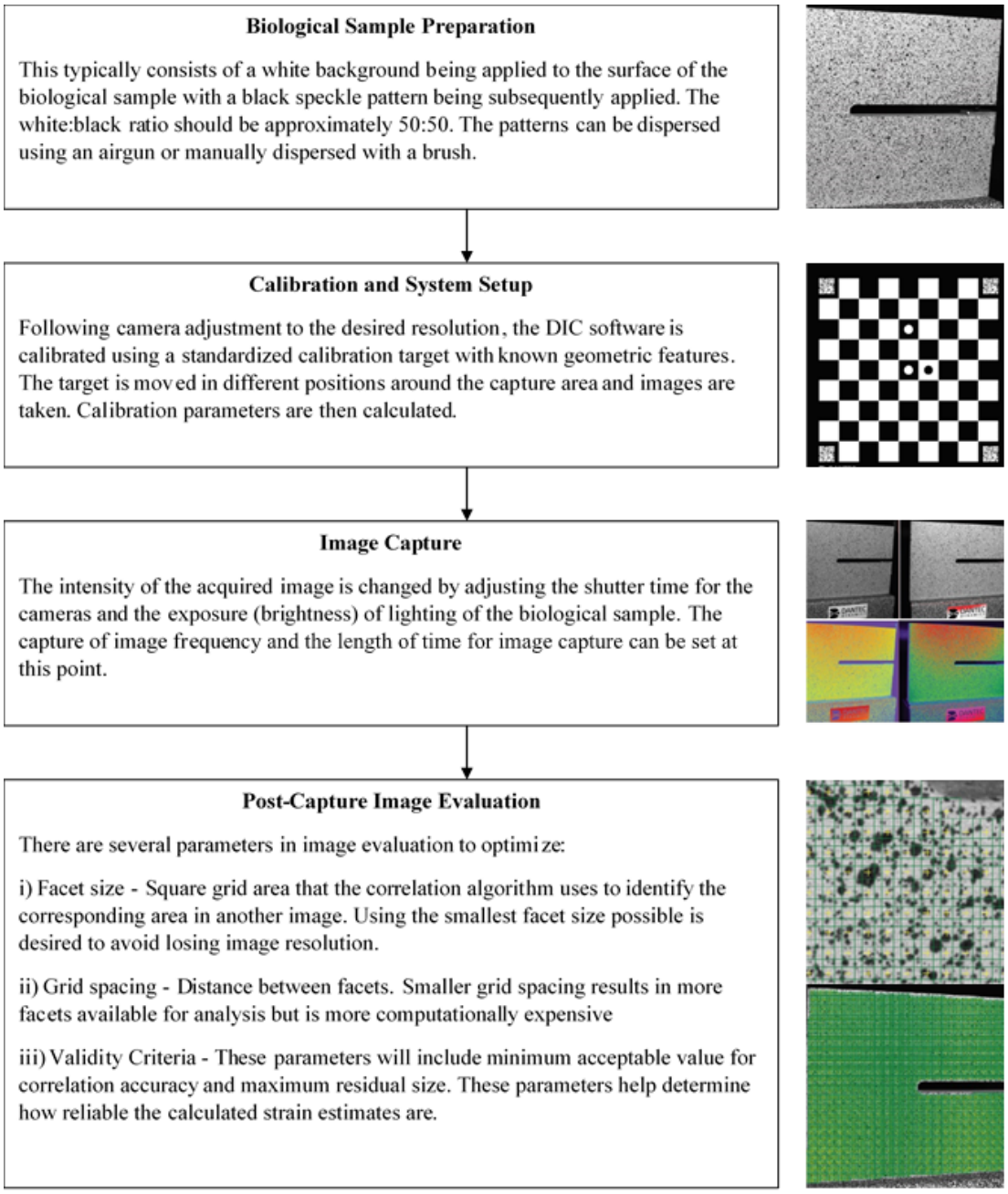


Figure 11: Workflow for DIC analysis of biological specimens. Based upon correlation algorithm parameters discussed by Palanca et al. [200] (Images in flowchart reproduced from Dantec Dynamics) [201].

DIC is an accurate and high-resolution method of evaluating global strain distribution in a sample. While this method represents a significant advancement in strain characterisation and is growing in popularity for biomechanical and tissue engineering applications, DIC is limited to providing strain estimates at the surface. Given that native tissue demonstrates non-uniform deformation between superficial and deep layers, DIC does not fully capture the behaviour of native tissue or complex 3D scaffolds that deform non-homogenously.

2.5 Chapter Summary

Tendon is a complex, nonhomogeneous tissue which relies on mechanical stimulation for healthy development. Inadequate and excessive loading are both hypothesised to contribute to tendon disease, a growing problem due to an aging demographic. Rotator cuff tears are one of the most common and debilitating tendon injuries. Despite advances in surgical methods, patient outcomes remain poor, with upwards of 40 % of rotator cuff repairs failing, depending on the degree of tear. To address this clinical need, expertise from other disciplines is required.

Tissue engineering is a promising strategy to enhance management of tendon disease. MSK humanoid robots have been identified as a platform for providing physiologically relevant loading to engineered tissue constructs. To examine whether musculoskeletal robots are an appropriate technology to use in rotator cuff tendon tissue engineering, it is important to determine whether they can provide physiologically relevant mechanical conditions for tissue growth.

The technical review section of this chapter provided context to technologies that can be appropriate for evaluating humanoid robots and discussed the benefits and limitations of each respective technology. UE MA and MSK modelling are valuable comparative tools for investigating the kinematics and dynamics of the humanoid robot. DIC has been identified as a technology for tendon tissue engineering that has distinct advantages over conventional strain measurement techniques.

3. General Materials and Methods

3.1 Humanoid Robot

The first section of this chapter provides technical details about the MSK humanoid robot used in this thesis and design alterations made for different testing conditions. The description of the MSK robot (Subsection 3.1.1) and of modifications made to the joint for tendon tissue engineering (Subsection 3.1.3) are adapted from Richter et al. and a manuscript under preparation within our research group [145, 148].

3.1.1 Original MSK Robot Shoulder

"Roboy", the MSK robot whose tendon-driven shoulder component was used throughout this study (Figure 12), was designed and developed by Devanthro, GmbH (Garching, Germany). The structural components of the robotic shoulder were constructed using aluminium rods and 3D printed polyamide Nylon 12 (PA 12) (EOS GmbH Electro Optical Systems, Krailling, Germany). The 3D printed structural components were designed using CAD software (Autodesk Fusion, San Francisco, USA). The original joint for this system consisted of a ball component, attached to an aluminium rod to comprise the 'humerus' side and a socket component, attached to the main frame of the shoulder, to comprise the 'thorax' side of the joint. The original ball and socket joint was developed to resemble the GH joint.

To control the joint movements, five myorobotic actuators were mounted on an aluminium rod stand. Actuating muscles consisted of a 100 W brushless DC motor (Maxon Motors AG, Sachseln, Switzerland), an encoder, a motor driver board, a spring, and a series of pulleys encased in 3D printed PA 12 [145]. Braided line (300lb Hercules Super Tackle 8 Strands Strong Braid Fishing Line, Hercules, Taiwan) – serving as the tendon – connected the arm of the robotic shoulder to the pulley system and DC motor in each respective actuator. Loading caused the 'tendon' line to coil or uncoil around the motor. The movement of this line was discerned by an encoder and interpreted by the motor board driver, with the signal being sent via a serial peripheral interface (SPI) cable to a field programmable gate array (FPGA) board [148]. The FPGA could in turn communicate with the motor driver board to replay movement based on encoded deformation. A proportional-integral-derivative (PID) system was running on the

FPGA to control the movement replay speed [145]. ROS Kinetic and Ubuntu 16.04 were the middleware for the FPGA. Rviz, a visualisation tool for ROS, was the graphical user interface used to record and replay muscle trajectories.

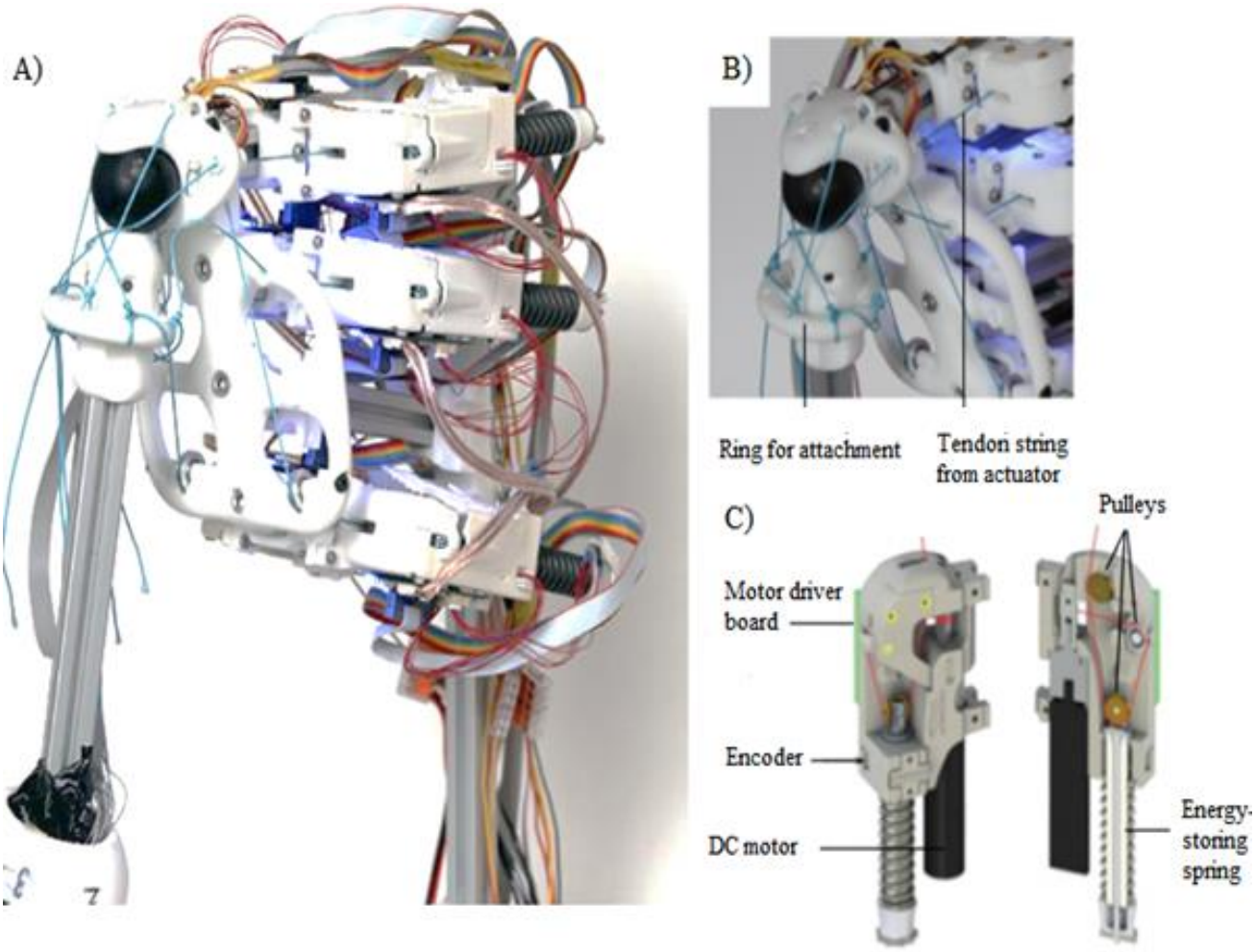


Figure 12: Key components of Roboy arm-shoulder system. A) Arm-shoulder with five actuators assembled on aluminium frame. B) Attachment of strings from the actuators to the joint. On the thorax side, closer to actuators, a socket joint is used. On the humerus side, there is a ball joint with a ring for attachment of the tendon strings. C) Internal components in the myorobotic actuators. The tendon (orange line) is routed in a triangular fashion around the pulleys to create a nonlinear net spring force [145] (Figure adapted from Mouthuy et al. and Richter et al.) [145, 148].

3.1.2 Joint and Actuator Modifications

To improve control and system range of motion, two additional robotic muscles were added to the arm-shoulder system, for a total of seven actuators being used in this study. Myorobotic actuators were arranged to mimic the anatomic location of rotator cuff muscles (Figure 13). The subscapularis, teres

minor, and infraspinatus muscles were each replicated using two myorobotic actuators. One actuator was used to mimic the supraspinatus.

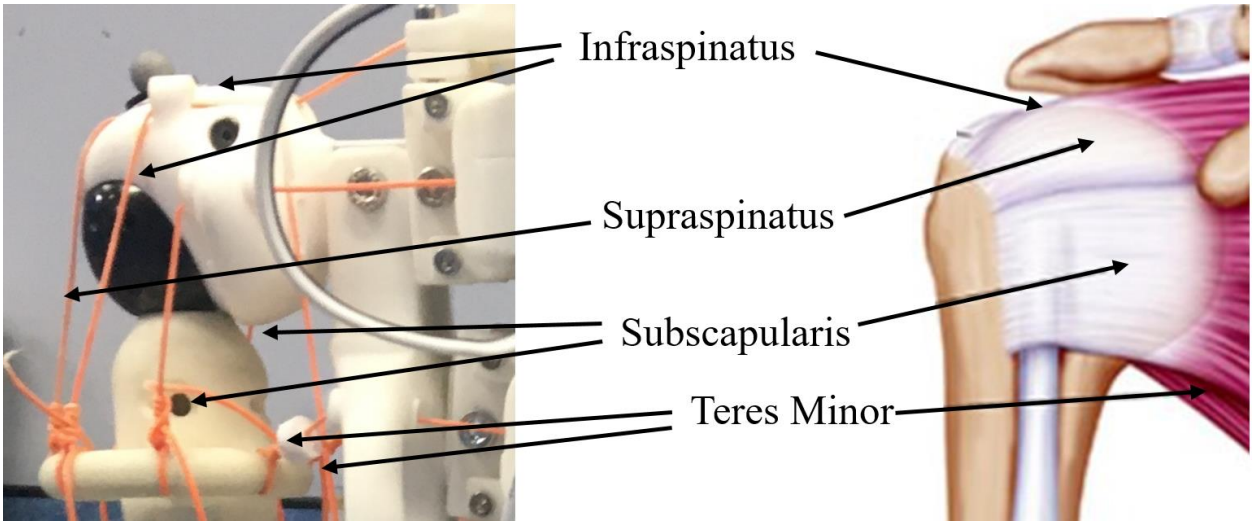


Figure 13: Configuration of actuating 'tendon' lines for the original joint on the MSK humanoid arm. Lines are arranged around the joint to imitate the anatomic location of rotator cuff tendons in the human shoulder. The infraspinatus, subscapularis, and teres minor positions on the humanoid arm each have two actuators, for a total of seven actuators contributing to movement.

Three new joint configurations were developed for the "Roboy" arm-shoulder system: a clinically used shoulder implant, a reverse ball and socket joint, and a joint designed from bone scans. The former two joint configurations were used in the motion study (Chapter 4), while the latter joint was used in strain characterisation studies (Chapter 5). Joints were attached to the humanoid arm with bolts, nuts, and washers to allow joints to be used interchangeably.

The purpose of the clinically used shoulder implant was to evaluate whether the original ball and socket joint reasonably approximated its function. Reverse shoulder arthroplasties are used clinically to improve function for patients with unstable shoulders and limited abduction due to damaged stabilising structures around the glenohumeral joint, such as torn rotator cuff muscles or severe osteoarthritis. Given that the humanoid robot lacks a deltoid muscle and stabilising ligaments around the glenohumeral joint, a reverse shoulder joint was included in this study as it was expected that this conformation would have greater

ROM compared to the original ball and socket joint configuration. The joint designed for DIC was specially configured to enable attachment of scaffold materials.

Joint Based on Clinical Implant

A bipolar shoulder implant (Waldemar-Link Orthopaedics GmbH, Hamburg, Germany) comprising a titanium stem, ceramic head, and ultra-high molecular weight polyethylene cup was modified to replace the ball and socket joint in the "Roboy" shoulder (Figure 14). The ceramic head was cut from the stem and was screwed into a plastic mount at a University of Oxford departmental workshop (Institute of Biomedical Engineering, Oxford UK). This component was then fit over an aluminium rod to comprise the 'humeral side'. The polyethylene cup from the implant was fitted into the socket of the initial joint.

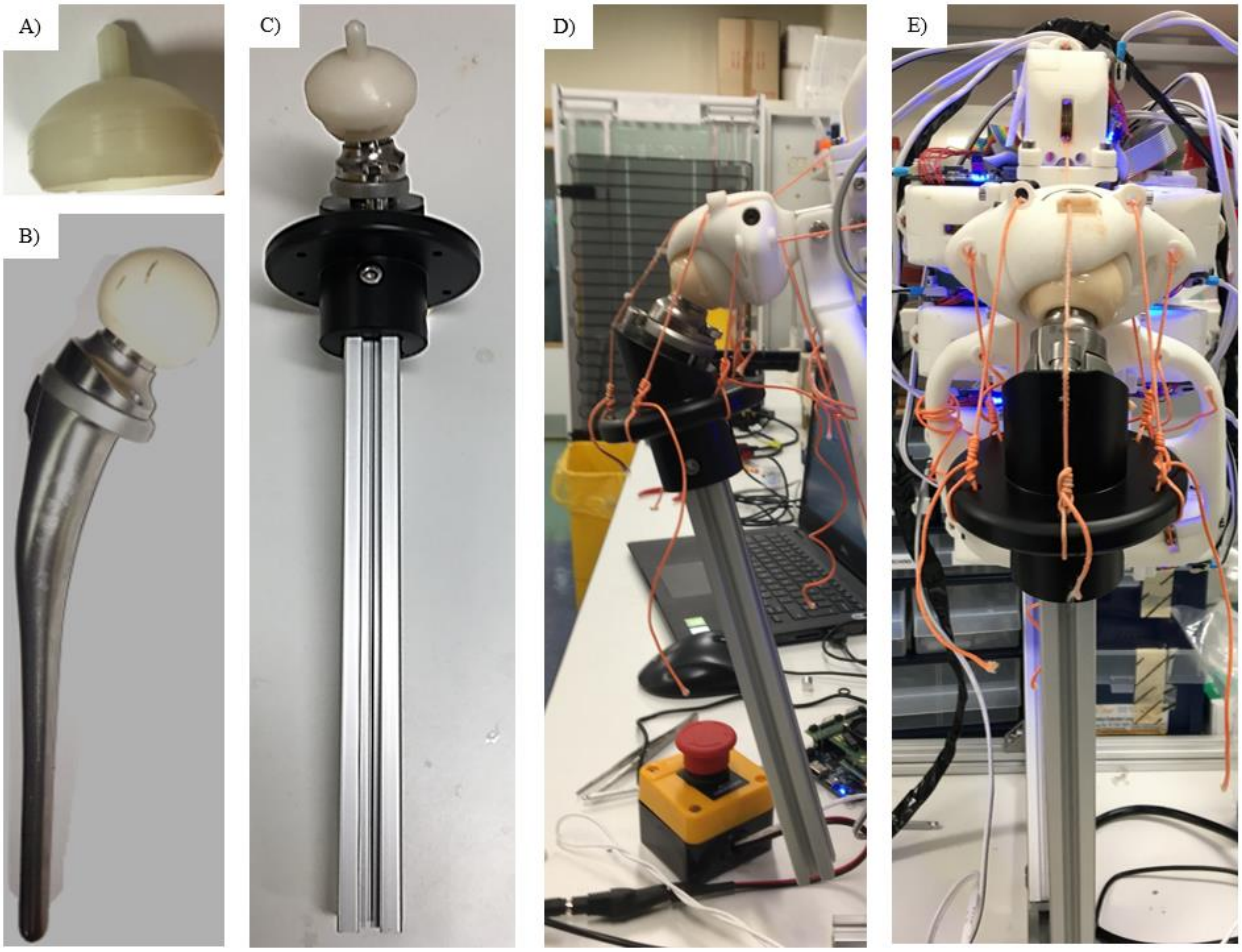


Figure 14: Adaptation of Roboy arm-shoulder system using clinical implant. A) Polyethylene cup from the initial implant. B) Titanium stem and ceramic head from clinical implant. C) Adapted humerus component based upon clinical implant. D) Front view of clinical implant joint. E) Side view of clinical implant joint.

Reverse Shoulder Joint

A reverse shoulder was developed for the “Roboy” arm-shoulder system (Figure 15). The joint was designed by modifying existing CAD files from the original thorax and humerus components produced by the “Roboy” development team (Devanthro GmbH, Garching, Germany). On the ‘humerus’ side, the modified socket consisted of an angled cut part that was attached to an aluminium rod; the ‘thorax’ component was altered from the original design and fitted with a ball. A medical 3D printing company (3D LifePrints, Oxford, UK) prototyped reverse ball and socket joint components with dental model resin (Formlabs, Somerville, USA).

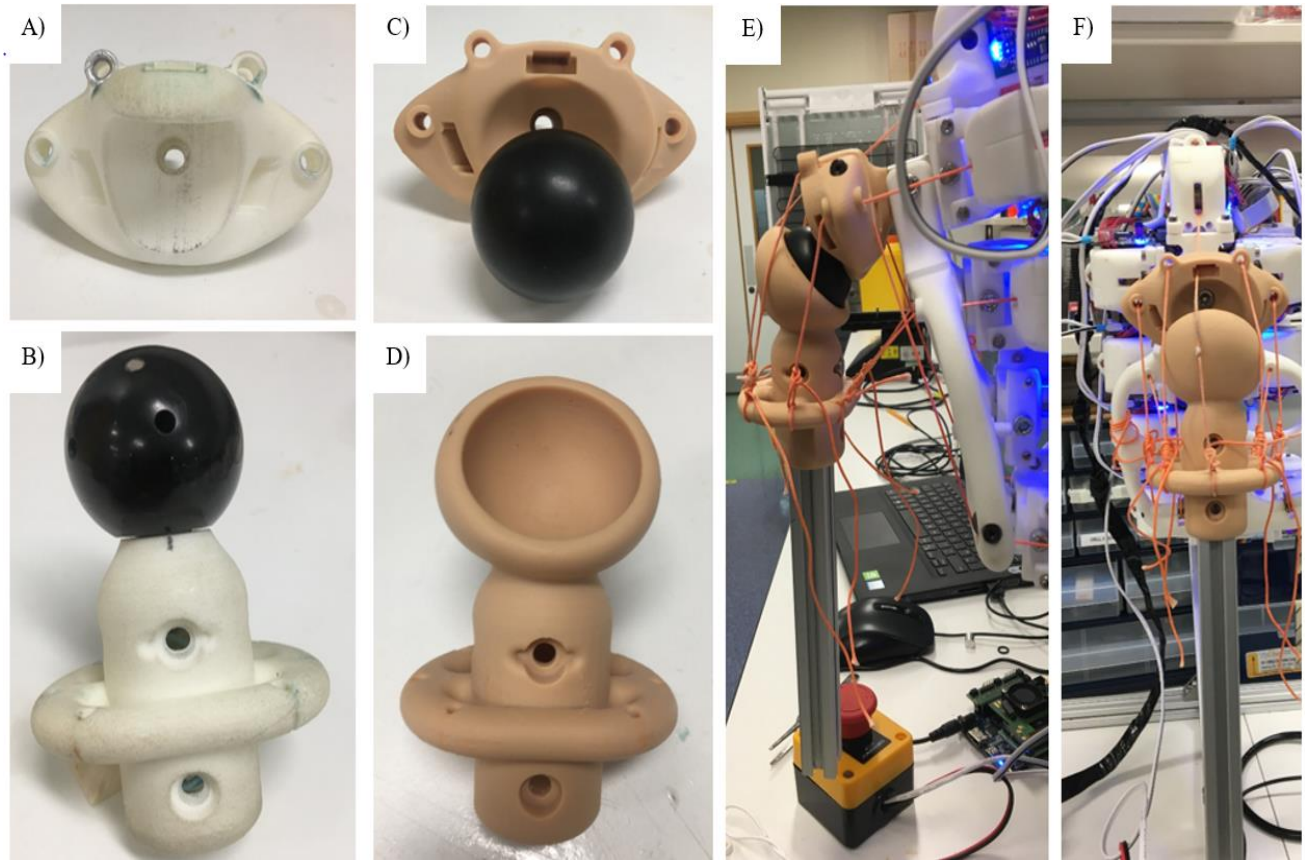


Figure 15: Reverse shoulder configuration. A) Original socket component attached to thorax side of robot. B) Original ball component attached on humerus side. C) Modified ball component attaching on thorax side of robot. D) Socket component attaching on humerus side. E) Front view of modified robotic arm. F) Side view of modified robotic arm.

Joint for Strain Analysis

Mouthuy et al. developed an additional joint model based upon 3D scans of scapula and humerus bone models (AnatomyStuff, Health Books UK Ltd, Aberystwyth, UK). These scans were subsequently merged into CAD drawings of the original robotic shoulder and printed with a polyamide resin (3Dsystems, High Wycombe, UK). A clinical implant was used to ensure smooth movement of the humerus head in the glenoid cavity [148]. A stemless humeral implant made of cobalt chrome alloy was fixed to the humeral side and a polyethylene glenoid implant was attached on the thorax side (Zimmer Biomet, Warsaw, USA). A socket was cut on the humerus side to allow space for a chamber to be used in strain characterisation experiments (Figure 16). The joint was stabilised with elastic bands that served as artificial ligaments (Vancool, Guangdong, China) [148].

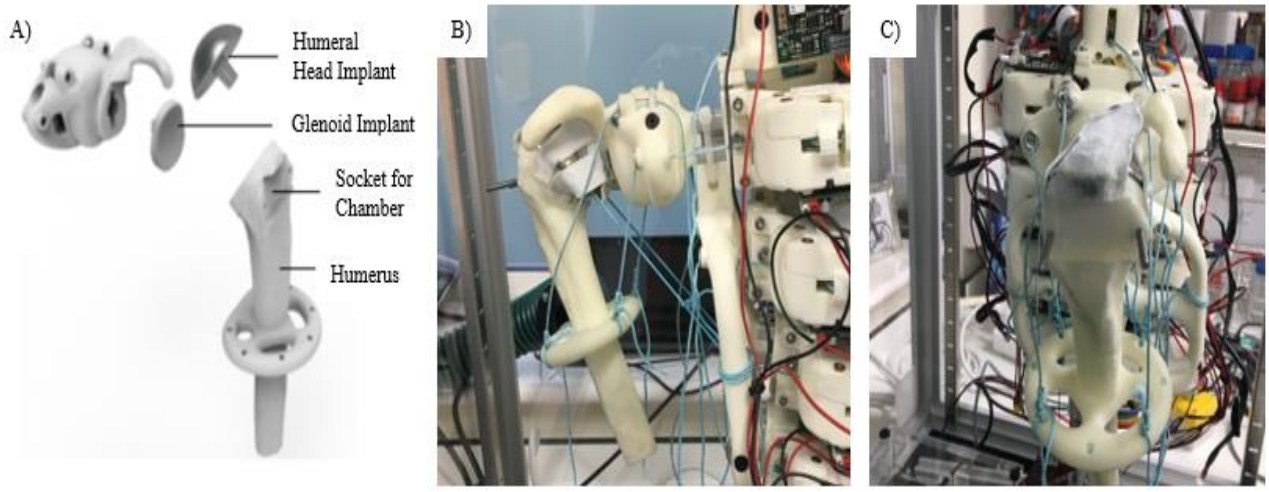


Figure 16: Modified shoulder joint presented by Mouthuy et al. for tendon tissue engineering applications. A) Exploded view of components in modified joint, reproduced from manuscript under review by Mouthuy et al. [148]. B) Front view of joint. C) Side view of joint.

3.2 Motion Study and MSK Modelling

The second section of this chapter describes the methods used in the motion study, which compare the kinematics and kinetics of the robotic arm with a reference data set of forty healthy human participants.

3.2.1 Ethics Approval for Study

Research ethics approval for the motion study, "Validation of shoulder model through motion tracking study" (reference number: R65527/RE001), was approved by the University of Oxford's Central University Research Ethics Committee (CUREC).

3.2.2 Study Participants for Motion Study

Forty participants (23 male, 17 female; mean age 28.3 years [range 20.5 – 36.9 years]; mean height 1.75 m [range 1.56 – 1.93 m]) were recruited from the University of Oxford. Individuals participated in the study voluntarily and received no compensation for participation. Prior to volunteering for the study, participants received an advertising poster, information sheet, consent form, and instructions to bring a tank top/vest to wear during data collection for the study. Upon entering the motion lab, participants were presented with a consent form to sign, an information sheet, and the opportunity to clarify any questions they had prior to data collection. Following signing of consent forms, participants completed a measurement form where age, gender, height, and weight were recorded. Participant height and weight were measured using a stadiometer and a scale (EKS Scales, Hong Kong). Participant IDs were pseudonymised to ensure confidentiality. While forty participants were recruited for this study, the data of one participant was not evaluated due to poor data quality.

There were three inclusion criteria for study participants:

- Capable of freely giving informed consent
- Over 18 years of age
- No neurological or musculoskeletal pathology that would limit ability to complete tasks.

There were three exclusion criteria for study participants:

- History of UE surgery
- History of shoulder injury within the past year
- Physical disability or injury limiting shoulder movement

3.2.3 Equipment and Software Details

The study took place at the Oxford Gait Lab (Oxford, UK) (Figure 17). A near-infrared 16-camera Vicon T-Series motion capture system (Vicon Motion Systems, Oxford, UK) was used to track 9.5 mm diameter retroreflective passive markers (B&L Engineering, Santa Ana, USA) in this study. Data were collected at a rate of 100 Hz. Vicon Nexus™ (v. 2.9.2, Vicon Motion Systems, Oxford, UK) was used to acquire, process, and analyse motion data in this study. Analysed data were exported in .c3d and .csv format.

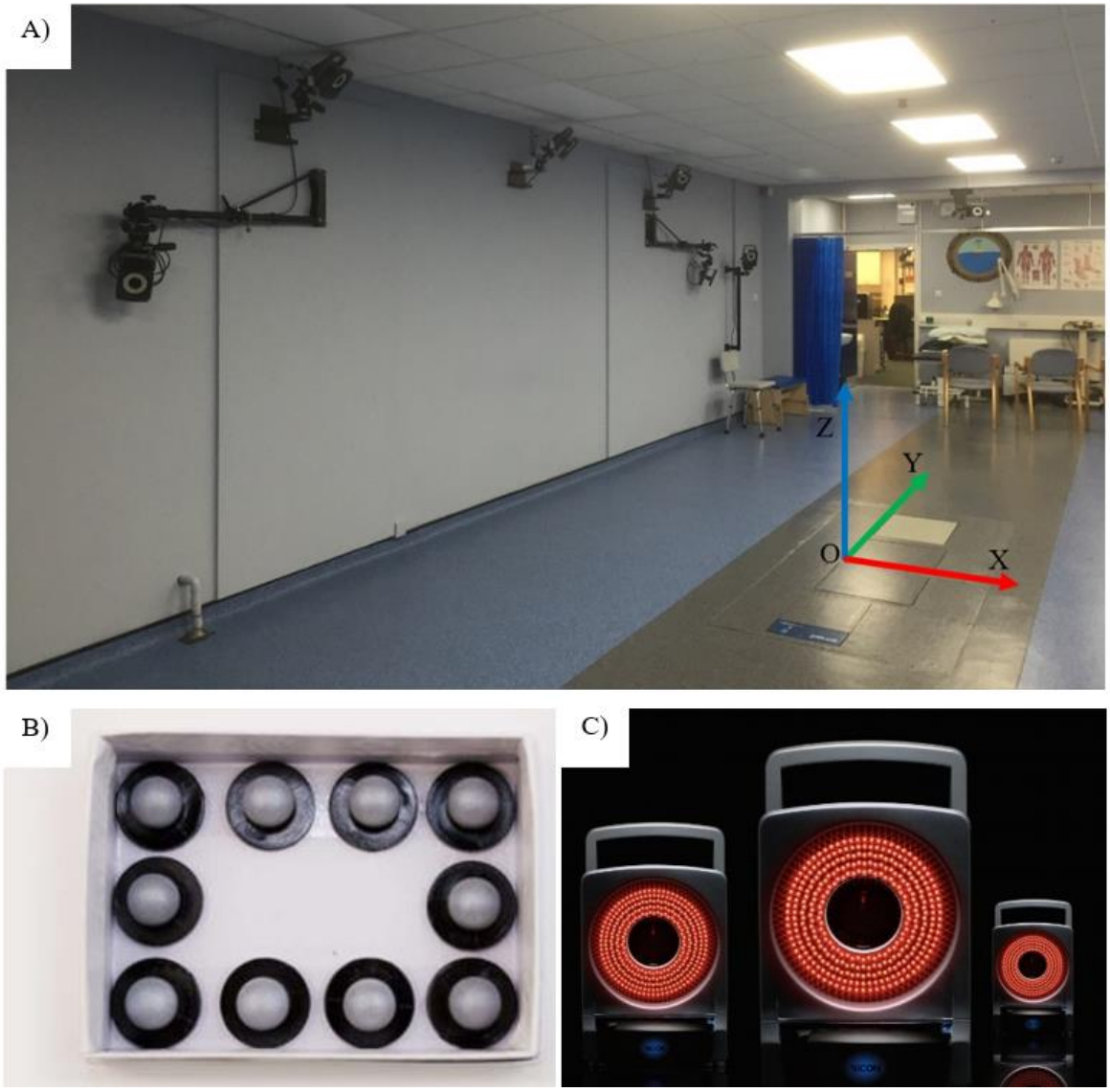


Figure 17: Equipment used in motion study. A) Oxford University Hospitals Gait Lab with global axes used for motion capture in this study with "O" marking the volume capture point of origin. B) Ø 9.5 mm retroreflective pearl markers used in motion capture study C) Vicon T-Series near-infrared motion capture cameras [202].

3.2.4 Quality Assurance and Calibration Procedures

Calibration of the camera system and designation of capture volume origin were performed prior to every data collection session to ensure consistency in data that were collected. A calibration object with LED markers (Vicon Motion Systems, Oxford, UK) was used to calibrate the room and use the relative position of the cameras to determine room geometry (Figure 18). To set the origin of the capture volume and allow the position of the force plates relative to the cameras to be determined, the calibration object was placed on the floor against a floor plate in the motion lab, with the wand handle facing the + y-axis. To ensure that the origin of the capture volume was properly set, and that the calibration had been performed correctly, the calibration object was then rotated 180^{o} from where it was placed for establishing the capture volume origin. Tolerance levels for camera error were set to be less than 2 mm.

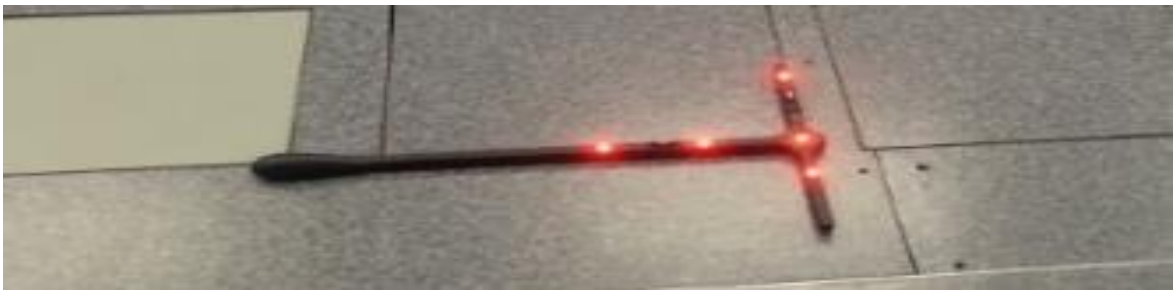


Figure 18: Object used for calibration procedure and designation of capture volume origin.

3.2.5 Task Protocol

Tasks for this study were completed with the right arm only. The supraspinatus is primarily responsible for abduction up to 15^{o} and assists the deltoid with motion up to 90^{o} in healthy shoulders [41]. Upwards of 90^{o} abduction, motion contributions from the supraspinatus are less significant [203]. Furthermore, rehabilitation of rotator cuff injuries typically involves motion up to 90^{o} ROM [99-101, 105, 204]. In consideration of these factors, the exercises completed during motion capture sessions for this study are listed in Table 8.

Each task was completed at two movement speeds: a slow, controlled movement over a 6 s interval for the 30º task and 18 s for the 90º task (for a target movement speed of 10 deg/s) and a faster movement over a 2 s interval for the 30º task and 6 s for the 90º task (for a target movement speed of 30 deg/s) [209]. Tasks were timed to help identify limitations in the movement speed of the humanoid arm and to evaluate the ability of the arm to replicate early-stage and later stage rehabilitation movements. Slow, controlled movements are typically completed in early phases of physical therapy, with faster isokinetic exercises being used to represent healthy shoulder function [205, 206].

Table 8: List of exercises completed in motion study

Order	Task	Description
1a, 1b	Abduction to 30º	Starting with arms at side of the body with the dorsal aspect of the hand facing outwards (i.e. palmar aspect facing towards the body), participant will move their upper extremity 30º laterally in the coronal plane. Once participant has reached 30º, position will be held for 5 seconds before returning to initial position.
2a, 2b	Abduction to 90º	Starting with arms at side of the body with the dorsal aspect of the hand facing outwards (i.e. palmar aspect facing towards the body), participant will move their upper extremity 90º laterally in the coronal plane. Once participant has reached 90º, immediately return to initial position.

One researcher collected data for all human and robotic trials to avoid marker placement inconsistency between researchers. Standardised instructions and a demonstration were provided to each human participant; participants were told to start the movement with their arm by their side, with the dorsal aspect of their hand facing outwards and thumb facing forwards. Participants were told to keep the remainder of their body as still as possible during task completion, to keep their thumb facing forwards to avoid rotation of the forearm during abduction, and to only abduct with their arm by their side (i.e. to limit movement outside of the scapular plane). Before completing the desired movement, participants were asked to move their arm to the desired range of motion, which was verified by the assessor and confirmed to be within a 5º location of the desired range of motion. This location was shown on live stream from a video camera that participants were able to view while completing the task. To ensure reliability in timing, the assessor used an on-screen stopwatch and counted out loud for participants as they completed the movement. One representative trial was recorded per task for each participant. This

decision was based on existing literature, which states that “one representative trial can generally be used for clinical decision-making” in MA studies [207, 208].

For movement trials involving the robotic arm, the assessor recorded a movement for the arm to the desired range of motion and speed, programming the robotic arm to replay the movement. The recording was done by manually moving the arm to the desired ROM at the desired angular velocity. The software used to control the robot was set to replay these movements (more details on control of the humanoid robot are provided in Section 3.1). A movement was programmed five times per task at 10 deg/s and twenty times per task at 30 deg/s. The entire repertoire of tasks was completed for the original ball and socket joint. Subsequent joint configurations (Section 3.1) only completed the “abduction to 30º” and “abduction to 90º” tasks at 30º/s. The same PID controller settings were programmed into the robotic system for each joint configuration to ensure consistent comparison of performance during task completion.

3.2.6 Kinematic Model

The model and marker protocol for this study was an adaptation of the widely used upper body Plug-in Gait® (PiG) model, developed by Vicon [202]. The marker protocol used for this study consisted of four segments (i.e. thorax, shoulder, radius, hand) and three joints (i.e. shoulder 3 DoF, elbow 2 DoF, wrist 2 DoF). As with upper body PiG, shoulder kinematics were approximated to the GH joint (described as shoulder joint centre in the model); scapular contributions to motion were neglected. The default PiG segment axes and angle calculation methods were used. In contrast to the PiG model, the marker protocol used for this study additionally consisted of a marker cluster on the right upper arm and a marker cluster under the clavicle marker on the torso. Head, hand, and left arm markers were not used in this study. For the humanoid robot, wrist, back and the left shoulder markers were not used as the system only has a right shoulder joint. Marker locations and descriptions are provided in Figure 19 and Table 9, respectively.

For human participants, markers were either attached to the anatomical landmarks described in Table 9 using double-side hypoallergenic tape (Tape Range Distributors Ltd, Hyde, UK) or constructed virtually using a marker wand (Figure 19-G). Elbow and wrist joint centres were calculated as the midpoint between their respective medial and lateral markers. The shoulder joint centre was calculated using a method previously described by Rab et al [209].

For the robotic arm-shoulder system, markers were attached to points which were analogous to anatomical landmarks on human participants. To ensure consistency between trials, locations for marker placement on the robotic system were indicated using a permanent ink pen. The elbow joint centre was calculated as the midpoint between medial and lateral 'elbow' markers for the robot. As the right shoulder marker for the robotic arm was placed directly superior to the shoulder joint centre, the offset from the 'RHSO' marker was measured using a clinical calliper. This distance was measured for each robotic joint configuration and subsequently changed in the program code to reflect different offsets in shoulder joint centres. A copy of the modified program code used for kinematic modelling of the human participants is provided in Appendix A of this thesis.

Table 9: Marker locations used for motion study

Marker Label	Marker Name	Anatomic Position
LFSO	Left Shoulder	On the acromion
RHSO	Right Shoulder	On the acromion
CLAV	Clavicle	On the jugular notch where the clavicles meet the sternum
CHE(A-D)	Chest Cluster	Below the jugular notch on the manubrium. There are four markers in this cluster, labelled clockwise from the top left corner (A), to the bottom left corner (D)
RUP(A-D)	Right Upper Arm Cluster	On the lower lateral 1/3 surface of the right upper arm. There are four markers in this cluster, labelled clockwise from the top left corner (A), to the bottom left corner (D)
RELL	Right Elbow (L)	On the lateral epicondyle
REM	Right Elbow (M)	On the medial epicondyle
RWUL	Right Wrist Marker (U)	Ulnar styloid†
RWRA	Right Wrist Marker (R)	Radial styloid†
RBAK	Right Back	Over the right scapula†
T10	10th Thoracic Vertebra	On the spinous process of the 10th thoracic vertebra*

C7	7th Cervical Vertebra	On the spinous process of the 7th cervical vertebra*
STRN	Sternum	On the xiphoid process of the sternum*

†Markers not included for humanoid robot
*****Markers placed virtually with wand for human participants

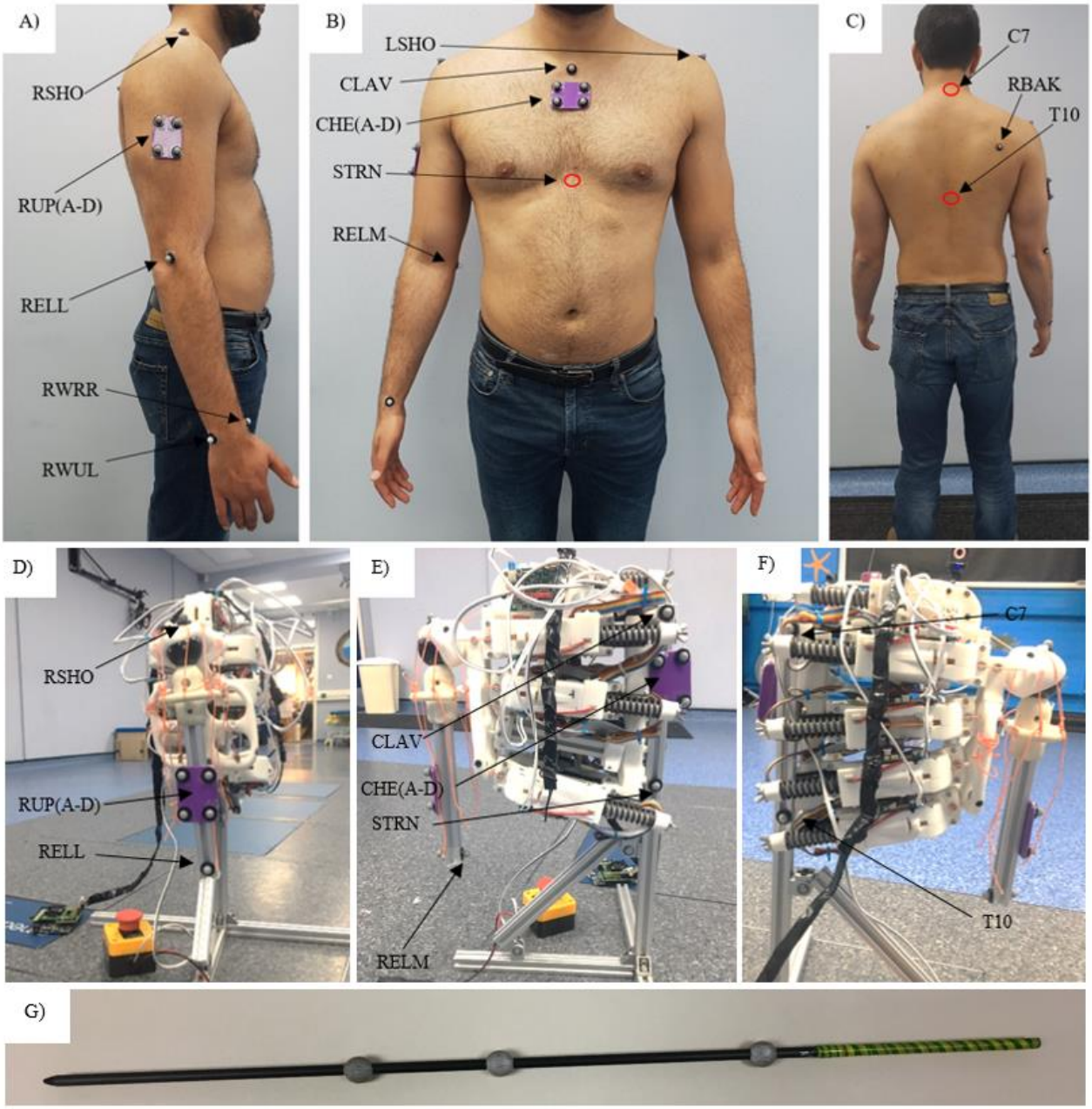


Figure 19: Marker placement protocol used in study. A – C) Marker placement locations for human participants. Locations indicated by red ellipses (i.e. STRN, C7, and T10) have markers constructed virtually using a pointer wand. D – F) Marker placement locations on Roboy arm-shoulder system. G) Wand used for virtual construction of C7, T10, and STRN markers for human participants.

3.2.7 Motion Capture Data Processing

Raw data were processed and filtered in Vicon Nexus™. Upon reconstruction and labelling of marker trajectories, gaps smaller than 5 frames (0.05 seconds) were filled using a Woltring spline interpolation function in the software [210]. Larger gaps were filled using the "Rigid Body" filling option, whereby gaps were filled based on the trajectory of other markers sharing a rigid relationship with the missing marker. Noise in the data were filtered using a spline Woltring filter [211]. Given small variations in starting position due to participant body habitus, motion data for angles were standardised such that every participant's motion started at 0^{o} abduction. Motion data were similarly standardised for the humanoid arm such that the starting position for a movement was described as being 0^{o} abduction. A pipeline further detailing all steps of data collection and processing is provided in Appendix B.

3.2.8 Kinetic Modelling for Human Participants

The AMS was used to estimate *in vivo* supraspinatus forces for human participants in this motion study via the AnyMoCap application (v.7.3.0, AnyBody Technology, Aalborg, Denmark). The DSEM and a rigid body spine model developed by Zee et al. were the upper body models implemented for this study [189, 190]. Default UE segment inertial parameters in the AMS are taken from anthropometric data published by Winter [212]. Muscles were modelled using a simplified Hill-type muscle model and 3^{rd} order polynomial recruitment and load-sharing algorithm [213]. In the AMS, muscle-tendon units are differentiated into smaller segments. Total muscle forces in this study were computed as the sum of all segments for a particular muscle.

The AnyMoCap application uses linear model scaling to estimate kinetics [214, 215]. Labelled marker trajectory data were imported into the AMS as .c3d files. Participant height and weight data were directly input into the AMS. Noise from data imported into the AMS was filtered using a 2^{nd} order zero-phase Butterworth filter with a cut-off frequency of 10 Hz. Using filtered motion study and participant anthropometric data, an optimisation procedure scaled the upper body model and optimised marker positions to re-calculate joint angles. Following this optimisation procedure, inverse dynamics analysis

was completed to estimate joint moments, reaction forces, and muscle forces. Force estimates were obtained for both movement tasks completed at 30 deg/s. It was chosen to model force profiles for the higher speed movement trials only, as this movement speed better represents the abduction exercises completed by physical therapists at later stages in rehabilitation [99-101, 105, 204].

The supraspinatus forces extracted from the AMS were presented for comparison of force measurements from the humanoid arm. Infraspinatus, teres minor, subscapularis, and lateral deltoid muscle forces, glenohumeral joint moments, and glenohumeral reaction forces were extracted from the program and are presented in Appendix C. Verifying the sensitivity of model parameters is of vital importance, given that there are no direct comparison methods currently available to ensure accuracy of model outputs [216]. Further details of study-specific changes to the standard AnyMoCap application and a sensitivity analysis showing the effect of changing the muscle recruitment algorithm is provided in Appendix C.

3.2.9 Force Measurements for Humanoid Robot

Force data were only recorded for the 30 deg/s movement trials. Force data for the robotic system were measured using a load cell (model WMC-450N, Interface Force Measurements Ltd, Crowthorne, UK) and recorded using a high-speed data logger (model 9330-MSDI-IP43, Interface Force Measurements Ltd, Crowthorne, UK) at a frequency of 10 Hz. The load cell was fixed to the robotic system on the ‘humeral’ side and to an actuating muscle in the ‘supraspinatus’ position using braided ‘tendon’ line (300lb Hercules Super Tackle 8 Strands Strong Braid Fishing Line, Hercules, Taiwan).

3.3 Analysis of Scaffolds Using DIC

This section describes use of DIC to characterise strain in tissue engineering scaffolds undergoing mechanical loading with the humanoid arm-shoulder system.

3.3.1 Scaffold Description

A small, flexible bioreactor chamber was developed and patented by Mouthuy for use in tissue engineering [148, 217]. The scaffold matrix material within the chamber is made of electrospun polycaprolactone (PCL) filaments (Apollo Scientific Ltd., Cheshire, UK). These fibres are contained by an impermeable membrane (TFL-2EA, thickness: 50µm, Permali Gloucester Limited, Gloucester, UK) fixed into 3D printed inserts (3Dsystems, High Wycombe, UK), which help maintain the sterility of tissue growing in the bioreactor chamber (Figure 20). There are small holes in the inserts which allow tubing to be fit through the chamber, allowing perfusion of nutrients and waste removal during incubation. To fix the chamber to the robotic arm, the scaffold is fit into a modified joint developed for the arm-shoulder system (previously described in Section 3.1.2).

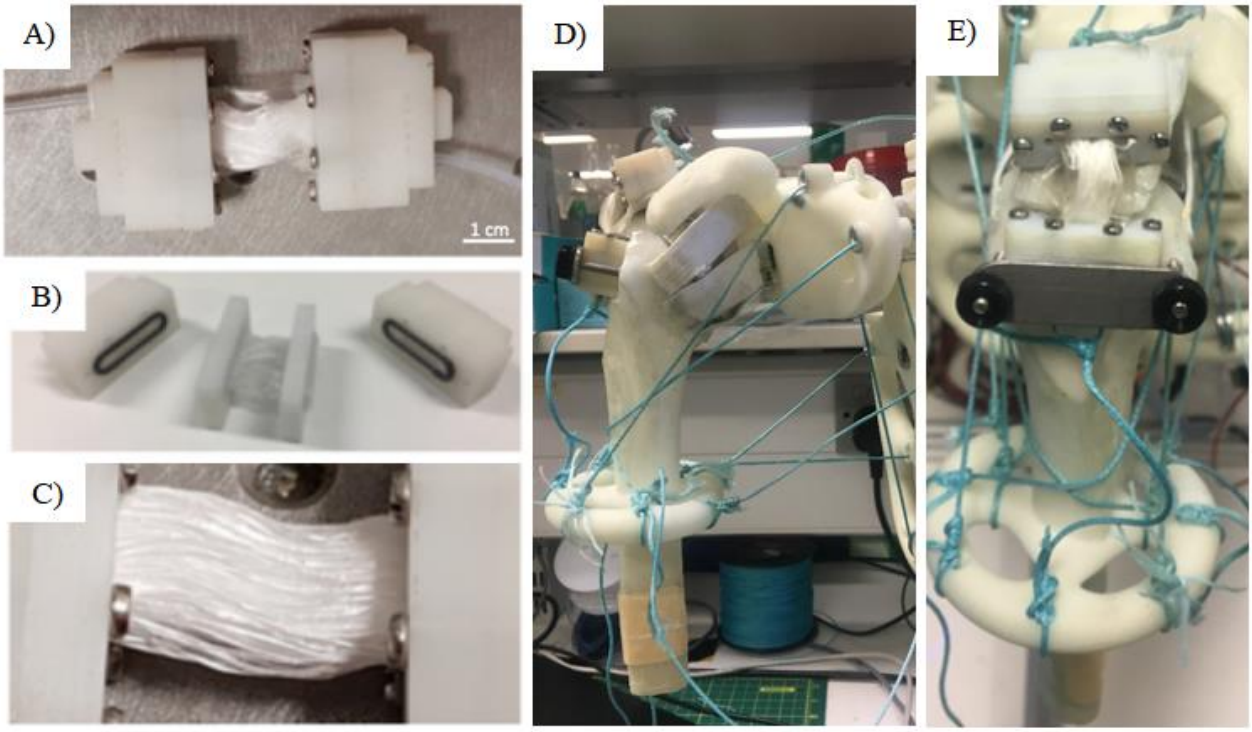


Figure 20: Bioreactor chamber scaffold and attachment to 3D printed shoulder. A) is the assembled bioreactor chamber shown with tubing which allows for media exchange, B) is an exploded view of the bioreactor chamber, C) the PCL filaments in the chamber that serve as a scaffold for tendon cells, D) and E) offer front and side views of the 3D printed shoulder, respectively, with a bioreactor chamber fit into the specially designed socket [148].

3.3.2 Preparation for DIC

To prepare samples for DIC imaging, a random speckled pattern is required for the surface of the material [200]. A generic white acrylic surface primer coating from a canister (Rust-Oleum White Surface Primer, UK) was applied to the filaments of three scaffold chambers. After 5 minutes of drying, a black acrylic spray paint (Rust-Oleum Matte Black, UK), was applied using a fine bristled brush to ensure an evenly coated random speckled pattern. The ratio on the surface of the sample was approximately 50 white: 50 black (Figure 21). After preparation, the chambers were left to dry for approximately 15 minutes.

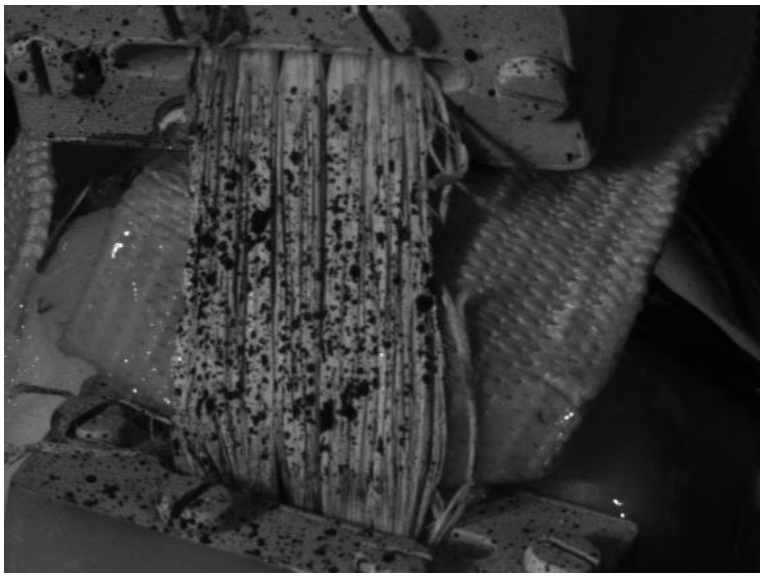


Figure 21: Speckle pattern applied to scaffold filaments.

3.3.3 Equipment Details and Testing Protocol

The commercially available Digital 3D Image Correlation System Q-400 (Dantec Dynamics, Bristol, UK) was used to estimate strain of the scaffold materials (Figure 22). The system comprises two cameras and a monochromatic LED. Force data were simultaneously measured using a load cell (model WMC-450N, Interface Force Measurements Ltd, Crowthorne, UK) and recorded using a high-speed data logger (model 9330-MSDI-IP43, Interface Force Measurements Ltd). DIC data and force data were collected at a frequency of 10 Hz. Data were analysed using proprietary DIC software (ISTRA 4D v4.4.7, Dantec Dynamics, Bristol, UK).

Three bioreactor chambers were tested, and each completed an abduction-adduction motion (between +20^{o} to -20^{o}). Each movement was recorded for an interval of 15-30 s. With three trials taken for each bioreactor chamber, a total of 9 trials were completed. Chambers were loaded onto the 3D printed shoulder joint in the position of the supraspinatus tendon.

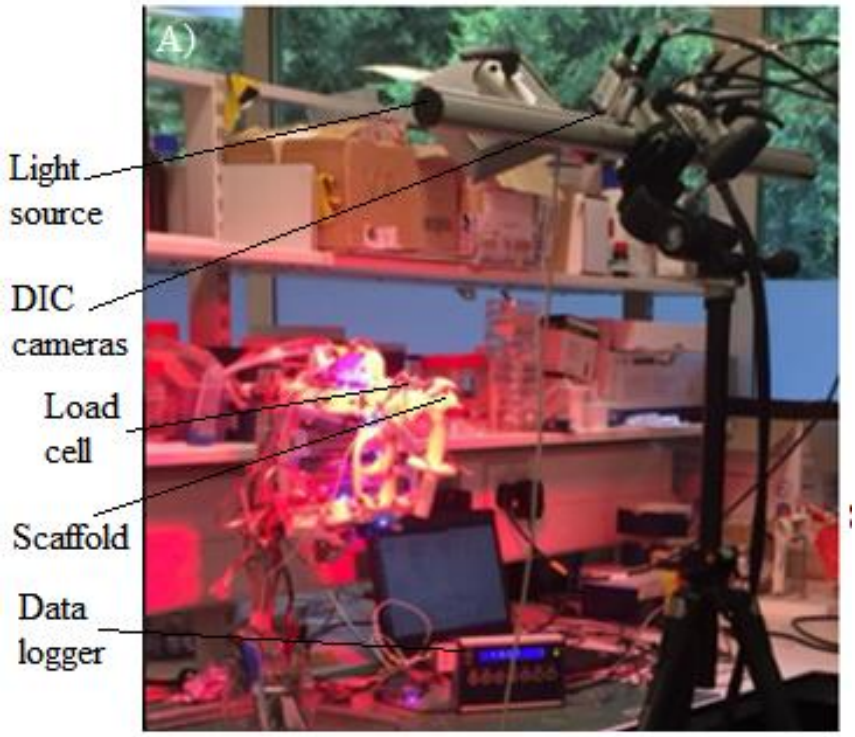


Figure 22: Experimental Setup for DIC strain evaluation

3.3.4 Camera Setup and Calibration

Camera shutter time and aperture were adjusted when setting up the system to ensure that the sharpest quality image would be obtained for capture. Shutter time for all sessions ranged between 5-25 ms, depending on time of day and lighting conditions, while aperture ranged in value from 8-12. Prior to data collection, a calibration procedure was performed to set projection parameters and define the region of interest for capture. A black and white calibration plate with a known geometry (Figure 23) was held in front of the camera at alternating angles and orientations for 10 images. The calibration procedure was

known to be complete when the residuum for cameras was less than 0.5 pixels. The target values for calibration and camera setup were described in the ISTRA 4D user manual [201].

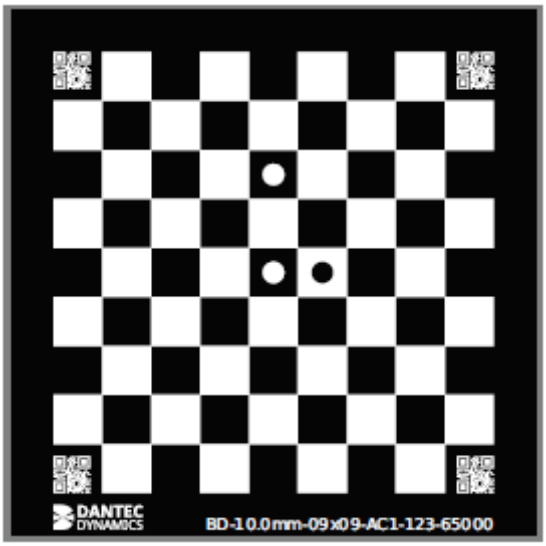


Figure 23: Example of defined calibration target for system.

3.3.5 Evaluation and Data

To simplify the investigation and allow for comparison with conventional strain testing equipment, longitudinal (y-direction) tensile strain was analysed, given that it was the most relevant deformation for the bioreactor chamber. Data from captured images were evaluated according to instructions outlined in the ISTRA 4D user manual [201]. Residuum, facet size, and search grid radius[‡] were adjusted to provide adequate resolution for pattern detection on the scaffold. A spline filter available within ISTRA 4D was used to smooth results by a factor of -0.1. Processed data were exported from ISTRA 4D in .csv format.

3.3.6 Validation

To validate strain data obtained using DIC, destructive stress-strain testing was done on the three bioreactor chambers. Data were collected using tensile stage (5 kN load cell, Zwick Roell Group, Ulm, Germany)

[‡] Residuum was changed from 20 to 2 to reduce uncertainty. Facet size was set to be between 33-37, and search grid radius was set to 200 pixels. These modifications were made to optimise accuracy of results, amount of data collected, and computational time for the model.

applying strain at a rate of 5 mm/min. Force and elongation were recorded and exported in .csv format; Young's Modulus, ultimate stress (MPa), and breaking strain (%) were subsequently calculated.

3.4 Statistical Analysis

GraphPad software (GraphPad Prism v.8.4.3, San Diego USA) was used for statistical analyses. Parametric testing of outcome variables was used where possible, given its superior power to detect differences between normally distributed groups of data [218, 219]. The D'Agostino-Pearson and Shapiro-Wilk tests were used to evaluate normality [220, 221]. Non-normally distributed data are presented as median and inter-quartile range. The Mann-Whitney *U* test was used for statistical comparison of non-normally distributed data. Normally distributed data are presented as mean and standard deviation (SD) unless otherwise indicated. Normally distributed data were compared using *t*-tests. Statistical significance for all data was determined at $p < 0.05$.

4. Evaluation of Musculoskeletal Humanoid Robot as a Platform for Rotator Cuff Tendon Tissue Engineering

4.1 Introduction

With an aging demographic and growing rates of obesity, rotator cuff tendon injuries are a common cause of mobility related impairment and present a significant socio-economic burden [5]. Rotator cuff tears present most commonly in the supraspinatus tendon. Despite a high prevalence of rotator cuff injury, patient outcomes remain poor; it is estimated that upwards of 40 % of rotator cuff repairs fail within the first few months post-operatively [7-10]. Development of engineered tendon grafts for clinical use is a promising strategy to address this growing challenge.

Conventionally, tissue engineering involves the complex interplay of gas exchange, nutrient and waste transfer through the system, temperature and pH control, and maintenance of a sterile environment. Unlike conventional methods of tissue culture, *in vitro* tendon tissue engineering additionally involves provision of mechanical cues to the culture. Evidence has consistently demonstrated that provision of dynamic loading to tendon tissue results in improved mechanical properties, increased ECM deposition, and improved cellular differentiation when compared to static culture [148]. Tendon mechanobiology studies further suggest that the type and direction of mechanical stimulation applied will have distinct effects on tendon properties at a cellular level [17, 30-32]. Clinical imaging studies have shown that tendon tissue experiences multiaxial loading and deforms non-uniformly *in vivo* [25-27, 140]. Collectively, evidence suggests that *in vitro* systems should attempt to imitate the mechanical environment of native tendon tissue as closely as possible.

A major limitation of current bioreactor systems is their limited ability to adequately replicate *in vivo* mechanical loading. Most current bioreactors only apply cyclic uniaxial or biaxial linear tensile loading that results in uniform deformation within tissue constructs. To produce clinically useful tissue grafts, more advanced bioreactor systems are needed. Mouthuy and Carr have stated that future bioreactors need to provide physiologically relevant stresses to tissue constructs and adapt movement patterns in consideration of anatomic location [13].

To achieve these goals and overcome limitations associated with conventional tendon bioreactor systems, MSK humanoid robots have been proposed to enhance tendon tissue engineering [13]. MSK robots rely on tendon-driven systems, whereby tension applied via a string cord causes the actuation system to compress an energy-storing spring and respond to the tensile loading correspondingly [13, 222]. By having similar dimensions and structure to human limbs, MSK humanoids are hypothesised to imitate the motion observed *in vivo* while actuating these structures. Furthermore, since the number of degrees of freedom and arrangement of actuators is designed according to the anatomic position of analogous muscles, the direction and types of loading provided by MSK robots are hypothesised to be physiologically relevant [142-145]

To validate whether MSK robots are a viable platform for tendon tissue engineering, it is important to compare the kinematic and kinetic profiles of humanoids with those of healthy human participants. Motion analysis (MA) is a tool which is growing in popularity to quantitatively assess and characterise UE kinematics. While there is no widely available method to directly measure *in vivo* muscle forces, computational MSK modelling can provide reasonable estimates of internal muscle and joint kinetics during functional tasks [216].

This chapter presents an MSK humanoid robot with potential applicability in rotator cuff tendon tissue engineering. The objective of this study is to compare the humanoid robot to human participants and determine whether the humanoid is physiologically relevant from a kinematic and kinetic perspective. A motion study was conducted, comparing abduction/adduction movement in 40 healthy human participants and three joint configurations for the arm-shoulder MSK robot. Estimates of shoulder muscle forces in human participants were obtained using a commercially available MSK modelling software. Forces in the supraspinatus tendon position on the robotic humanoid arm were directly measured.

4.2 Methods

4.2.1 Robotic Shoulder and Joint Configurations

Please refer to Section 3.1 for information on the humanoid robot and joints developed for the study.

4.2.2 Ethics Approval

Please refer to Section 3.2.1 for details on study ethics approval

4.2.3 Study Participants

Please refer to section 3.2.2 for details on participant demographics.

4.2.4 Equipment and Software Details

Please refer to Section 3.2.3 for details about the equipment and software used in this study.

4.2.5 Quality Assurance

Please refer to Section 3.2.4 for quality assurance and to Section 3.2.7 for motion study data processing.

4.2.6 Task Protocol

Please refer to Section 3.2.5 for a detailed task protocol.

4.2.7 Kinematic Model

Please refer to Section 3.2.6 for a description of the kinematic model used in this study.

4.2.8 Human Force Data

Please refer to Section 3.2.8 for a description of the MSK model used to estimate supraspinatus tendon forces. Please refer to Appendix C for discussion of the validity of the MSK model used in this study.

4.2.9 Humanoid Force Data

A load cell was used to estimate forces for the humanoid robot, as detailed in Section 3.2.9.

4.2.10 Data Analysis

Kinematic Comparison

Motion trajectory plots were presented for qualitative comparison of humanoid robot and participant kinematic profiles. Total range of motion and average movement speed were used to evaluate ability to complete movement tasks. Movement quality is important in UE MA and was assessed using peak acceleration, a measure of efficiency during task completion, and the speed metric, a dimensionless ratio of average to peak movement speed (v_{avg}/v_{peak}) [223-227]. A speed metric ratio closer to 1 indicates greater consistency of speed throughout a motion, while a value closer to 0 indicates larger fluctuations in speed consistency throughout a movement [223, 224].

Kinetic Comparison

Kinetic data were presented as force (N) in this study to facilitate comparison between human participants and the humanoid robot. Force trajectory plots were presented for qualitative comparison of humanoid robot and participant kinetic profiles. Average force and peak force were the outcome parameters used to quantitatively compare the kinetic profiles of the humanoid arm and healthy participants.

4.2.11 Statistical Analysis

The D'Agostino-Pearson test was used to verify the normality of outcome parameters [220]. Kinematic outcome parameters were found to be normally distributed for both the humanoid robot and healthy participants. Unpaired *t*-tests were therefore used for quantitative analysis of kinematic data. Force outcome parameters obtained from MSK modelling were normally distributed; several force values obtained from the humanoid robot were not normally distributed. The Mann-Whitney *U* was therefore used for quantitative interpretation of kinetic data.

4.3 Results

These subsections describe the humanoid robot in terms of fidelity to human anatomy, movement characteristics, and kinetic profile during abduction tasks.

4.3.1 Actuator Configuration, Structure and Dimensions of System

To evaluate the robustness of the humanoid robot and improve clinical relevance of the humanoid, two additional configurations were developed for this study: a joint which incorporates a bipolar shoulder implant and a reverse ball and socket joint inspired by reverse shoulder implants [228] (Figure 24). The modified implant was used to evaluate whether the original ball and socket joint adequately imitates a clinical implant. Given that the humanoid robot lacks muscles and ligaments present in human shoulders, the reverse joint was tested in this study as it was expected to match the biomechanics of a functional human shoulder more closely.

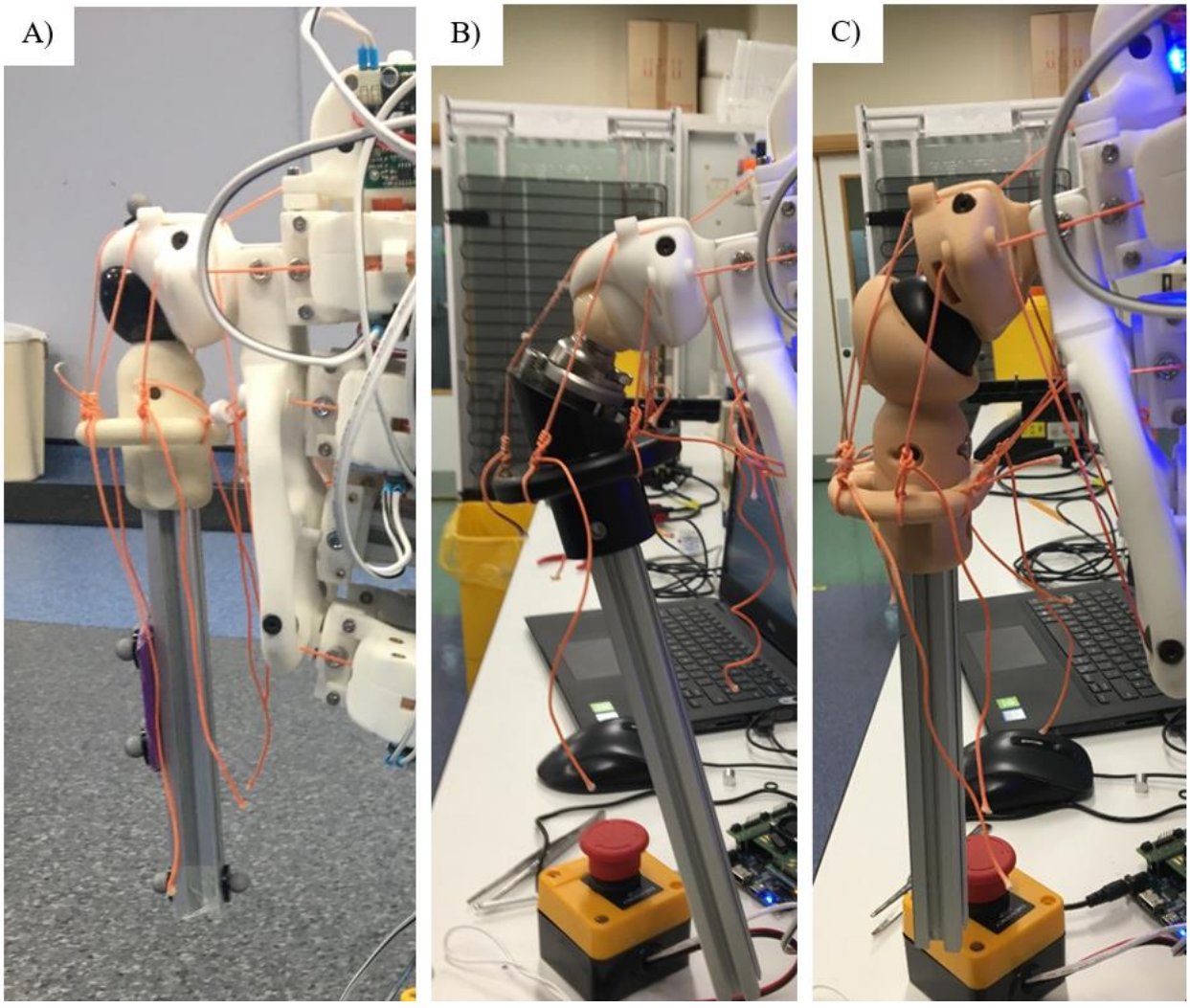


Figure 24: Joint configurations implemented in this study. A) Original ball and socket joint developed with humanoid arm. B) Joint based upon clinical shoulder implant. C) Socket and ball reverse shoulder joint.

While the humanoid arm attempts to provide tendons and a joint that resemble the rotator cuff and GH joint, respectively, the human shoulder is a complex structure consisting of many important anatomic features. Relevant parameters comparing the fidelity of the humanoid arm-shoulder system to the adult human shoulder have been summarised in Table 10.

Table 10: Comparison of the original MSK arm-shoulder robot joint and adult human shoulder anthropometric parameters. Data for the average human were obtained from previously reported anthropometric measurements [212, 229, 230].

Parameter	Humanoid Shoulder	Average Human	Ratio (%)
Upper Trunk* Length (cm)	46.0	41.0	112
Upper Arm$^{\lambda}$ Length (cm)	26.5-32.5	29.7	89-109[#]
Upper Trunk* Mass (kg)	5.2	23.1	23
Upper Arm$^{\lambda}$ Mass (kg)	0.425	2.1	20
Number of Muscles[†]	9	15 +	60
Number of Joints	1	4	25
Degrees of Freedom	3	12	25

* The region from the C7 vertebrae to the T12 vertebrae was defined as the upper trunk region.
$^{\lambda}$ The upper arm was defined as the region spanning the length of the humerus (i.e. humeral head to the epicondyles)
The original ball and socket and reverse joint configurations are 26.5 cm. The clinical implant configuration is 32.5 cm long.
† The muscles contributing to human shoulder motion include the supraspinatus, infraspinatus, teres minor, subscapularis, deltoid, teres major muscles, serratus anterior, pectoralis minor, levator scapulae, rhomboid major, rhomboid minor, trapezius, latissimus dorsi, biceps brachii, and triceps brachii

The humanoid arm reasonably imitates the length of the average adult trunk and upper arm segments but differs significantly from other anthropometric parameters described in Table 10.

4.3.2 Kinematic Profile

Trajectory plots comparing the completion of the slow, controlled tasks in human participants and the humanoid robot have been provided in Figure 25. Qualitatively, the humanoid robot very closely matches the trajectory of human participants in both movement tasks. The mean trajectory of the humanoid robot is essentially indistinguishable from that of the human participants in the 30^{o} abduction/adduction task. It is important to note that there is significant variability in the SD of motion data 30^{o} trial, however. The

peak ROM attained by the humanoid robot with the ball and socket joint configuration appears to be lower than the peak ROM of the healthy human participants in the 90º abduction/adduction trial.

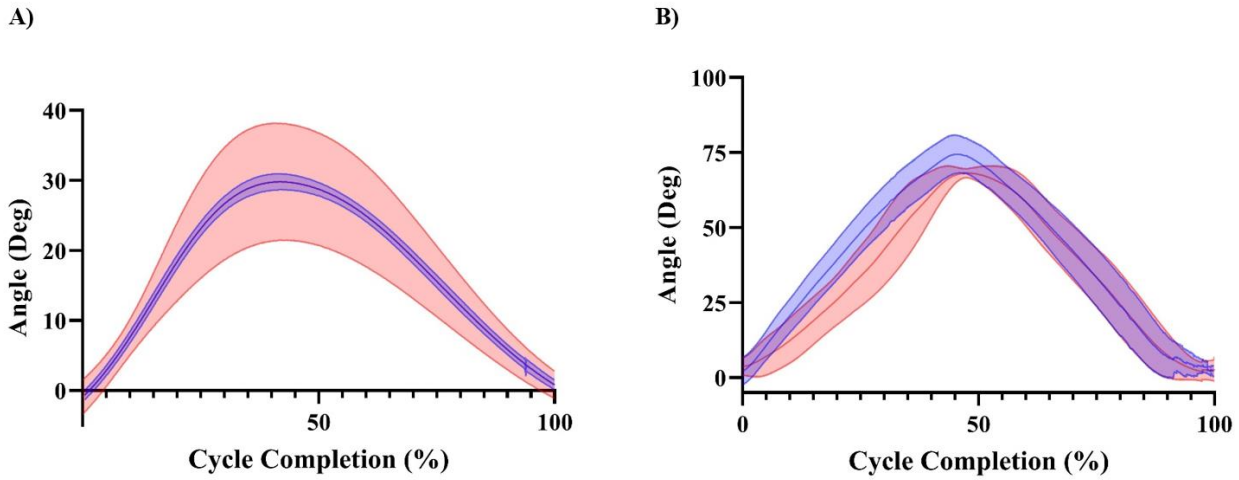


Figure 25: Kinematic trajectory plots for the slow movement tasks using the original ball and socket joint configuration. A) Compares the humanoid arm to human participants for the 30º abduction task. The cycle length of time for this task was 6 s. B) Compares the humanoid arm to human participants for the 90º abduction task. The cycle length of time for this task was 18 s. The blue curve and error bands represent mean human participant movement ± 1 SD in both plots. The red curve and error bands represent mean angle ± 1 SD for the humanoid robot in both plots.

The quantitative metrics provided in Tables 11 and 12 similarly indicate that the kinematic profile of human participants is closely matched by the humanoid robot. For the 30º abduction/adduction task, only the robotic system's average and peak acceleration were found to have a statistically significant difference compared to human participants. Average and peak accelerations of the humanoid arm were both found to be lower than the values obtained for human participants by 3.7 (SEM 1.4) deg/s^2 and 23.1 (SEM 2.6) deg/s^2, respectively. While the humanoid arm matched the speed of human participants in the 90º task, it was unable to achieve the same total ROM. A difference of 9.4º (SEM 3.1º) was noted for the 90º task. Average and peak accelerations of the humanoid robot were found to be lower than those of human participants by 1.8 (SEM 0.7) deg/s^2 and 15.8 (SEM 3.1) deg/s^2, respectively for the 90º task.

Table 11: Kinematic outcome variables from slow movement 30º abduction/adduction task. P-values indicating that a parameter of interest differs significantly from human participants (i.e. p<0.05) have been bolded.

Parameter	Human	Humanoid Robot		
	Mean (SD)	Mean (SD)	p-value	Difference (SEM)
Total ROM (deg)	30.3 (7.0)	30.7 (0.4)	0.702	0.4 (1.1)
Average Speed (deg/s)	9.7 (2.3)	8.6 (0.3)	0.297	1.1 (1.0)
Peak Speed (deg/s)	16.1 (5.4)	16.1 (0.8)	0.976	0.0 (0.9)
Speed Metric	0.61 (0.1)	0.53 (0.1)	0.190	0.1 (0.1)
Average Acceleration (deg/s^2)	9.0 (3.2)	5.4 (0.5)	**0.0145**	3.7 (1.4)
Peak Acceleration (deg/s^2)	36.0 (16.0)	12.9 (1.1)	**<0.0001**	23.1 (2.6)

Table 12: Kinematic outcome variables from slow movement 90º abduction/adduction task. P-values indicating that a parameter of interest differs significantly from human participants (i.e. p<0.05) have been bolded.

Parameter	Human	Humanoid Robot		
	Mean (SD)	Mean (SD)	p-value	Difference (SEM)
Total ROM (deg)	78.1 (6.6)	68.7 (4.3)	**0.0042**	9.4 (3.1)
Average Speed (deg/s)	7.9 (0.9)	7.5 (0.3)	0.363	0.4 (0.4)
Peak Speed (deg/s)	16.4 (5.3)	13.5 (2.4)	0.246	2.8 (2.4)
Speed Metric	0.52 (0.1)	0.57 (0.1)	0.346	0.1 (0.1)
Average Acceleration (deg/s^2)	5.7 (1.5)	3.9 (0.7)	**0.011**	1.8 (0.7)
Peak Acceleration (deg/s^2)	33.0 (17.14)	17.2 (2.9)	**<0.0001**	15.8 (3.1)

Trajectories for the humanoid robot and human participants completing abduction/adduction tasks at a faster speed have been provided in Figure 26 and Figure 27. While the movement pattern for both the robotic arm and human participants appear to be similar in both tasks at the faster speed, there are several differences worth noting when assessing the performance of each joint. In both movement tasks, the humanoid robot's peak ROM is significantly lower than the target peak abduction ROM (30º and 90º, respectively) with the ball and socket joint and clinical implant joint configurations. In contrast, the peak range of motion for the reverse shoulder joint appears to resemble the target peak ROM more closely in both tasks. In general, the humanoid robot reached its highest ROM before the 50 % cycle completion

point, regardless of joint configuration, whereas human participants were able to consistently time their movements to attain peak abduction range at the midpoint.

From the slope of the curves in the trajectory plots, the clinical implant joint closely matched or exceeded the speed of human participants until reaching their peak abduction range. Conversely, it can be noted that the adduction phase of the movement trial is completed at a slower speed for this joint. Compared to human participants, the ball and socket joint moved at a consistent albeit slow speed throughout its trajectory for each task. Qualitatively, the reverse shoulder joint configuration most closely matches human speed and consistency in both tasks.

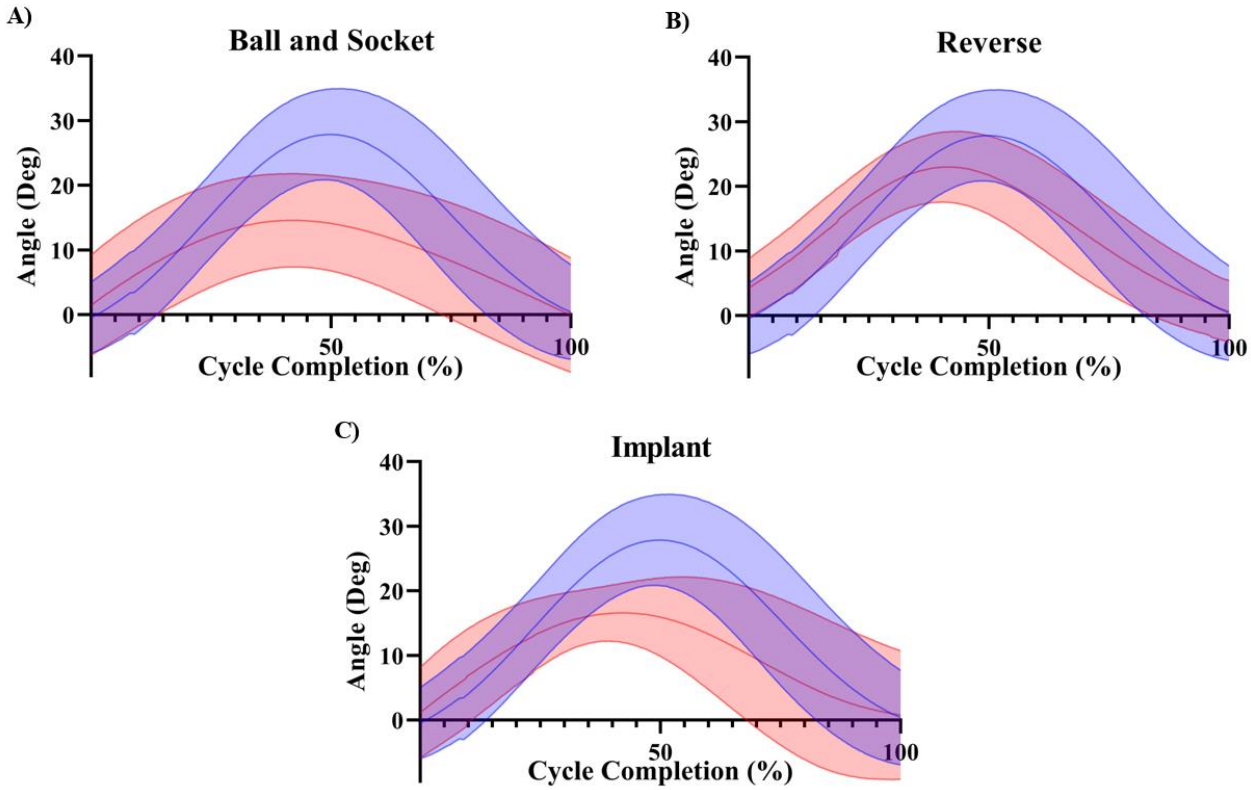


Figure 26: Kinematic trajectory plots for abduction to 30° in scapular plane, measured in degrees. A) Compares the original ball and socket joint configuration's trajectory; B) compares the reverse shoulder joint configuration; and C) compares the clinical implant joint configuration. Blue curve and error bands represent mean human participant movement ± 1 SD. Red curve and error bands represent mean angle ± 1 SD for each joint configuration. The movement cycle length is 2 seconds.

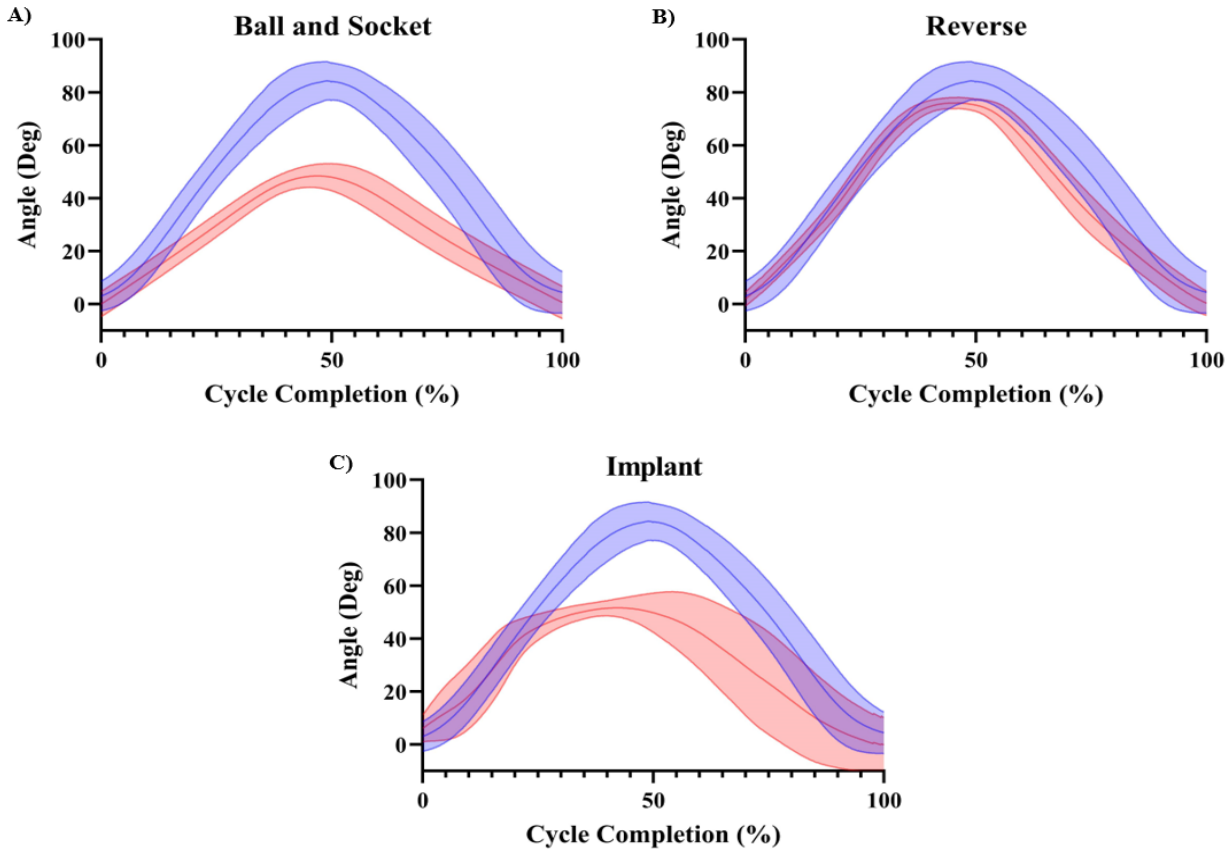


Figure 27: Kinematic trajectory plots for abduction to 90º in scapular plane, measured in degrees. A) Compares the original ball and socket joint configuration's trajectory; B) compares the reverse shoulder joint configuration; and C) compares the clinical implant joint configuration. Blue curve and error bands represent mean human participant movement ± 1 SD. Red curve and error bands represent mean angle ± 1 SD for each joint configuration. The movement cycle length is 6 seconds.

Tables 13 and 14 provide a summary of kinematic outcome parameters used to quantitatively evaluate the performance of the humanoid robot with different joint configurations. Consistent with the trajectory plots, the ball and socket and clinical implant joints had peak ROMs which were around 10º and 30º lower than the target ROM achieved by human participants for the 30º and 90º abduction tasks, respectively. The humanoid robot attained higher ROMs with the reverse shoulder joint; total ROM was within 10º of human participants for both tasks.

The average movement speeds of the ball and socket and clinical implants were significantly lower than the human participants for both tasks. Differences of 20.0 (SEM 1.3) deg/s for the ball and socket and 15.8 (SEM 1.2) deg/s for the and clinical implant were noted in the 30º abduction trial, while the differences for the 90º trial were 13.4 (SEM 0.7) deg/s and 9.9 (SEM 1.0) deg/s, respectively. The mean

peak movement speeds for the ball and socket joint were less than half the mean peak movement speeds for human participants in both trials. The reverse shoulder joint more closely matched average movement speed of healthy human participants, with no statistically significant difference in average movement speed for the 90º task and an 8.5º (SD 1.3)º difference reported for the 30º task.

There was no statistically significant difference in the speed metric of the reverse shoulder joint and human participants for both tasks. Both trials completed with the implant joint reported lower average speed metrics than human participants. The ball and socket joint had a lower speed metric for the 30º task and a higher speed metric value for the 90º task when compared to human participants.

Human participants had a greater mean peak acceleration than the humanoid robot for all joint configurations in the 30º task. In the 90º task, the reverse shoulder's peak acceleration did not differ significantly from human participants. The clinical implant's peak acceleration was 97.0 (SEM 24.3) deg/s^2 greater than human participants and the ball and socket joint's peak acceleration was 80.3 (SEM 12.4) deg/s^2 less than human participants for the 90º task.

Table 13: Kinematic outcome variables from 30º abduction/adduction task used to evaluate implant performance. P-values indicating that a parameter of interest differs significantly from human participants (i.e. $p<0.05$) have been indicated in bolded text.

Parameter	Human	Ball and Socket			Clinical Implant			Reverse		
	Mean (SD)	Mean (SD)	p-value	Difference (SEM)	Mean (SD)	p-value	Difference (SEM)	Mean (SD)	p-value	Difference (SEM)
Total ROM	32.5 (6.9)	16.0 (6.6)	**<0.0001**	16.5 (1.7)	21.7 (2.2)	**<0.0001**	10.8 (1.2)	24.2 (3.4)	**0.0016**	8.3 (1.3)
Average Speed (deg/s)	29.7 (6.9)	9.7 (3.2)	**<0.0001**	20.0 (1.3)	14.0 (2.5)	**<0.0001**	15.8 (1.2)	21.2 (2.8)	**<0.0001**	8.5 (1.3)
Peak Speed (deg/s)	49.7 (14.5)	19.0 (3.8)	**<0.0001**	30.7 (2.5)	30.1 (8.1)	**<0.0001**	19.6 (3.5)	34.6 (4.2)	**<0.0001**	15.1 (2.5)
Speed Metric	0.60 (0.11)	0.51 (0.17)	**0.016**	0.09 (0.03)	0.48 (0.1)	**0.0002**	0.11 (0.03)	0.63 (0.12)	0.352	0.03 (0.03)
Average Acceleration (deg/s^2)	73.7 (31.0)	12.0 (2.5)	**<0.0001**	61.7 (5.0)	29.4 (10.6)	**<0.0001**	44.3 (5.5)	41.5 (9.3)	**<0.0001**	32.2 (5.4)
Peak Acceleration (deg/s^2)	173.3 (76.2)	27.0 (7.5)	**<0.0001**	146.2 (12.3)	57.8 (20.7)	**<0.0001**	115.4 (17.4)	108.1 (34.1)	**<0.0001**	65.1 (14.4)

Table 14: Kinematic outcome variables from 90º abduction/adduction task used to evaluate implant performance. P-values indicating that a parameter of interest differs significantly from human participants (i.e. p<0.05) have been indicated in bolded text.

Parameter	Human	Ball and Socket			Clinical Implant			Reverse		
	Mean (SD)	Mean (SD)	p-value	Difference (SEM)	Mean (SD)	p-value	Difference (SEM)	Mean (SD)	p-value	Difference (SEM)
Total ROM	82.6 (8.6)	50.9 (3.1)	**<0.0001**	31.7 (2.0)	54.1 (7.5)	**<0.0001**	28.5 (2.2)	77.0 (2.1)	**0.0062**	5.6 (2.0)
Average Speed (deg/s)	26.6 (4.4)	13.2 (0.7)	**<0.0001**	13.4 (0.7)	16.7 (2.1)	**<0.0001**	9.9 (1.0)	25.1 (0.7)	0.130	1.5 (1.0)
Peak Speed (deg/s)	41.2 (6.7)	17.6 (1.3)	**<0.0001**	24.1 (1.5)	65.4 (16.9)	**<0.0001**	23.8 (3.9)	45.8 (18.8)	0.195	4.2 (3.2)
Speed Metric	0.62 (0.14)	0.75 (0.05)	**<0.0001**	0.13 (0.02)	0.28 (0.10)	**<0.0001**	0.34 (0.04)	0.58 (0.10)	0.300	0.04 (0.04)
Average Acceleration (deg/s^2)	25.8 (6.4)	5.6 (0.8)	**<0.0001**	20.2 (1.5)	30.3 (10.1)	0.080	4.5 (2.5)	24.8 (22.1)	0.846	1.0 (5.0)
Peak Acceleration (deg/s^2)	102.8 (55.0)	22.5 (4.6)	**<0.0001**	80.3 (12.4)	199.8 (29.4)	**0.0002**	97.0 (24.3)	80.7 (20.0)	0.096	22.1 (13.1)

4.3.3 Comparison of Kinetic Profiles

Plots describing supraspinatus forces throughout the movement cycle for the 30º and 90º abduction tasks completed at the faster speed have been provided in Figure 28 and Figure 29, respectively. Kinetic trials were not completed for the slow, controlled movement. In the 30º abduction task, human participants reach their maximum muscle force around the midpoint of the cycle. The humanoid robot follows this same trajectory with the ball and socket joint configuration. Conversely, with the implant and reverse shoulder joint configurations, the humanoid shoulder appears to reach peak muscle[§] force levels approximately 25 % through the task cycle in the 30º task.

In the 90º abduction task, peak force values can be appreciated at 25 % and 75 % through the movement cycle for human participants. This trend is similarly mirrored by the clinical implant and reverse shoulder joint configurations, whereas peak muscle forces are observed at the midpoint of the cycle for the original joint during the 90º task. The force magnitudes for human participants in the 30º abduction task appear to

[§] For the humanoid arm, 'muscle' and 'myorobotic actuator' are used interchangeably to describe the component responsible for generating force to move and control the robotic arm-shoulder system in the supraspinatus position.

be well-matched by the implant and ball and socket joint configurations. The reverse shoulder appears to generate significantly higher supraspinatus muscle forces throughout the movement cycle.

In the 90° task, a sharp spike in force magnitude is noted in the first quarter of the cycle for the implant joint configuration. Negligible force output readings can be noted around the midpoint of the cycle for this joint, with a small increase in force readings towards the end of the cycle. The reverse shoulder configuration exhibited significantly higher forces than human participants throughout the majority of the cycle for the 90° task, with an abrupt decrease in force values being noted around the middle of the cycle. The original ball and socket joint more closely matches the force magnitude of human participants for this task compared to the other joint configurations.

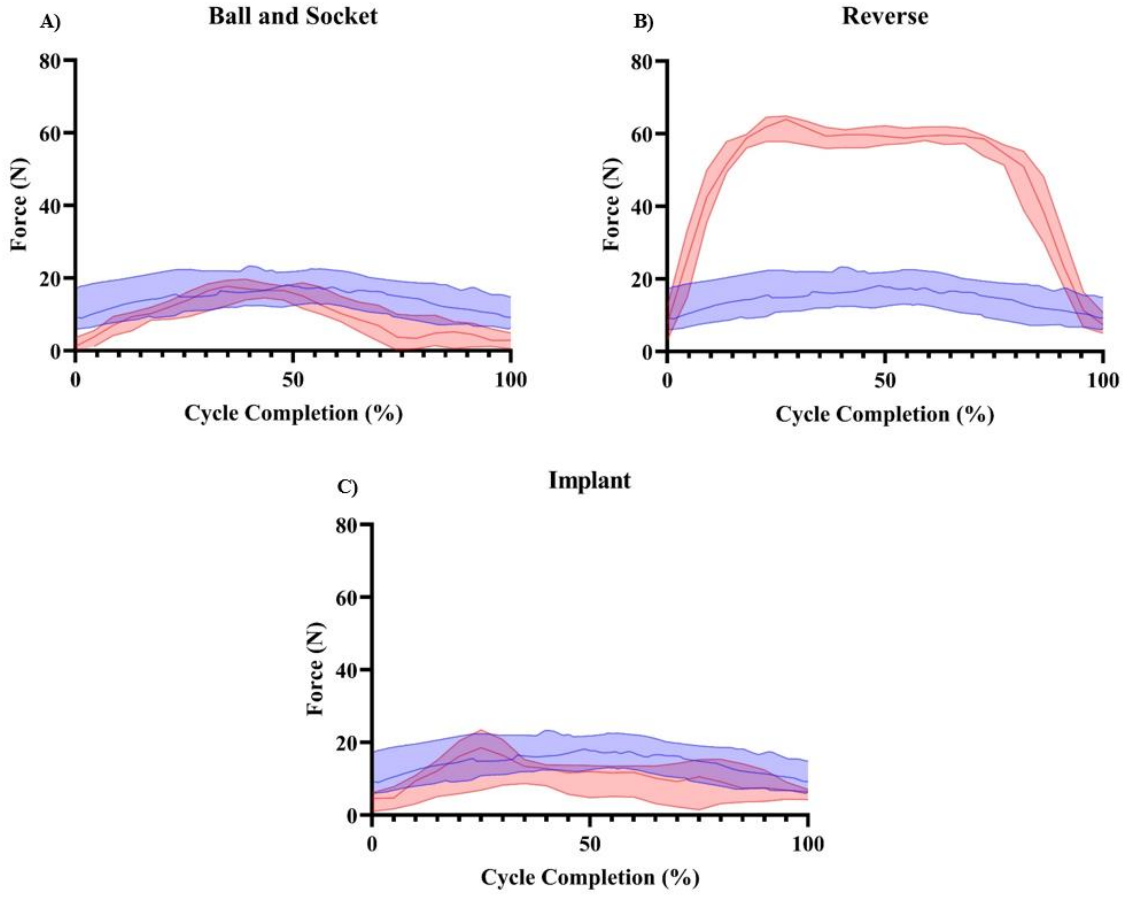


Figure 28: Supraspinatus force profile for abduction to 30° in scapular plane, measured in Newtons (N). A) Compares the original ball and socket joint configuration's force profile; B) Compares the reverse shoulder joint configuration's force profile. and C) compares the clinical implant joint configuration. The blue curve and error bands represent median human participant force and IQR, respectively. The red curve and error bands represent median force and IQR, respectively, for each joint configuration. The movement cycle length is 2 seconds.

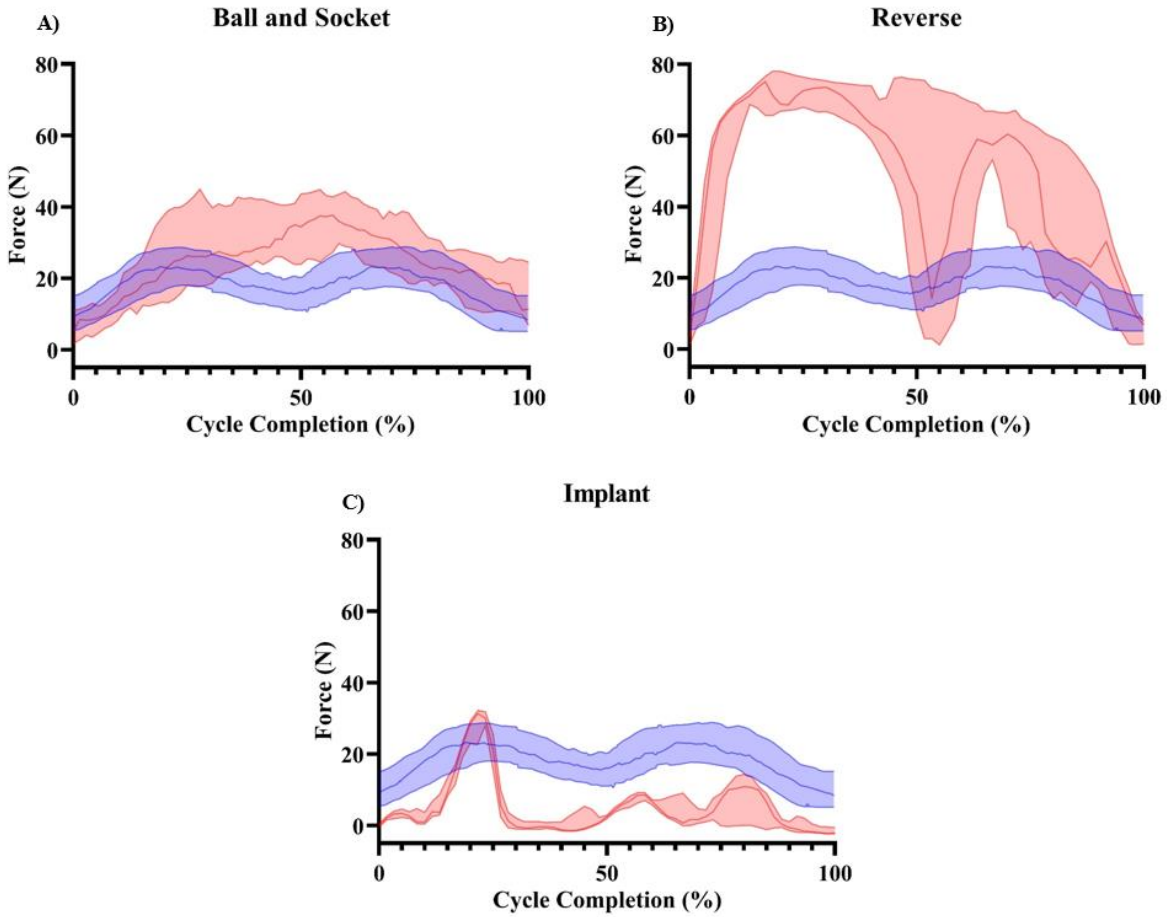


Figure 29: Supraspinatus force profile for abduction to 30º in scapular plane, measured in Newtons (N). A) Compares the original ball and socket joint configuration's force profile; B) Compares the reverse shoulder joint configuration's force profile. and C) Compares the clinical implant joint configuration. The blue curve and error bands represent median human participant force and IQR, respectively. The red curve and error bands represent median force and IQR, respectively, for each joint configuration. The movement cycle length is 6 seconds.

Figure 30 and Table 15 further describe force magnitude for each joint configuration compared to human participants during the 30º abduction trial. Peak force values for the ball and socket and implant joints were found to have no statistically significant difference from the peak force experienced by human participants during this task. With the ball and socket and implant joint configurations, the humanoid robot had modestly smaller average force values compared to human participants; average forces differed by less than 10 N for these joint configurations. The average muscle force for the reverse shoulder configuration was measured to be twice as large as the average force estimated for human participants,

while the peak force recorded over the movement cycle for this joint was three times greater than the peak muscle force estimated for human participants during task completion.

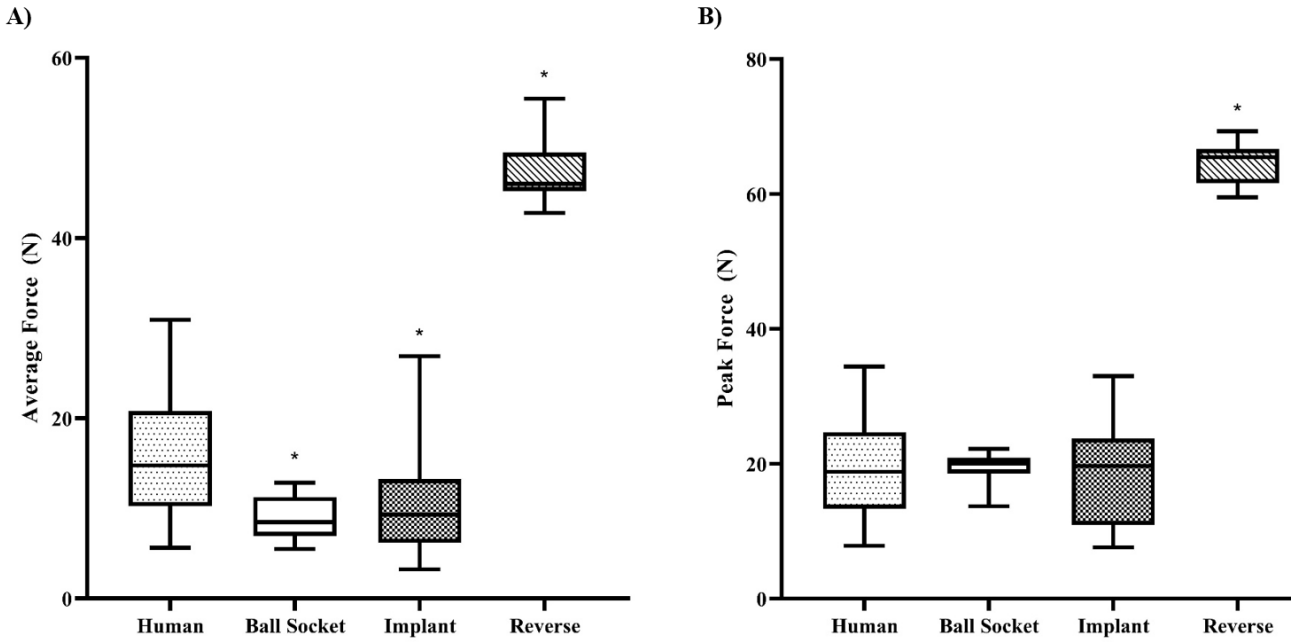


Figure 30: Supraspinatus force values from abduction to 30º task completed over 2 s. A). Average force values for the human participants and the humanoid robot for each joint configuration during task completion. B). Peak force values for human participants and the humanoid robot for each joint configuration during task completion. Results which have statistically significant ($p<0.05$) differences from human participants have been denoted with an asterisk (*).

Table 15: Kinetic outcome variables from 30º abduction/adduction task used to evaluate implant performance. P-values indicating that parameter of interest differs significantly from human participants (i.e. $p<0.05$) are bolded.

Parameter	Human	Ball and Socket			Implant			Reverse		
	Median (IQR)	Median (IQR)	p-value	Difference	Median (IQR)	p-value	Difference	Median (IQR)	p-value	Difference
Average Force (N)	14.8 (10.2-20.8)	8.0 (8.5-11.3)	**<0.0001**	6.8	9.3 (6.2-13.2)	**0.0056**	5.5	46.0 (45.2-49.5)	**<0.0001**	31.3
Peak Force (N)	18.8 (13.4-24.7)	20.0 (18.6-20.9)	0.671	1.2	19.7 (10.9-23.8)	0.651	0.8	65.5 (61.6-66.7)	**<0.0001**	46.6

Figure 31 and Table 16 further describe force magnitudes for the 90º abduction task. Statistically significant differences in average and peak forces were observed between human participants and the humanoid robot with all three joint configurations. Peak force values with all joint configurations were higher than the peak force of human participants during task completion. The clinical implant most closely matched the peak force of human participants, with a difference of less than 10 N. The ball and

socket joint had a 23.4 N higher median peak force compared to human participants, while the reverse shoulder joint exceeded the median peak force of human participants by 51.8 N. The average force of human participants in the 90° abduction task was 12.1 N greater than the clinical implant joint configuration and 12.0 N less than the original ball and socket configuration. The reverse configuration's median average force was 23.3 N greater than the median force in human participants.

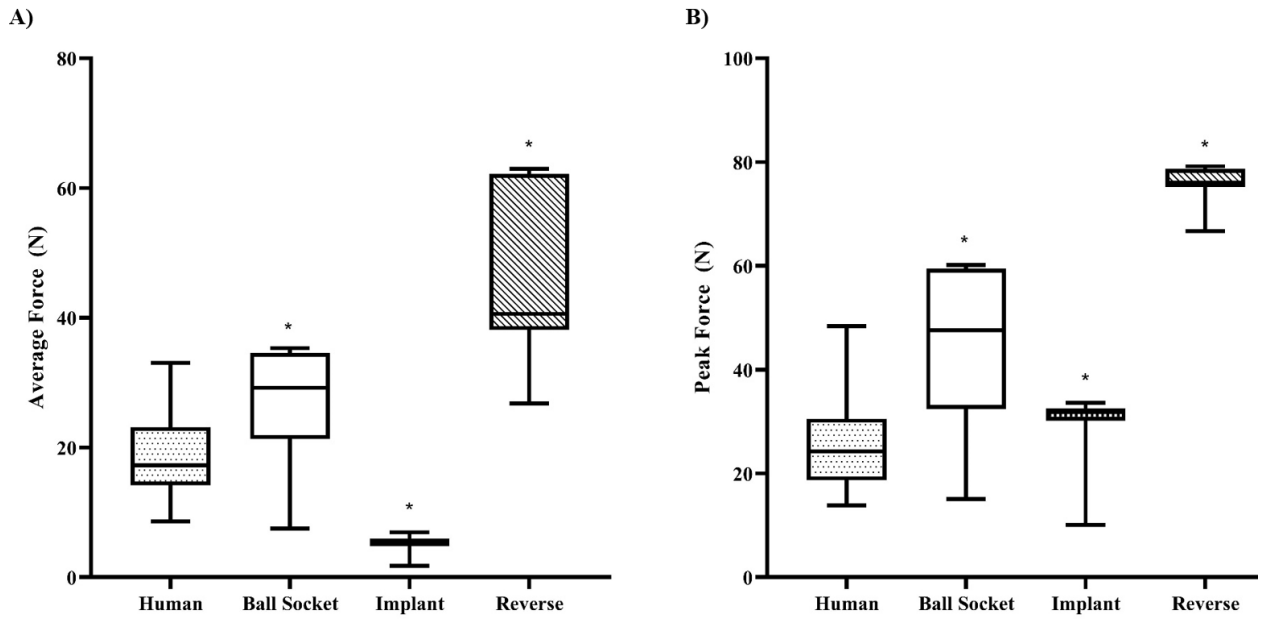


Figure 31: Supraspinatus force values from abduction to 90º task completed over 6 s. A). Average force values for the human participants and the humanoid robot for each joint configuration during task completion. B). Peak force values for human participants and the humanoid robot for each joint configuration during task completion. Results which have statistically significant ($p<0.05$) values from human participants have been denoted with an asterisk (*).

Table 16: Kinetic outcome variables from 90º abduction/adduction task used to evaluate implant performance. P-values indicating that parameter of interest differs significantly from human participants (i.e. $p<0.05$) are bolded.

Parameter	Human	Ball and Socket			Implant			Reverse		
	Median (IQR)	Median (IQR)	p-value	Difference	Median (IQR)	p-value	Difference	Median (IQR)	p-value	Difference
Average Force (N)	17.3 (14.2-23.2)	29.2 (21.3-34.6)	**0.0016**	12.0	5.2 (4.8-6.0)	**<0.0001**	12.1	40.6 (38.1-62.2)	**<0.0001**	23.3
Peak Force (N)	24.2 (18.7-30.5)	47.6 (32.5-59.5)	**<0.0001**	23.4	31.8 (30.2-32.5)	**0.018**	7.6	76.0 (75.2-78.7)	**<0.0001**	51.8

4.4 Discussion

4.4.1 Interpretation of Key Findings

In this study, human participants representing normal shoulder function were typically from a young adult demographic, whereas typical randomised control trials often recruit middle aged patients to represent the average adult. Since the purpose of this pilot study was to evaluate the feasibility of a robotic model in comparison to healthy human shoulders, it was reasonable to use younger participants, given that prevalence of rotator cuff injury tends to increase with age [2, 45, 46].

Apart from trunk and upper arm length, the humanoid robot presented in this study does not faithfully replicate healthy human shoulder anatomy. Human shoulders have four articulating joints, stabilised by numerous ligaments, and controlled by more than fifteen muscles [230, 231]. Muscles originating from numerous structures contribute to shoulder movement and stability, including the anterior chest wall, spinous processes of the back, clavicle, and scapula. Conversely, the humanoid shoulder only has one joint, approximating the GH joint, and is controlled and stabilised by seven myorobotic actuators in analogous positions to the rotator cuff muscles.

Despite significant anatomic differences, the humanoid robot closely matched the kinematics of human participants for the abduction to 30^{o} task completed at a slower pace. The only notable difference between the humanoid robot and human participants was the mean peak acceleration value. This discrepancy is not discouraging however, as this trial aimed to produce abduction patterns that resemble the slow movement tasks used in the initial phases of supraspinatus tendon rehabilitation. This phase of rehabilitation is not focussed on rebuilding significant amounts of tendon tissue, but instead on providing small mechanical cues to guide tendon cell alignment. It is not necessary to provide significant accelerations or forces to achieve this goal. Consequently, these results suggest that the humanoid robot adequately replicates human kinematics for slow abduction tasks up to 30^{o} ROM.

While a similar movement profile was observed during the slower 90º abduction task, a statistically significant difference in peak ROM exists between the humanoid and human participants. The humanoid robot was unable to exceed an average ROM of 68.7º (SD.4.3º) due to the ball element being constrained by the socket element of the joint. It is unsurprising that the ball and socket's movement is constrained to around 70º ROM, given that the humanoid robot lacks crucial anatomic structures found in human shoulders, such as the scapula. For abduction between 30º-90º, it has been estimated that the scapula contributes 20-40 % (12º-24º) of the total ROM in healthy human shoulders [232]. This task demonstrated that the humanoid robot could not adequately match human abduction to 90º with the original ball and socket joint.

The abduction to 30º and 90º tasks were subsequently completed at a faster pace (over 2 s and 6 s intervals, respectively, or at a target pace of 30 deg/s) with two additional joints: a joint which incorporated a clinically used total shoulder implant and a reverse ball and socket joint, inspired by reverse shoulder implants. The purpose of these trials was to characterise abduction movements of the humanoid robot at a more physiologically relevant pace and to evaluate the performance of the humanoid using different joint configurations.

Although the original ball and socket joint closely matched human movement at the slower pace, this configuration inadequately reproduced human kinematics with more rapid movement. The clinical implant was similarly unable to replicate human performance of these tasks over the specified quicker time interval. The clinical implant's speed metric, or measure of smoothness, was found to be significantly lower than that of human participants in both trials. This finding suggests that the implant not only completed the movements at a slower pace and to a lower peak ROM than human participants, but also moved less fluidly throughout the trajectory. This was observed qualitatively in Figures 27 and 28, with the implant quickly reaching peak ROM but having difficulty in changing directions and transitioning from abduction to adduction to return to the starting point.

The reverse shoulder joint's kinematic profile was close match to that of the human participants during task completion at a faster pace. Differences in peak ROM were small, with differences of less than 10^{o} being observed for both movement trials. The trajectory profiles of the reverse shoulder were also more qualitatively consistent with those of human participants. In the 90^{o} abduction trial, peak ROM was the only outcome parameter found to have a statistically significant difference when compared with human completion of this task. The increased ROM and superior kinematic profile of the reverse shoulder configuration were promising findings, given that reverse implants are used clinically to improve stability and function for patients with shoulder muscle deficiencies [233].

Differences in movement speeds and force profiles can likely be attributed to joint stability. The original joint and the clinical implant were more unstable than the reverse shoulder joint, leading to greater recruitment of the myorobotic actuators in the infraspinatus, subscapularis, and teres minor positions. The need for the robot to coordinate between these actuators slowed down movement speed, thereby preventing the humanoid from mimicking human kinematics with these joint configurations. Interestingly, this increased coordination also had the unintended effect of limiting force contributions from the supraspinatus position actuator.

Consequently, a close match in force magnitudes was noted in the 30^{o} abduction trial, with no statistically significant differences in peak force and less than a 10 N difference in average force between human participants and the original ball and socket or clinical implant joint configurations. Average force magnitudes were also reasonably well matched in the 90^{o} abduction trial for these two joint configurations. The reverse shoulder joint configuration consistently exhibited significantly higher mean and peak force values compared to human participants during task completion, given that force contributions from the supraspinatus actuator were not limited with this joint configuration.

These results suggest that the humanoid robot can either reproduce human kinematics or provide physiologically relevant forces during task completion, but not both simultaneously. In future

experimental work, it is clear that adaptations will need to be made to the humanoid arm to ensure stability and an appropriate range of forces without sacrificing movement speed and ROM. This may be achieved through placement of artificial ligaments around the joint to increase stability, incorporation of a scapula in the model, or incorporation of additional actuators in physiologically relevant arrangements.

4.4.2 Implications of Key Findings

Tissue Engineering

While benchtop science models can have limitations in application to clinical medicine, such as patient reported outcome measures research suggesting that the degree of tendon injury does not always match severity of symptoms [234], tendon tissue engineering serves many purposes, such as better understanding biomolecules involved in tendon repair and injury, the ability to compare different loading programmes to influence rehabilitation protocol, and eventually, production of tissue grafts for clinical use. To extract the most physiologically relevant data possible from these studies, having a system that reasonably imitates human anatomy is crucial.

To date, no bioreactor systems presented in peer-reviewed literature have attempted to provide mechanical stimulation through movement patterns that consider the anatomic location of the tendon tissue being cultured [12, 115-136]. Furthermore, a number of current studies have presented bioreactor systems which provide less than 5 N of force during peak loading [115, 124, 129, 131]. It can therefore be concluded that although the humanoid arm presented in this study lacks many of the complex structures present in the human shoulder, this platform has superior biomimicry to the uniaxial and biaxial tensile stage bioreactors currently being used to produce engineered tendon. With actuators positioned to simulate rotator cuff muscles and tendons, this system demonstrated the potential to replicate controlled abduction tasks at a low ROM. This is relevant to shoulder tendon tissue engineering, given that the supraspinatus tendon, which is most commonly injured, is primarily responsible for this movement [41].

It is important to provide tendon tissue with the right amount of tensile loading and appropriate mechanical cues; insufficient stimulation has been shown to lead to catabolic gene expression and eventual loss of structural integrity [16, 29], while excess loading of tendon tissue leads to inflammation, degradative enzyme production, undesirable fibroblast differentiation and programmed cellular death [51]. Although further work will be required to characterise loading patterns in healthy shoulders, the results from this study suggest that the humanoid robot would be capable of providing physiologically relevant mechanical loading to tissue constructs. While the movement pattern and mechanical loading in this study focussed on the supraspinatus tendon, the humanoid bioreactor system approach could be applied to other MSK tissues within the body, facilitating development of tissue grafts in consideration of other anatomic locations.

Other Biomedical Applications

In this study, it was possible to identify distinct differences in the performance of each joint configuration tested with the humanoid robot. This ability to discern differences in joint performance may allow MSK humanoid robots to play a role in clinical implant and biomedical device development. Currently, shoulder implants undergo biomechanical evaluation using uniaxial and biaxial loading systems which do not directly imitate *in vivo* loading conditions [235, 236]. By offering more mechanically appropriate loading conditions, this MSK robot has potential to complement traditional methods of implant testing.

Robotics

This investigation has helped to identify limitations of the current MSK robotic arm. To increase ROM and enhance the performance of this system, future prototypes of the robotic shoulder should incorporate a scapular component. This is already being developed in other MSK robots [237]. As more actuators are incorporated into the system, it will be important for them to be arranged to represent analogous muscles which help contribute to shoulder stability and ROM.

4.4.3 Limitations of Study

Kinematic Modelling

Several limitations exist with the kinematic model used in this study. Despite being widely used commercially, the upper body PiG model has not been rigorously validated and no peer-reviewed studies examining model repeatability have been published.

Scapular contributions have been described as "almost impossible to track noninvasively" due to the large amount of movement under the skin [168, 170]. To reduce error in estimation of joint angles shoulder kinematics were approximated to the GH joint for human participants in this study. If intra-cortical bone pins had been used for marker tracking in this study, it may have been able to differentiate human participants' scapular and GH contributions in abduction tasks. This information could then be used to help inform further development for future prototypes of the humanoid arm presented in this study.

MSK Model and Quantitative Force Estimates

A major appeal of musculoskeletal modelling is the ability to estimate *in vivo* internal muscle forces that cannot be measured using current techniques. This poses a challenge for model evaluation, as it is not possible to directly confirm the validity of model outputs. EMG is a commonly used tool for qualitatively validating results obtained from MSK modelling [216]. This method involves measuring muscle activity and comparing trends from the muscle activity curves to force profiles during task completion.

There are disadvantages to EMG as a validation method, however. The accuracy of force magnitudes cannot be easily confirmed using EMG, given them complex relationship between EMG signal amplitude and force quantity. Furthermore, EMG signals are subject to significant crosstalk, and it would be difficult or impossible to estimate activity of all key shoulder muscles during abduction tasks. Finally, since the supraspinatus tendon lies beneath the deltoid, intramuscular insertion of needle electrodes would be required to obtain accurate supraspinatus activity estimates [238, 239]. Given the invasiveness of this procedure and limitations associated with this method, it was decided to not obtain EMG signals from participants to evaluate the force estimates of this pilot study.

Given that human supraspinatus muscle forces could not be directly measured and EMG activity curves were not obtained for qualitative interpretation, the only method used to evaluate forces presented in this study was comparison with results reported in previous literature examining abduction-related tasks (discussed further in Appendix C). Although estimated supraspinatus muscle forces reasonably matched previously published values from *in vitro* studies using cadaveric shoulder tissue [240, 241] and *in silico* models [242-245], these results must be interpreted cautiously.

While this study focussed on the supraspinatus tendon, the shoulder girdle is a complex structure, and all rotator cuff muscles work in concert to provide stability to the glenohumeral joint and effectuate movement. The kinetic modelling presented in this study is intended to provide a starting point for comparison of human forces with those of the humanoid robot and more complex models are required prior to clinical translation of the information provided in this study [36-39].

4.5 Chapter Summary

This chapter has presented an MSK humanoid robotic arm as a platform for supraspinatus tendon tissue engineering. A motion study was conducted to assess whether the robotic arm was capable of producing physiologically relevant movement patterns and force magnitudes when completing abduction tasks. Kinematic results from this study demonstrate that the humanoid robot can accurately replicate slow, controlled abduction movements up to 30^{o} ROM. Although further work will be required to accurately estimate supraspinatus muscle forces in humans during abduction tasks, the results from this study demonstrate that the humanoid robot would be capable of providing physiologically relevant mechanical loading to tissue constructs. In addition to the potential benefit of advancing tissue engineering and enabling production of tendon grafts for clinical use, this study has identified a potential role of MSK robots in biomedical device testing and highlighted areas of improvement for developing enhanced UE MSK robots. Future work will need to focus on improving the humanoid robot's actuation to enable robust force modulation, operation across a variety movement speeds, and enhanced ROM.

5. Strain Characterisation in Tendon Tissue Engineering Scaffold

5.1 Introduction

Rotator cuff tendon injuries are a frequent musculoskeletal (MSK) condition for which patients seek medical attention. These injuries also present a significant socio-economic burden, with workers taking significant amounts of sick leave to recover following surgery and reporting lower productivity upon return to work [5]. Despite surgical advances, patient outcomes remain poor, with upwards of 40 % of tendon repairs failing post-operatively [7-10]. Revision surgeries further compound the social and economic impacts of rotator cuff tendon disease.

Engineering autografts for tendon replacement has been proposed as a solution to this growing challenge. This process involves culturing patient cells on scaffold material in a controlled bioreactor system. A widely held belief within the field of tendon tissue engineering is that bioreactors should mimic the physiologic environment of native tissue during *in vitro* culture [12]. In addition to appropriate chemical conditions, tendon tissue requires mechanical cues for tissue maintenance, development, and healing [17]. A growing body of evidence demonstrates that tendon tissue deforms non-uniformly during *in vivo* loading and responds differently to mechanical stimuli depending on the direction and type of loading applied [27, 30-32]. Most current bioreactor systems have limited ability to mimic the native environment of tendon, as they only provide uniaxial loading with a linear actuator [12].

To better replicate the mechanical environment of native rotator cuff tendon tissue, our research group has developed an MSK humanoid shoulder for tendon tissue engineering. This robot incorporates components which are analogous to human bones, tendons, and muscle. It mimics human physiology by pulling the skeletal structure using a series of braided strings that represent tendon. The system can complete movements that are physiologically relevant to the supraspinatus tendon, such as abduction and adduction.

While the humanoid robot may be capable of generating movements which resemble movement of the human shoulder, it is important to ensure that the forces used to generate these movements are

appropriately transmitted to the tissue constructs growing on the model; insufficient stimulation results in a loss of extracellular matrix (ECM) structural integrity and tissue atrophy, while overstimulation leads to inflammation and degradative enzyme production [51]. Being able to measure and characterise loading in tissue engineering constructs is therefore crucial. To monitor load transmission, it is common practice to measure deformation, or strain, within a construct.

Although widely used in tissue engineering, conventional strain measurement tools such as extensometers or strain gauges do not adequately capture non-homogenous loading, such as that which would be provided by the humanoid robot [194]. Other important considerations include having sufficient resolution to detect small deformations in a sample and minimal contact to avoid disturbing the biomechanical environment of samples during tissue culture. Given these requirements, Digital Image Correlation (DIC) has emerged as a promising technology for strain characterisation in MSK tissue engineering.

The basic principle of DIC involves application of a random specular marker pattern on a sample, taking a series of images as the sample is being deformed, and tracking the movement of the pattern via cross-correlation throughout the deformation cycle [195]. Using two or more cameras, DIC offers 3D strain evaluation.

This chapter presents DIC as a novel method for strain characterisation of scaffold material during multiaxial loading. The aims of this chapter are i) to evaluate whether the humanoid robot presented by our research group provides appropriate tensile loading to tissue constructs throughout a movement cycle and ii) to evaluate whether the strain estimates provided by DIC are consistent with strain values obtained using conventional methods of tensile testing.

5.2 Materials and Methods

5.2.1 Robotic Arm Used for Study

Please refer to Section 3.1 for details on the robotic arm used in this study and for a description of the modifications made to the arm for tendon tissue engineering applications.

5.2.2 Description of Scaffold

A description of the bioreactor chamber scaffold design is provided Section 3.3.1.

5.2.3 Scaffold Preparation for DIC

Steps taken to prepare scaffold material for DIC analysis are outlined in Section 3.3.2.

5.2.4 Data Collection and Evaluation

Please refer to Section 3.3.3 for details on the DIC equipment used in this study. A description of testing conditions used for study can be found in Section 3.3.4. Section 3.3.5 provides details on data analysis. Parameters of interest for this study included peak strain and mean strain within samples, and Young's Modulus for validation of DIC data.

5.2.5 Validation of DIC Data

The method of validating DIC strain estimates has been outlined in Section 3.3.6.

5.2.6 Statistical Analysis

Normality of outcome parameters was verified with the Shapiro-Wilk test [221]. It was therefore possible to evaluate data using unpaired *t*-tests. Data are presented as mean and standard deviation (SD) in this study, unless otherwise indicated. Statistical significance for all data was determined at $p < 0.05$.

5.3 Results

From the movements tracked by the DIC system, it was possible to obtain three-dimensional strain maps for each recorded timepoint within a trial. To simplify the investigation and allow for comparison with conventional strain testing equipment, longitudinal tensile strain was analysed for the bioreactor chamber. A snapshot of the longitudinal tensile strain mapping has been provided in Figure 32. Throughout abduction/adduction movements, strain concentrations were noted towards the top middle sections of the scaffold material.

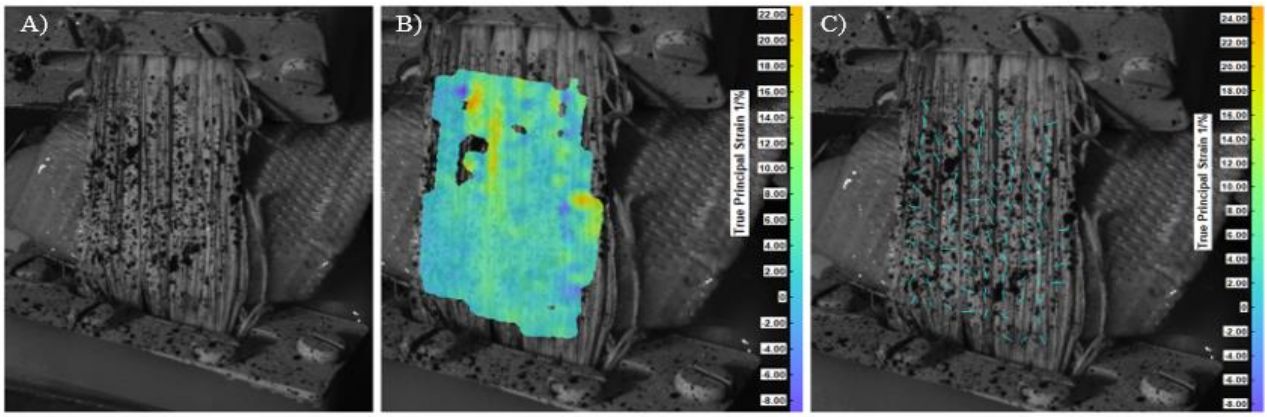


Figure 32: Strain map taken midway through an abduction-adduction trial. A) The speckle pattern applied to the bioreactor is shown here. B) The heat map represents tensile strain concentrations on the bioreactor chamber surface. C) Grid marks indicate the direction of strain in the sample.

Data were collected to compare resultant strain to tensile stress and range of motion applied over the course of a movement trial (Figure 33). As can be observed in Figure 33, peaks in average strain within the scaffold material match trends in muscle force from the supraspinatus position actuator. Stress and strain values tend to be maximised near the peak ROM of 20^{o} abduction and minimised when the humanoid arm moved towards -20^{o} abduction (20^{o} adduction). Abduction/adduction movements were completed at a frequency of 4 cycles per minute (0.07 Hz). The measured average and maximum stresses and strains for all abduction/adduction trials have been summarised in Table 17. Peak and average strain were estimated to be 6.10 (SD 1.80) % and 3.39 (SD 1.80) %, respectively, during task completion. Peak and average forces were found to be 63.2 (SD 9.1) N and 39.1 (SD 10.6) N, respectively.

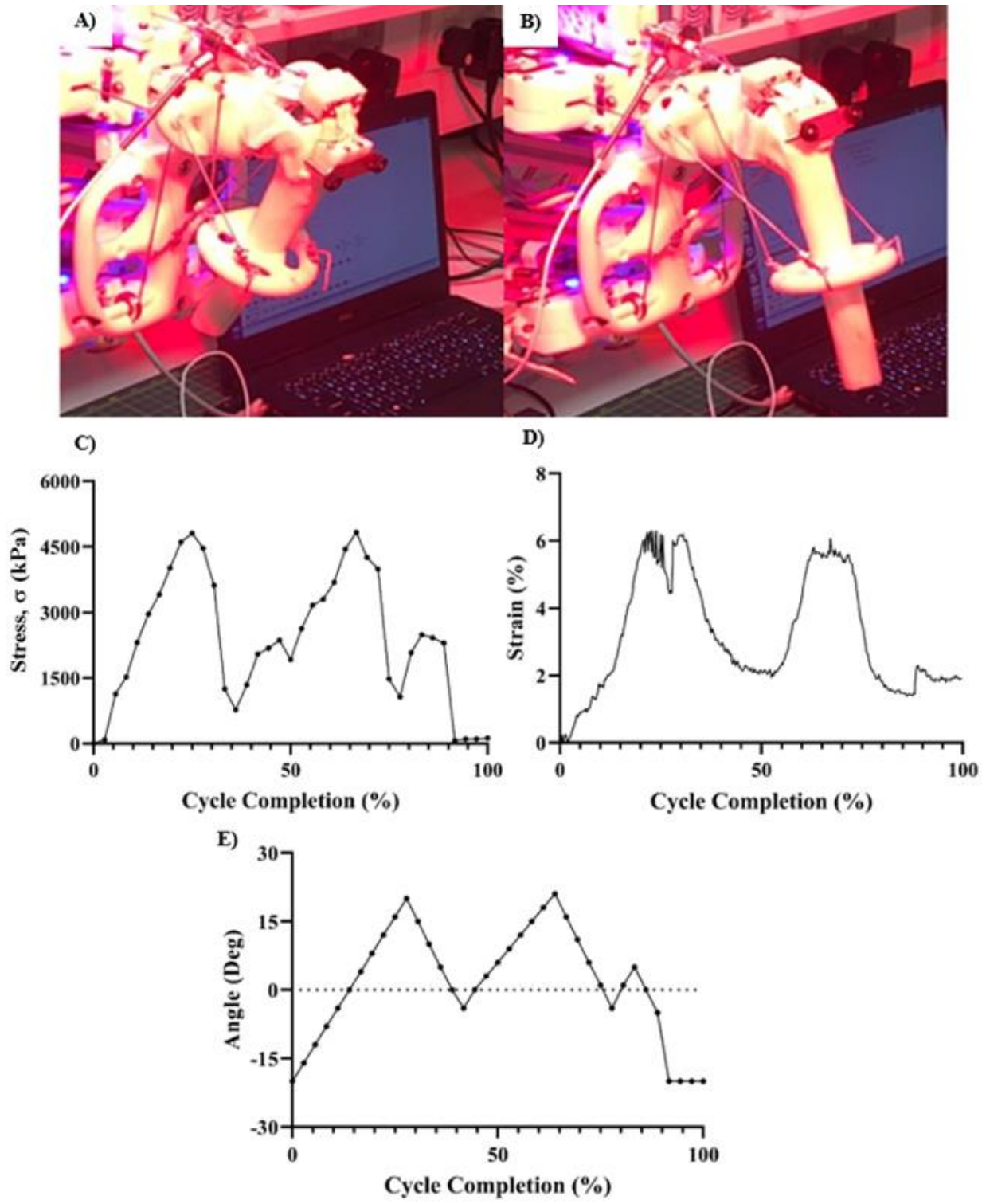


Figure 33: Comparison of tensile stress applied to tissue construct and resultant strain. A) The humanoid arm starts the movement cycle at an angle of -20º abduction. B) At 25 % into cycle completion, the arm is maximally abducted and at a point of high tensile stress. C) Stress recorded over the abduction-adduction trial. D) The resultant average longitudinal tensile strain over the course of an abduction-adduction trial, measured using DIC. E) Measured ROM throughout task completion.

Table 17: Outcome parameters for movement trials.

Average Strain (SD) %	Peak Strain (SD) %	Average Stress (SD) MPa	Peak Stress (SD) MPa
3.39 (1.10)	6.10 (1.80)	3.73 (1.03)	6.02 (0.86)

Destructive testing of the speckle-coated chambers in a tensile stage confirmed that forces measured during DIC were well within the linear elastic deformation range for these fibres. Data provided by the from the tensile stage were presented in terms of force and sample displacement. Scaffold dimensions were used to convert these values to stress and strain. The initial length of fibres in the chamber prior to tensile testing was 3 cm. The cross-sectional area of the bioreactor chambers was approximated as being a rectangle with dimensions of 350 μm x 50 μm. Previous imaging on electrospun fibres conducted by our research group found an average porosity of 40 %. Therefore, the actual surface area of contact used in stress strain calculations was 0.6 x 350 μm x 50 μm. The force-displacement curve and stress-strain curve that were obtained from the tensile testing equipment in the Gait lab are shown in Figure 34.

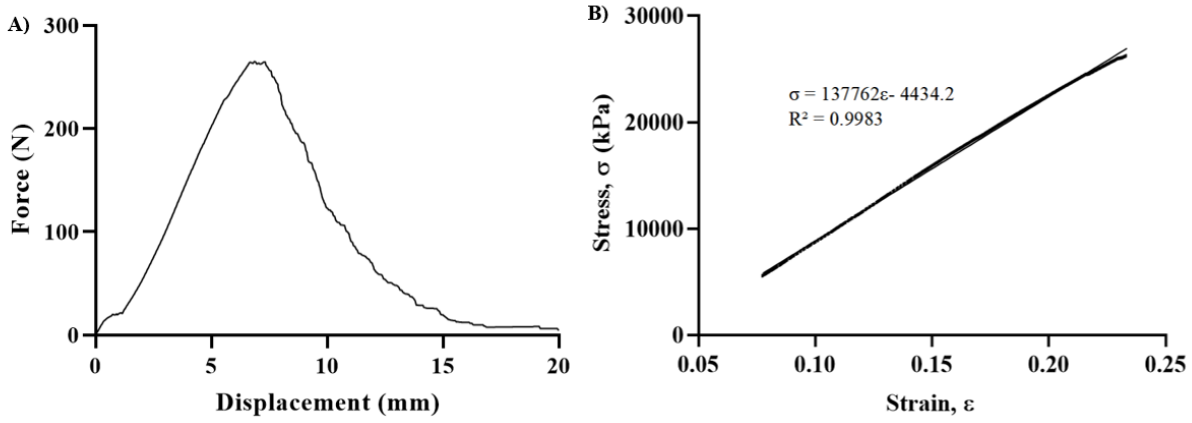


Figure 34: Results from Tensile Testing. A) The raw data obtained from the Zwick tensile stage is presented here. B) The linear portion of the curves obtained from tensile testing was converted to stress and strain values to calculate the Young's Modulus of the chambers. Data represent average values from all tensile tests (n=3) and error bands have not been shown.

The slope of the curve was calculated using displacement data from 2-7 mm of displacement. The initial portion of the curve was neglected given the 'bump' in the slope value that appears at the beginning of testing. This bump likely occurred due to fibres in the scaffold chamber not being fully straightened prior

to tensile loading. The Young's Modulus for the bioreactor chambers calculated using DIC data was found to be 142 (SD 72) MPa, compared to a value of 138 (SD 3) MPa from conventional tensile testing (Figure 35). These values indicate that stress-strain measurements from DIC and the tensile stage were well-matched, with no statistically significant difference ($p=0.8475$) being found when calculating Young's Modulus values.

5.4 Discussion and Suggested Future Research

Stress concentrations are typically found at the tendon-to bone attachment site in human supraspinatus tendons [246]. In this study, strain was typically concentrated towards the top and middle of the scaffold, closest to where the 'supraspinatus' actuator on the robot attaches to the scaffold. Qualitatively, this may indicate that the distribution of loading throughout the scaffold matches with stress distributions found in human rotator cuff tendon. A limitation worth noting is that the scaffold chambers used in this study were manually assembled, thereby introducing challenges for reproducibility of results from this study. While the three chambers evaluated in this study appeared to demonstrate consistent strain distribution profiles, differences in chamber assembly could introduce undesirable inconsistency in how strain is distributed throughout the scaffold material. Automated scaffold assembly would help reduce the risk of potential variability and should be considered as a future step in this project.

The tensile strain values reported in this study, ranging from 0-6 %, correspond well to the strain range suggested for optimal growth in recent tendon tissue engineering studies [12, 115-136]. Although only a limited number of studies have attempted to quantify strain in the human supraspinatus tendon during *in vivo* loading, the results from these studies are similar to the values obtained in this study [28, 247]. The peak and average tensile stress values reported in this study also fall within the range of stresses reported in previous tendon tissue literature [122]. Collectively, the results from this study suggest that the MSK robots are a promising and viable platform to enhance tendon tissue engineering

The Young's Modulus value calculated from the stress-strain curve was closely matched to the Young's Modulus calculated using DIC data. This validation step suggests that DIC may be suitable method for accurately measuring longitudinal tensile strain from motions applied with the MSK humanoid robot. It is important to note that other types of mechanical loading which may have been provided by the humanoid robot, such as shear, torsional, and compressive stresses and strains have not been discussed or quantified within this study. Future work will therefore be required to characterise other types of loading within the specimen given that these types of loading are known to influence cellular processes in tendon tissue [17].

While DIC was found to yield expected results for quantifying linear surface strain on biological samples in this study, several limitations of this technology were identified. These challenges need to be addressed prior to use of DIC for real-time strain measurement in tendon tissue engineering:

- The speckle pattern was applied directly to the bioactive filaments in the chamber. This acrylic coating would likely have toxic effects for cells and may limit applicability of DIC for real-time strain quantification during tissue engineering experiments with the humanoid robot. In future experiments, this may be mitigated by exploring alternative coating materials for the sample. Use of water soluble dyes such as methylene blue have been explored in a previous study which analysed strain in Achilles tendon tissue [198].

- Given the small size of the chamber and the need to focus closely on the sample at high resolution, the plane of vision for the DIC system is very small. In more complicated arm movements, this results in numerous out-of-plane movements, whereby strain values are not being calculated. Given that each successive strain measurement requires comparison to previous measurements, one out of plane movement would result in no data being collected for the remainder of the trial. To mitigate this challenge while maintaining a high resolution, a future experimental setup should comprise additional cameras for image capture.

- As a non-contact, non-destructive method of strain analysis, DIC was only able to provide strain data on fibres at the surface of the tissue construct. Given that the scaffold chamber used in this study consists of multiple fibre bundles and is not an isotropic body, strain likely varies across the thickness of the construct. Furthermore, existing literature suggests that native tissue demonstrates non-uniform deformation between superficial and deep layers [26-28]. The validity of strain estimates from DIC are therefore limited in this application. Strain characterisation techniques such as quantitative ultrasound strain elastography, and digital volume correlation may be appropriate alternatives to DIC for capturing the behaviour of complex 3D scaffolds which have non-uniform strain distributions [25, 140, 248].

5.5 Chapter Summary

This chapter presents DIC as a technology to evaluate strain transmission to scaffold material during loading regimes applied by an MSK humanoid shoulder. Comparison of results from this study with previously published tendon engineering literature suggest that stresses from the humanoid robot were within a desired range of values. Moreover, DIC was shown to be yield strain values consistent with traditional tensile testing. Future research directions for improving strain characterisation during tendon tissue engineering have also been discussed in this study.

Strain characterisation is important within tendon tissue engineering, as this information can help identify the mechanical conditions which result in optimal tissue development. A potential benefit of this research is the eventual use of engineered tendon tissue grafts for clinical use. Enhanced repair strategies for torn shoulder tendons may improve the quality of life for patients, by reducing surgical failure rates, and for society, by decreasing the economic impact of rotator cuff disease.

6. Conclusion

6.1 Summary of Thesis

Rotator cuff tendon injuries are a common cause of debilitation and are increasing in prevalence, presenting in upwards of 10 % of adults over the age of 50. The supraspinatus is the most commonly injured rotator cuff tendon. The economic and social impacts of rotator cuff disease are significant, with billions of dollars in annual healthcare expenditure. Despite the burden of this disease on healthcare systems, patient outcomes following treatment remain poor. A promising strategy to address this challenge is the development of engineered tendon grafts for clinical use.

A major barrier in the development of clinically useful grafts has been a lack of advanced bioreactor systems which can replicate the mechanical environment of healthy native tendon tissue. In response to this translational gap, MSK humanoid robots have been proposed as a platform for tendon tissue engineering. The work presented in this thesis contributes to the development of an MSK robotic shoulder intended for supraspinatus tendon tissue engineering through two sub-tasks. The first subtask focussed on evaluating the kinematic and force profiles of the humanoid robot, while the second sub-task investigated whether forces used to complete movements were appropriately transmitted to scaffold materials for tendon tissue culture. Although several MSK humanoids are in development, this thesis is part of the first attempt to use this technology as a platform for tendon tissue engineering.

Chapter 4 addresses the first sub-task of this thesis. It consists of an UE motion study to examine whether the MSK humanoid robot can replicate the movement and force profiles of a healthy human shoulder. The humanoid robot was configured to have 7 actuating muscles positioned around the robotic shoulder in analogous positions to the human rotator cuff[**]. Three joint configurations were evaluated in the motion study: the humanoid's original ball and socket joint, a bipolar clinical implant which was re-configured

[**] The teres minor, subscapularis, and infraspinatus muscles were represented by 2 actuators each, while 1 actuator was used to imitate supraspinatus tendon function.

for use with the MSK robot, and a reverse ball and socket joint. As a comparative reference, 40 healthy human participants with no history of shoulder injury or surgery were recruited for the study.

Since no consensus exists as to one task which can adequately represent functional UE use, the task protocol for this study only consisted of abduction/adduction movements up to 30º and 90º ROM in the scapular plane. This movement pattern was prioritised as the supraspinatus tendon is largely responsible for abduction up to 15º ROM and contributes significantly to ROM up to 90º. Each task was completed at two movement speeds: a slow, controlled movement (at a target movement speed of 10 deg/s) and a faster movement (at a target movement speed of 30 deg/s). Motion was tracked using retro-reflective markers. The marker protocol for this study was an adaption of the commercially popular PiG upper body model. Kinematic modelling was carried out in Vicon Nexus™. It was possible to directly measure muscle forces during task completion for the humanoid robot using a load cell. The AMS MSK modelling software developed by AnyBody Technology™ was used for estimating supraspinatus muscle forces as these were not possible to directly measure.

This study indicated that the humanoid robot can accurately replicate slow, controlled abduction movements up to 30º ROM with the original ball and socket joint configuration. When evaluating the force and kinematic profiles of the humanoid robot during the fast movement task, it was possible to identify differences in performance depending on joint configuration. The original joint configuration and the clinical implant were unable to match the kinematic profiles of human participants for task completion at a faster movement speed but were able to closely replicate the force profiles throughout the task. In contrast, the reverse shoulder joint configuration successfully replicated the kinematic profile of human participants but was unable to provide similar a range of forces during task completion. These results indicate that at a faster movement speed, the humanoid arm was able to either match the kinematic profile or the force profile of human participants, but not both simultaneously. Improving the consistency between kinematic profile and range of forces used to apply a motion will therefore be a focus of future design modifications to the robotic shoulder. This may be achieved through inclusion of a scapular

component and additional muscles. Given that it was possible to observe differences in kinematic and force profiles depending on joint configuration, another potential use of MSK humanoid robots was identified in this study – testing biomedical orthopaedic implants. Similar to tendon tissue engineering, a major gap in current implant testing is the lack of systems which can accurately model *in vivo* mechanical environments.

The second sub-task of this thesis, examining the transmission of mechanical load to scaffold material, was investigated in Chapter 5 with a DIC study. The humanoid robot used a joint configuration which was designed for attachment of a small, flexible bioreactor scaffold in the supraspinatus tendon position. The DIC equipment consisted of two cameras, enabling 3D strain analysis. A speckle pattern was applied to the surface of the scaffold material and deformation throughout the movement trial was tracked.

Strain concentrations in the scaffold were noted near the attachment to the robot's 'supraspinatus' position actuator. This finding was consistent with human physiology, given that stress concentrations in the rotator cuff are typically found at the tendon-bone interface. Average and peak strains found in the construct were within the range of strains reported in previous tendon tissue engineering studies for optimal tissue growth. The strain values found in this investigation were also consistent with the strain ranges reported in the limited number of studies which have attempted to quantify strain within the supraspinatus tendon during *in vivo* loading. Altogether, the findings from this study suggest that MSK robots are a viable and promising technology to enhance tendon tissue engineering.

Conventional tensile testing was used to validate the accuracy of strain measurements obtained using DIC. While the measurements obtained through DIC were found to be adequately similar to results obtained through conventional tensile testing, several key limitations of this technology were identified. These challenges need to be addressed prior to use of DIC for tendon tissue engineering.

6.2 Summary of Findings

Several key findings have been identified from this research project:

- The humanoid robot used in this study was able to replicate either the kinematic or kinetic profile of human participants during task completion, but not both simultaneously. This finding suggests that with adaptation, the humanoid robot may be able to reasonably replicate the human shoulder for abduction/adduction tasks.
- From this study, it is clear that a scapular component should be incorporated in future prototypes of the humanoid shoulder.
- The ability to discern differences in the performance of different joint configurations suggests that humanoid robots may be a useful technology in biomedical implant testing.
- The humanoid robot can transmit strain to scaffold material in quantities which have been shown in previous literature to result in optimal tissue growth. Strain from the humanoid robot is distributed in a non-uniform pattern similar to what has been observed *in vivo*.
- While DIC was a suitable strain characterisation technique for the pilot phase work presented in this study, there are limitations associated with this technique that would need to be addressed in future work.

6.3 Limitations and Suggested Work

The primary goal of this research project was to assess the potential a humanoid MSK robot as a platform for rotator cuff tendon tissue engineering. While benefits and shortcomings of the current robotic shoulder have been identified, there are known limitations which reduce the ready acceptance of results presented in this thesis. Additional work is necessary to assess the full potential of MSK robots for biomedical applications. This section highlights limitations of results presented in this thesis and suggests future work to enhance the potential clinical impact of the humanoid robot presented in this study.

The motion study in Chapter 4 relied on several simplifying assumptions, at the cost of accuracy and potentially valuable information. Upper body PiG, the kinematic model used in this study, neglects all scapular contributions by approximating shoulder movement to the GH joint. From 30^{o} to 90^{o} abduction, the scapula has been estimated to contribute up to 40 % of this motion. By differentiating between GH joint and scapular contributions to ROM during movement tasks, it would have been possible to better quantify how the lack of a scapula impacts the functionality of the current humanoid robot. In future work to further characterise the humanoid robot, a kinematic model which accounts for scapular movement is recommended. This may be achieved either through newer non-invasive methods suggested by Cutti et al. [168], or through traditional methods, such as intracortical bone pins [173]. An additional advantage of intracortical bone pins would be the elimination of STA, thereby improving the accuracy of kinematic model outputs.

Results from the MSK model used to estimate human supraspinatus muscle forces must be interpreted cautiously and further evaluation and validation of MSK modelling results is recommended. In future studies, this may include intramuscular EMG to qualitatively compare trends in rotator cuff activation with estimated muscle forces. Another potential strategy could include a comparison of model-predicated and measured moment arms for the supraspinatus muscle. This comparison is valuable as moment arms are an important element for accurate estimation of muscle forces. This strategy has been used in previous studies to evaluate the performance of MSK models for estimation of rotator cuff muscle forces [249].

Future applications of the humanoid MSK robot should include exploration of additional movements which are physiologically relevant to the supraspinatus tendon, including movements based upon rehabilitation exercises. This may include additional ROM tasks, such as forward elevation and internal/external rotation. To achieve this, future prototypes of the humanoid robot should incorporate a scapula and additional actuators to imitate muscles which contribute to shoulder motion in humans, such as the deltoid, pectoralis major, and trapezius muscles.

Future work should investigate other types of mechanical loading experienced during movement, such as compression, torsion, and shear stress. It would also be worthwhile to measure these types of loading in each direction, given that tendon tissue is known to demonstrate anisotropic properties. DIC may play a role in characterising this loading, although its limitation to only providing surface level analysis and the practical challenge of finding appropriate biocompatible dyes limit its usefulness. Quantitative ultrasound strain elastography and digital volume correlation are complementary imaging strategies which may be relevant to development of appropriate loading regimes for the humanoid robot.

6.4 Closing Remarks

In summary, this thesis has contributed to the development of a novel robotic shoulder for use in tendon tissue engineering. Although significant work is necessary to enhance this humanoid shoulder and assess the feasibility of this strategy for development of clinically useful tendon grafts, the MSK robot has demonstrated the potential to overcome limitations associated with current bioreactor systems. Future work in this project will include design changes to enhance the physiologic relevance of the humanoid robot, development of task protocols which represent a broader range of functional shoulder use, and improved characterisation of the direction and types of loading provided by the MSK humanoid robot. The technology presented in this project has the potential to improve quality of life for individuals, by decreasing pain and risk of repair failure, for the healthcare systems, by reducing the number of revision surgeries performed annually, and for the economy, by improving workplace productivity and lowering healthcare costs.

References

[1] S. Gumina *et al.*, "The association between body fat and rotator cuff tear: the influence on rotator cuff tear sizes," (in eng), *J Shoulder Elbow Surg,* vol. 23, no. 11, pp. 1669-74, Nov 2014, doi: 10.1016/j.jse.2014.03.016.

[2] S. Tempelhof, S. Rupp, and R. Seil, "Age-related prevalence of rotator cuff tears in asymptomatic shoulders," (in eng), *J Shoulder Elbow Surg,* vol. 8, no. 4, pp. 296-9, Jul-Aug 1999.

[3] H. Minagawa *et al.*, "Prevalence of symptomatic and asymptomatic rotator cuff tears in the general population: From mass-screening in one village," (in eng), *J Orthop,* vol. 10, no. 1, pp. 8-12, 2013, doi: 10.1016/j.jor.2013.01.008.

[4] G. Spargoli, "Supraspinatus tendon pathomechanics: a current concepts review," (in eng), *Int J Sports Phys Ther,* vol. 13, no. 6, pp. 1083-1094, Dec 2018.

[5] C. Hopkins *et al.*, "Critical review on the socio-economic impact of tendinopathy," (in eng), *Asia Pac J Sports Med Arthrosc Rehabil Technol,* vol. 4, pp. 9-20, Apr 2016, doi: 10.1016/j.asmart.2016.01.002.

[6] R. C. Mather, 3rd *et al.*, "The societal and economic value of rotator cuff repair," (in eng), *J Bone Joint Surg Am,* vol. 95, no. 22, pp. 1993-2000, Nov 20 2013, doi: 10.2106/jbjs.l.01495.

[7] J. Bishop, S. Klepps, I. K. Lo, J. Bird, J. N. Gladstone, and E. L. Flatow, "Cuff integrity after arthroscopic versus open rotator cuff repair: a prospective study," (in eng), *J Shoulder Elbow Surg,* vol. 15, no. 3, pp. 290-9, May-Jun 2006, doi: 10.1016/j.jse.2005.09.017.

[8] L. M. Galatz, C. M. Ball, S. A. Teefey, W. D. Middleton, and K. Yamaguchi, "The outcome and repair integrity of completely arthroscopically repaired large and massive rotator cuff tears," (in eng), *J Bone Joint Surg Am,* vol. 86, no. 2, pp. 219-24, Feb 2004.

[9] N. Andarawis-Puri, E. L. Flatow, and L. J. Soslowsky, "Tendon basic science: Development, repair, regeneration, and healing," (in eng), *J Orthop Res,* vol. 33, no. 6, pp. 780-4, Jun 2015, doi: 10.1002/jor.22869.

[10] B. J. Cole, L. P. McCarty, 3rd, R. W. Kang, W. Alford, P. B. Lewis, and J. K. Hayden, "Arthroscopic rotator cuff repair: prospective functional outcome and repair integrity at minimum 2-year follow-up," (in eng), *J Shoulder Elbow Surg,* vol. 16, no. 5, pp. 579-85, Sep-Oct 2007, doi: 10.1016/j.jse.2006.12.011.

[11] N. B. Jain, L. D. Higgins, E. Losina, J. Collins, P. E. Blazar, and J. N. Katz, "Epidemiology of musculoskeletal upper extremity ambulatory surgery in the United States," (in eng), *BMC Musculoskelet Disord,* vol. 15, p. 4, Jan 8 2014, doi: 10.1186/1471-2474-15-4.

[12] T. Wang *et al.*, "Bioreactor design for tendon/ligament engineering," (in eng), *Tissue Eng Part B Rev,* vol. 19, no. 2, pp. 133-46, Apr 2013, doi: 10.1089/ten.TEB.2012.0295.

[13] P.-A. Mouthuy and A. Carr, "Growing tissue grafts on humanoid robots: A future strategy in regenerative medicine?," *Sci Robot,* vol. 2, no. 4, p. eaam5666, 2017, doi: 10.1126/scirobotics.aam5666.

[14] D. T. Kirkendall and W. E. Garrett, "Function and biomechanics of tendons," (in eng), *Scand J Med Sci Sports,* vol. 7, no. 2, pp. 62-6, Apr 1997, doi: 10.1111/j.1600-0838.1997.tb00120.x.

[15] C. T. Thorpe and H. R. Screen, "Tendon Structure and Composition," (in eng), *Adv Exp Med Biol,* vol. 920, pp. 3-10, 2016, doi: 10.1007/978-3-319-33943-6_1.

[16] H. L. Birch, "Tendon matrix composition and turnover in relation to functional requirements," (in eng), *Int J Exp Pathol,* vol. 88, no. 4, pp. 241-8, Aug 2007, doi: 10.1111/j.1365-2613.2007.00552.x.

[17] J. G. Snedeker and J. Foolen, "Tendon injury and repair - A perspective on the basic mechanisms of tendon disease and future clinical therapy," (in eng), *Acta Biomater,* vol. 63, pp. 18-36, Nov 2017, doi: 10.1016/j.actbio.2017.08.032.

[18] C. M. McNeilly, A. Banes, M. Benjamin, and Ralphs, Jr., "Tendon cells in vivo form a three dimensional network of cell processes linked by gap junctions," (in English), *J. Anat.*, vol. 189, pp. 593-600, 1996.

[19] H. R. Screen, D. E. Berk, K. E. Kadler, F. Ramirez, and M. F. Young, "Tendon functional extracellular matrix," (in eng), *J Orthop Res,* vol. 33, no. 6, pp. 793-9, Jun 2015, doi: 10.1002/jor.22818.

[20] C. T. Thorpe, P. D. Clegg, and H. L. Birch, "A review of tendon injury: why is the equine superficial digital flexor tendon most at risk?," (in eng), *Equine Vet J,* vol. 42, no. 2, pp. 174-80, Mar 2010, doi: 10.2746/042516409x480395.

[21] S. P. Lake, K. S. Miller, D. M. Elliott, and L. J. Soslowsky, "Tensile properties and fiber alignment of human supraspinatus tendon in the transverse direction demonstrate inhomogeneity, nonlinearity, and regional isotropy," (in eng), *J Biomech,* vol. 43, no. 4, pp. 727-32, Mar 3 2010, doi: 10.1016/j.jbiomech.2009.10.017.

[22] C. T. Thorpe, C. P. Udeze, H. L. Birch, P. D. Clegg, and H. R. Screen, "Specialization of tendon mechanical properties results from interfascicular differences," (in eng), *J R Soc Interface,* vol. 9, no. 76, pp. 3108-17, Nov 7 2012, doi: 10.1098/rsif.2012.0362.

[23] C. T. Thorpe, C. Klemt, G. P. Riley, H. L. Birch, P. D. Clegg, and H. R. Screen, "Helical sub-structures in energy-storing tendons provide a possible mechanism for efficient energy storage and return," (in eng), *Acta Biomater,* vol. 9, no. 8, pp. 7948-56, Aug 2013, doi: 10.1016/j.actbio.2013.05.004.

[24] M. J. Bey and K. A. Derwin, "Measurement of in vivo tendon function," (in eng), *J Shoulder Elbow Surg,* vol. 21, no. 2, pp. 149-57, Feb 2012, doi: 10.1016/j.jse.2011.10.023.

[25] L. A. Chernak and D. G. Thelen, "Tendon motion and strain patterns evaluated with two-dimensional ultrasound elastography," (in eng), *J Biomech,* vol. 45, no. 15, pp. 2618-23, Oct 11 2012, doi: 10.1016/j.jbiomech.2012.08.001.

[26] L. C. Slane and D. G. Thelen, "Achilles tendon displacement patterns during passive stretch and eccentric loading are altered in middle-aged adults," (in eng), *Med Eng Phys,* vol. 37, no. 7, pp. 712-6, Jul 2015, doi: 10.1016/j.medengphy.2015.04.004.

[27] R. L. Chimenti, A. S. Flemister, J. Ketz, M. Bucklin, M. R. Buckley, and M. S. Richards, "Ultrasound strain mapping of Achilles tendon compressive strain patterns during dorsiflexion," (in eng), *J Biomech,* vol. 49, no. 1, pp. 39-44, Jan 4 2016, doi: 10.1016/j.jbiomech.2015.11.008.

[28] Y. S. Kim, J. M. Kim, L. U. Bigliani, H. J. Kim, and H. W. Jung, "In vivo strain analysis of the intact supraspinatus tendon by ultrasound speckles tracking imaging," (in eng), *J Orthop Res,* vol. 29, no. 12, pp. 1931-7, Dec 2011, doi: 10.1002/jor.21470.

[29] M. Lavagnino, M. E. Wall, D. Little, A. J. Banes, F. Guilak, and S. P. Arnoczky, "Tendon mechanobiology: Current knowledge and future research opportunities," (in eng), *J Orthop Res,* vol. 33, no. 6, pp. 813-22, Jun 2015, doi: 10.1002/jor.22871.

[30] B. Cheng *et al.*, "Cellular mechanosensing of the biophysical microenvironment: A review of mathematical models of biophysical regulation of cell responses," (in eng), *Phys Life Rev,* vol. 22-23, pp. 88-119, Dec 2017, doi: 10.1016/j.plrev.2017.06.016.

[31] T. D. Plant, "TRPs in mechanosensing and volume regulation," (in eng), *Handb Exp Pharmacol,* vol. 223, pp. 743-66, 2014, doi: 10.1007/978-3-319-05161-1_2.

[32] X. Varelas, "The Hippo pathway effectors TAZ and YAP in development, homeostasis and disease," (in eng), *Development,* vol. 141, no. 8, pp. 1614-26, Apr 2014, doi: 10.1242/dev.102376.

[33] M. Stolk, F. Klatte-Schulz, A. Schmock, S. Minkwitz, B. Wildemann, and M. Seifert, "New insights into tenocyte-immune cell interplay in an in vitro model of inflammation," (in eng), *Sci Rep,* vol. 7, no. 1, p. 9801, Aug 29 2017, doi: 10.1038/s41598-017-09875-x.

[34] 3D4Medical, "Complete Anatomy," 3D4Medical, Ed., ed, 2019.

[35] P. Villasenor-Ovies *et al.*, "Clinical anatomy of the elbow and shoulder," (in eng), *Reumatol Clin,* vol. 8 Suppl 2, pp. 13-24, Dec-2013 Jan 2012, doi: 10.1016/j.reuma.2012.10.009.

[36] D. Wattanaprakornkul, M. Halaki, C. Boettcher, I. Cathers, and K. A. Ginn, "A comprehensive analysis of muscle recruitment patterns during shoulder flexion: an electromyographic study," (in eng), *Clin Anat,* vol. 24, no. 5, pp. 619-26, Jul 2011, doi: 10.1002/ca.21123.

[37] D. Reed, I. Cathers, M. Halaki, and K. Ginn, "Does supraspinatus initiate shoulder abduction?," (in eng), *J Electromyogr Kinesiol,* vol. 23, no. 2, pp. 425-9, Apr 2013, doi: 10.1016/j.jelekin.2012.11.008.

[38] D. Wattanaprakornkul, I. Cathers, M. Halaki, and K. A. Ginn, "The rotator cuff muscles have a direction specific recruitment pattern during shoulder flexion and extension exercises," (in eng), *J Sci Med Sport,* vol. 14, no. 5, pp. 376-82, Sep 2011, doi: 10.1016/j.jsams.2011.01.001.

[39] D. T. Tardo, M. Halaki, I. Cathers, and K. A. Ginn, "Rotator cuff muscles perform different functional roles during shoulder external rotation exercises," (in eng), *Clin Anat,* vol. 26, no. 2, pp. 236-43, Mar 2013, doi: 10.1002/ca.22128.

[40] G. L. Vairo, M. L. Duffey, B. D. Owens, and K. L. Cameron, "Clinical descriptive measures of shoulder range of motion for a healthy, young and physically active cohort," (in eng), *Sports Med Arthrosc Rehabil Ther Technol,* vol. 4, no. 1, p. 33, Sep 10 2012, doi: 10.1186/1758-2555-4-33.

[41] J. H. Lam and B. Bordoni, "Anatomy, Shoulder and Upper Limb, Arm Abductor Muscles," in *StatPearls*. Treasure Island (FL): StatPearls Publishing, 2020.

[42] I. Gunal, N. Kose, O. Erdogan, E. Gokturk, and S. Seber, "Normal range of motion of the joints of the upper extremity in male subjects, with special reference to side," (in eng), *J Bone Joint Surg Am,* vol. 78, no. 9, pp. 1401-4, Sep 1996, doi: 10.2106/00004623-199609000-00017.

[43] J. Winkel, R. Westgaard, A. Mital, Å. Kilbom, and S. Kumar, "Occupational and individual risk factors for shoulder-neck complaints: Part II – The scientific basis (literature review) for the guide," in *Elsevier Ergonomics Book Series*, vol. 1: Elsevier, 2000, pp. 83-102.

[44] M. Artus, T. A. Holt, and J. Rees, "The painful shoulder: an update on assessment, treatment, and referral," (in eng), *Br J Gen Pract,* vol. 64, no. 626, pp. e593-5, Sep 2014, doi: 10.3399/bjgp14X681577.

[45] E. V. Fehringer, J. Sun, L. S. VanOeveren, B. K. Keller, and F. A. Matsen, 3rd, "Full-thickness rotator cuff tear prevalence and correlation with function and co-morbidities in patients sixty-five years and older," (in eng), *J Shoulder Elbow Surg,* vol. 17, no. 6, pp. 881-5, Nov-Dec 2008, doi: 10.1016/j.jse.2008.05.039.

[46] S. Moosmayer, H. J. Smith, R. Tariq, and A. Larmo, "Prevalence and characteristics of asymptomatic tears of the rotator cuff: an ultrasonographic and clinical study," (in eng), *J Bone Joint Surg Br,* vol. 91, no. 2, pp. 196-200, Feb 2009, doi: 10.1302/0301-620x.91b2.21069.

[47] J. M. Archambault, J. P. Wiley, and R. C. Bray, "Exercise loading of tendons and the development of overuse injuries. A review of current literature," (in eng), *Sports Med,* vol. 20, no. 2, pp. 77-89, Aug 1995, doi: 10.2165/00007256-199520020-00003.

[48] J. H. Wang *et al.*, "Cyclic mechanical stretching of human tendon fibroblasts increases the production of prostaglandin E2 and levels of cyclooxygenase expression: a novel in vitro model study," (in eng), *Connect Tissue Res,* vol. 44, no. 3-4, pp. 128-33, 2003.

[49] M. Skutek, M. van Griensven, J. Zeichen, N. Brauer, and U. Bosch, "Cyclic mechanical stretching enhances secretion of Interleukin 6 in human tendon fibroblasts," (in eng), *Knee Surg Sports Traumatol Arthrosc,* vol. 9, no. 5, pp. 322-6, Sep 2001, doi: 10.1007/s001670100217.

[50] L. J. Soslowsky *et al.*, "Neer Award 1999. Overuse activity injures the supraspinatus tendon in an animal model: a histologic and biomechanical study," (in eng), *J Shoulder Elbow Surg,* vol. 9, no. 2, pp. 79-84, Mar-Apr 2000.

[51] S. P. Arnoczky, M. Lavagnino, and M. Egerbacher, "The mechanobiological aetiopathogenesis of tendinopathy: is it the over-stimulation or the under-stimulation of tendon cells?," (in eng), *Int J Exp Pathol,* vol. 88, no. 4, pp. 217-26, Aug 2007, doi: 10.1111/j.1365-2613.2007.00548.x.

[52] A. P. Boesen *et al.*, "Tendon and skeletal muscle matrix gene expression and functional responses to immobilisation and rehabilitation in young males: effect of growth hormone administration," (in eng), *J Physiol,* vol. 591, no. 23, pp. 6039-52, Dec 1 2013, doi: 10.1113/jphysiol.2013.261263.

[53] M. D. de Boer, C. N. Maganaris, O. R. Seynnes, M. J. Rennie, and M. V. Narici, "Time course of muscular, neural and tendinous adaptations to 23 day unilateral lower-limb suspension in young men," (in eng), *J Physiol,* vol. 583, no. Pt 3, pp. 1079-91, Sep 15 2007, doi: 10.1113/jphysiol.2007.135392.

[54] K. Dideriksen *et al.*, "Tendon collagen synthesis declines with immobilization in elderly humans: no effect of anti-inflammatory medication," (in eng), *J Appl Physiol (1985),* vol. 122, no. 2, pp. 273-282, Feb 1 2017, doi: 10.1152/japplphysiol.00809.2015.

[55] B. J. F. Dean, S. G. Dakin, N. L. Millar, and A. J. Carr, "Review: Emerging concepts in the pathogenesis of tendinopathy," (in eng), *Surgeon,* vol. 15, 2017, doi: 10.1016/j.surge.2017.05.005.

[56] R. J. Williams, 3rd, E. Attia, T. L. Wickiewicz, and J. A. Hannafin, "The effect of ciprofloxacin on tendon, paratenon, and capsular fibroblast metabolism," (in eng), *Am J Sports Med,* vol. 28, no. 3, pp. 364-9, May-Jun 2000, doi: 10.1177/03635465000280031401.

[57] F. Kaleagasioglu and E. Olcay, "Fluoroquinolone-induced tendinopathy: etiology and preventive measures," (in eng), *Tohoku J Exp Med,* vol. 226, no. 4, pp. 251-8, Apr 2012.

[58] J. F. Haines, "Bilateral rupture of the Achilles tendon in patients on steroid therapy," (in eng), *Ann Rheum Dis,* vol. 42, no. 6, pp. 652-4, Dec 1983, doi: 10.1136/ard.42.6.652.

[59] R. A. Kotnis, J. C. Halstead, and P. J. Hormbrey, "Atraumatic bilateral Achilles tendon rupture: an association of systemic steroid treatment," (in eng), *J Accid Emerg Med,* vol. 16, no. 5, pp. 378-9, Sep 1999, doi: 10.1136/emj.16.5.378.

[60] D. M. Newnham, J. G. Douglas, J. S. Legge, and J. A. Friend, "Achilles tendon rupture: an underrated complication of corticosteroid treatment," (in eng), *Thorax,* vol. 46, no. 11, pp. 853-4, Nov 1991, doi: 10.1136/thx.46.11.853.

[61] M. W. Hast, J. A. Abboud, and L. J. Soslowsky, "Exploring the role of hypercholesterolemia in tendon health and repair," (in eng), *Muscles Ligaments Tendons J,* vol. 4, no. 3, pp. 275-9, Jul 2014.

[62] G. P. Riley *et al.*, "Matrix metalloproteinase activities and their relationship with collagen remodelling in tendon pathology," (in eng), *Matrix Biol,* vol. 21, no. 2, pp. 185-95, Mar 2002, doi: 10.1016/s0945-053x(01)00196-2.

[63] B. Taylor, A. Cheema, and L. Soslowsky, "Tendon Pathology in Hypercholesterolemia and Familial Hypercholesterolemia," (in eng), *Curr Rheumatol Rep,* vol. 19, no. 12, p. 76, Nov 4 2017, doi: 10.1007/s11926-017-0704-2.

[64] M. Kuzma-Kuzniarska, H. R. Cornell, M. C. Moneke, A. J. Carr, and P. A. Hulley, "Lovastatin-Mediated Changes in Human Tendon Cells," (in eng), *J Cell Physiol,* vol. 230, no. 10, pp. 2543-51, Oct 2015, doi: 10.1002/jcp.25010.

[65] T. A. Ranger, A. M. Wong, J. L. Cook, and J. E. Gaida, "Is there an association between tendinopathy and diabetes mellitus? A systematic review with meta-analysis," (in eng), *Br J Sports Med,* vol. 50, no. 16, pp. 982-9, Aug 2016, doi: 10.1136/bjsports-2015-094735.

[66] J. Pingel *et al.*, "Inflammatory and Metabolic Alterations of Kager's Fat Pad in Chronic Achilles Tendinopathy," (in eng), *PLoS One,* vol. 10, no. 5, p. e0127811, 2015, doi: 10.1371/journal.pone.0127811.

[67] S. E. Gwilym *et al.*, "Genetic influences in the progression of tears of the rotator cuff," (in eng), *J Bone Joint Surg Br,* vol. 91, no. 7, pp. 915-7, Jul 2009, doi: 10.1302/0301-620x.91b7.22353.

[68] N. H. Vaughn, H. Stepanyan, R. A. Gallo, and A. Dhawan, "Genetic Factors in Tendon Injury: A Systematic Review of the Literature," (in eng), *Orthop J Sports Med,* vol. 5, no. 8, p. 2325967117724416, Aug 2017, doi: 10.1177/2325967117724416.

[69] M. J. Peffers *et al.*, "Proteomic analysis reveals age-related changes in tendon matrix composition, with age- and injury-specific matrix fragmentation," (in eng), *J Biol Chem,* vol. 289, no. 37, pp. 25867-78, Sep 12 2014, doi: 10.1074/jbc.M114.566554.

[70] R. A. Bank, J. M. TeKoppele, G. Oostingh, B. L. Hazleman, and G. P. Riley, "Lysylhydroxylation and non-reducible crosslinking of human supraspinatus tendon collagen: changes with age and in chronic rotator cuff tendinitis," (in eng), *Ann Rheum Dis,* vol. 58, no. 1, pp. 35-41, Jan 1999, doi: 10.1136/ard.58.1.35.

[71] T. Kondo and Y. Ishida, "Molecular pathology of wound healing," (in eng), *Forensic Sci Int,* vol. 203, no. 1-3, pp. 93-8, Dec 15 2010, doi: 10.1016/j.forsciint.2010.07.004.

[72] N. L. Millar, G. A. Murrell, and I. B. McInnes, "Inflammatory mechanisms in tendinopathy - towards translation," (in eng), *Nat Rev Rheumatol,* vol. 13, no. 2, pp. 110-122, Jan 25 2017, doi: 10.1038/nrrheum.2016.213.

[73] P. B. Voleti, M. R. Buckley, and L. J. Soslowsky, "Tendon healing: repair and regeneration," (in eng), *Annu Rev Biomed Eng,* vol. 14, pp. 47-71, 2012, doi: 10.1146/annurev-bioeng-071811-150122.

[74] B. J. Dean, S. L. Franklin, and A. J. Carr, "A systematic review of the histological and molecular changes in rotator cuff disease," (in eng), *Bone Joint Res,* vol. 1, no. 7, pp. 158-66, Jul 2012, doi: 10.1302/2046-3758.17.2000115.

[75] W. Petersen, T. Pufe, B. Kurz, R. Mentlein, and B. Tillmann, "Angiogenesis in fetal tendon development: spatial and temporal expression of the angiogenic peptide vascular endothelial cell

growth factor," (in eng), *Anat Embryol (Berl),* vol. 205, no. 4, pp. 263-70, Jul 2002, doi: 10.1007/s00429-002-0241-1.

[76] D. D'Souza and K. Patel, "Involvement of long- and short-range signalling during early tendon development," (in eng), *Anat Embryol (Berl),* vol. 200, no. 4, pp. 367-75, Oct 1999.

[77] S. P. Magnusson, H. Langberg, and M. Kjaer, "The pathogenesis of tendinopathy: balancing the response to loading," in *Nat Rev Rheumatol*, vol. 6, no. 5). United States, 2010, pp. 262-8.

[78] W. R. Thompson, A. Scott, M. T. Loghmani, S. R. Ward, and S. J. Warden, "Understanding Mechanobiology: Physical Therapists as a Force in Mechanotherapy and Musculoskeletal Regenerative Rehabilitation," (in eng), *Phys Ther,* vol. 96, no. 4, pp. 560-9, Apr 2016, doi: 10.2522/ptj.20150224.

[79] C. J. Davidson, L. R. Ganion, G. M. Gehlsen, B. Verhoestra, J. E. Roepke, and T. L. Sevier, "Rat tendon morphologic and functional changes resulting from soft tissue mobilization," (in eng), *Med Sci Sports Exerc,* vol. 29, no. 3, pp. 313-9, Mar 1997.

[80] K. Nagasawa, M. Noguchi, K. Ikoma, and T. Kubo, "Static and dynamic biomechanical properties of the regenerating rabbit Achilles tendon," (in eng), *Clin Biomech (Bristol, Avon),* vol. 23, no. 6, pp. 832-8, Jul 2008, doi: 10.1016/j.clinbiomech.2008.02.002.

[81] M. S. Gareth H. Spurlock Dvm, S. L. Spurlock, and G. A. Parker, *Ultrasonographic, gross, and histologic evaluation of a tendinitis disease model in the horse*. 2005, pp. 184-188.

[82] J. E. Carpenter, S. Thomopoulos, C. L. Flanagan, C. M. DeBano, and L. J. Soslowsky, "Rotator cuff defect healing: a biomechanical and histologic analysis in an animal model," (in eng), *J Shoulder Elbow Surg,* vol. 7, no. 6, pp. 599-605, Nov-Dec 1998.

[83] J. Bruns, J. Kampen, J. Kahrs, and W. Plitz, "Achilles tendon rupture: experimental results on spontaneous repair in a sheep-model," (in eng), *Knee Surg Sports Traumatol Arthrosc,* vol. 8, no. 6, pp. 364-9, 2000, doi: 10.1007/s001670000149.

[84] F. Klatte-Schulz *et al.*, "Different Achilles Tendon Pathologies Show Distinct Histological and Molecular Characteristics," (in eng), *Int J Mol Sci,* vol. 19, no. 2, Jan 30 2018, doi: 10.3390/ijms19020404.

[85] F. Oliva *et al.*, "I.S.Mu.L.T - Rotator Cuff Tears Guidelines," (in eng), *Muscles Ligaments Tendons J,* vol. 5, no. 4, pp. 227-63, Oct-Dec 2015, doi: 10.11138/mltj/2015.5.4.227.

[86] J. Boudreault, F. Desmeules, J. S. Roy, C. Dionne, P. Fremont, and J. C. Macdermid, "The efficacy of oral non-steroidal anti-inflammatory drugs for rotator cuff tendinopathy: a systematic review and meta-analysis," (in eng), *J Rehabil Med,* vol. 46, no. 4, pp. 294-306, Apr 2014, doi: 10.2340/16501977-1800.

[87] R. van der Sande, W. D. Rinkel, L. Gebremariam, E. M. Hay, B. W. Koes, and B. M. Huisstede, "Subacromial impingement syndrome: effectiveness of pharmaceutical interventions-nonsteroidal anti-inflammatory drugs, corticosteroid, or other injections: a systematic review," (in eng), *Arch Phys Med Rehabil,* vol. 94, no. 5, pp. 961-76, May 2013, doi: 10.1016/j.apmr.2012.11.041.

[88] R. H. White, D. M. Paull, and K. W. Fleming, "Rotator cuff tendinitis: comparison of subacromial injection of a long acting corticosteroid versus oral indomethacin therapy," (in eng), *J Rheumatol,* vol. 13, no. 3, pp. 608-13, Jun 1986.

[89] D. W. Rha, G. Y. Park, Y. K. Kim, M. T. Kim, and S. C. Lee, "Comparison of the therapeutic effects of ultrasound-guided platelet-rich plasma injection and dry needling in rotator cuff disease: a randomized controlled trial," (in eng), *Clin Rehabil,* vol. 27, no. 2, pp. 113-22, Feb 2013, doi: 10.1177/0269215512448388.

[90] A. J. Carr *et al.*, "Platelet-Rich Plasma Injection With Arthroscopic Acromioplasty for Chronic Rotator Cuff Tendinopathy: A Randomized Controlled Trial," (in eng), *Am J Sports Med,* vol. 43, no. 12, pp. 2891-7, Dec 2015, doi: 10.1177/0363546515608485.

[91] S. Kesikburun, A. K. Tan, B. Yilmaz, E. Yasar, and K. Yazicioglu, "Platelet-rich plasma injections in the treatment of chronic rotator cuff tendinopathy: a randomized controlled trial with 1-year follow-up," (in eng), *Am J Sports Med,* vol. 41, no. 11, pp. 2609-16, Nov 2013, doi: 10.1177/0363546513496542.

[92] K. Tsikopoulos *et al.*, "The clinical impact of platelet-rich plasma on tendinopathy compared to placebo or dry needling injections: A meta-analysis," (in eng), *Phys Ther Sport,* vol. 17, pp. 87-94, Jan 2016, doi: 10.1016/j.ptsp.2015.06.003.

[93] Y. Shibata, K. Midorikawa, G. Emoto, and M. Naito, "Clinical evaluation of sodium hyaluronate for the treatment of patients with rotator cuff tear," (in eng), *J Shoulder Elbow Surg,* vol. 10, no. 3, pp. 209-16, May-Jun 2001, doi: 10.1067/mse.2001.113501.

[94] C. M. Alvarez, R. Litchfield, D. Jackowski, S. Griffin, and A. Kirkley, "A prospective, double-blind, randomized clinical trial comparing subacromial injection of betamethasone and xylocaine to xylocaine alone in chronic rotator cuff tendinosis," (in eng), *Am J Sports Med,* vol. 33, no. 2, pp. 255-62, Feb 2005, doi: 10.1177/0363546504267345.

[95] S. L. Moran, C. K. Ryan, G. S. Orlando, C. E. Pratt, and K. B. Michalko, "Effects of 5-fluorouracil on flexor tendon repair," (in eng), *J Hand Surg Am,* vol. 25, no. 2, pp. 242-51, Mar 2000, doi: 10.1053/jhsu.2000.jhsu25a0242.

[96] N. Nakamura *et al.*, "Early biological effect of in vivo gene transfer of platelet-derived growth factor (PDGF)-B into healing patellar ligament," (in eng), *Gene Ther,* vol. 5, no. 9, pp. 1165-70, Sep 1998, doi: 10.1038/sj.gt.3300712.

[97] J. Kukkonen *et al.*, "Treatment of non-traumatic rotator cuff tears: A randomised controlled trial with one-year clinical results," (in eng), *Bone Joint J,* vol. 96-b, no. 1, pp. 75-81, Jan 2014, doi: 10.1302/0301-620x.96b1.32168.

[98] P. A. van Dijk, B. Lubberts, C. Verheul, C. W. DiGiovanni, and G. M. Kerkhoffs, "Rehabilitation after surgical treatment of peroneal tendon tears and ruptures," (in eng), *Knee Surg Sports Traumatol Arthrosc,* vol. 24, no. 4, pp. 1165-74, Apr 2016, doi: 10.1007/s00167-015-3944-6.

[99] P. Edwards, J. Ebert, B. Joss, G. Bhabra, T. Ackland, and A. Wang, "Exercise rehabilitation in the non-operative management of rotator cuff tears: a review of the literature," (in eng), *Int J Sports Phys Ther,* vol. 11, no. 2, pp. 279-301, Apr 2016.

[100] C. A. Thigpen, M. A. Shaffer, B. W. Gaunt, B. G. Leggin, G. R. Williams, and R. B. Wilcox, 3rd, "The American Society of Shoulder and Elbow Therapists' consensus statement on rehabilitation following arthroscopic rotator cuff repair," (in eng), *J Shoulder Elbow Surg,* vol. 25, no. 4, pp. 521-35, Apr 2016, doi: 10.1016/j.jse.2015.12.018.

[101] O. A. van der Meijden, P. Westgard, Z. Chandler, T. R. Gaskill, D. Kokmeyer, and P. J. Millett, "Rehabilitation after arthroscopic rotator cuff repair: current concepts review and evidence-based guidelines," (in eng), *Int J Sports Phys Ther,* vol. 7, no. 2, pp. 197-218, Apr 2012.

[102] L. J. Weiss, D. Wang, M. Hendel, P. Buzzerio, and S. A. Rodeo, "Management of Rotator Cuff Injuries in the Elite Athlete," (in eng), *Curr Rev Musculoskelet Med,* vol. 11, no. 1, pp. 102-112, Mar 2018, doi: 10.1007/s12178-018-9464-5.

[103] J. N. Liu *et al.*, "Treatment of Partial Thickness Rotator Cuff Tears in Overhead Athletes," (in eng), *Curr Rev Musculoskelet Med,* vol. 11, no. 1, pp. 55-62, Mar 2018, doi: 10.1007/s12178-018-9459-2.

[104] K. S. Ahn, N. J. Lee, C. H. Kang, Y. H. Lee, and H. J. Jeon, "Serial Changes of Tendon Histomorphology and Strain Elastography After Induced Achilles Tendinopathy in Rabbits: An In Vivo Study," (in eng), *J Ultrasound Med,* vol. 36, no. 4, pp. 767-774, Apr 2017, doi: 10.7863/ultra.16.02059.

[105] T. A. Sgroi and M. Cilenti, "Rotator cuff repair: post-operative rehabilitation concepts," (in eng), *Curr Rev Musculoskelet Med,* vol. 11, no. 1, pp. 86-91, Mar 2018, doi: 10.1007/s12178-018-9462-7.

[106] B. G. Lee, N. S. Cho, and Y. G. Rhee, "Effect of two rehabilitation protocols on range of motion and healing rates after arthroscopic rotator cuff repair: aggressive versus limited early passive exercises," (in eng), *Arthroscopy,* vol. 28, no. 1, pp. 34-42, Jan 2012, doi: 10.1016/j.arthro.2011.07.012.

[107] D. J. Cuff and D. R. Pupello, "Prospective randomized study of arthroscopic rotator cuff repair using an early versus delayed postoperative physical therapy protocol," (in eng), *J Shoulder Elbow Surg,* vol. 21, no. 11, pp. 1450-5, Nov 2012, doi: 10.1016/j.jse.2012.01.025.

[108] K. H. Koh, T. K. Lim, M. S. Shon, Y. E. Park, S. W. Lee, and J. C. Yoo, "Effect of immobilization without passive exercise after rotator cuff repair: randomized clinical trial comparing four and eight weeks of immobilization," (in eng), *J Bone Joint Surg Am,* vol. 96, no. 6, p. e44, Mar 19 2014, doi: 10.2106/jbjs.l.01741.

[109] A. J. Carr *et al.*, "Clinical effectiveness and cost-effectiveness of open and arthroscopic rotator cuff repair [the UK Rotator Cuff Surgery (UKUFF) randomised trial]," (in eng), *Health Technol Assess,* vol. 19, no. 80, pp. 1-218, Oct 2015, doi: 10.3310/hta19800.

[110] J. A. Greenspoon, M. Petri, R. J. Warth, and P. J. Millett, "Massive rotator cuff tears: pathomechanics, current treatment options, and clinical outcomes," (in eng), *J Shoulder Elbow Surg,* vol. 24, no. 9, pp. 1493-505, Sep 2015, doi: 10.1016/j.jse.2015.04.005.

[111] N. Tandon, D. Marolt, E. Cimetta, and G. Vunjak-Novakovic, "Bioreactor engineering of stem cell environments," (in eng), *Biotechnol Adv,* vol. 31, no. 7, pp. 1020-31, Nov 15 2013, doi: 10.1016/j.biotechadv.2013.03.007.

[112] M. Govoni, C. Muscari, J. Lovecchio, C. Guarnieri, and E. Giordano, "Mechanical Actuation Systems for the Phenotype Commitment of Stem Cell-Based Tendon and Ligament Tissue Substitutes," (in eng), *Stem Cell Rev Rep,* vol. 12, no. 2, pp. 189-201, Apr 2016, doi: 10.1007/s12015-015-9640-6.

[113] M. Peroglio, D. Gaspar, D. I. Zeugolis, and M. Alini, "Relevance of bioreactors and whole tissue cultures for the translation of new therapies to humans," (in eng), *J Orthop Res,* vol. 36, no. 1, pp. 10-21, Jan 2018, doi: 10.1002/jor.23655.

[114] J. Mace, A. Wheelton, W. S. Khan, and S. Anand, "The Role of Bioreactors in Ligament and Tendon Tissue Engineering," (in eng), *Curr Stem Cell Res Ther,* vol. 11, no. 1, pp. 35-40, 2016.

[115] P. Sawadkar, D. Player, L. Bozec, and V. Mudera, "The mechanobiology of tendon fibroblasts under static and uniaxial cyclic load in a 3D tissue engineered model mimicking native ECM," (in eng), *J Tissue Eng Regen Med*, Oct 17 2019, doi: 10.1002/term.2975.

[116] A. Sensini *et al.*, "Hierarchical electrospun tendon-ligament bioinspired scaffolds induce changes in fibroblasts morphology under static and dynamic conditions," (in eng), *J Microsc*, Jul 24 2019, doi: 10.1111/jmi.12827.

[117] M. Y. Hsiao *et al.*, "The Effect of the Repression of Oxidative Stress on Tenocyte Differentiation: A Preliminary Study of a Rat Cell Model Using a Novel Differential Tensile Strain Bioreactor," (in eng), *Int J Mol Sci*, vol. 20, no. 14, Jul 12 2019, doi: 10.3390/ijms20143437.

[118] Y. Morita *et al.*, "The optimal mechanical condition in stem cell-to-tenocyte differentiation determined with the homogeneous strain distributions and the cellular orientation control," (in eng), *Biol Open*, vol. 8, no. 5, May 30 2019, doi: 10.1242/bio.039164.

[119] Y. Nakanishi *et al.*, "Histological evaluation of tendon formation using a scaffold-free three-dimensional-bioprinted construct of human dermal fibroblasts under in vitro static tensile culture," (in eng), *Regen Ther*, vol. 11, pp. 47-55, Dec 2019, doi: 10.1016/j.reth.2019.02.002.

[120] G. Talo, D. D'Arrigo, S. Lorenzi, M. Moretti, and A. B. Lovati, "Independent, Controllable Stretch-Perfusion Bioreactor Chambers to Functionalize Cell-Seeded Decellularized Tendons," (in eng), *Ann Biomed Eng*, Apr 8 2019, doi: 10.1007/s10439-019-02257-6.

[121] C. Rinoldi *et al.*, "Tendon Tissue Engineering: Effects of Mechanical and Biochemical Stimulation on Stem Cell Alignment on Cell-Laden Hydrogel Yarns," (in eng), *Adv Healthc Mater*, vol. 8, no. 7, p. e1801218, Apr 2019, doi: 10.1002/adhm.201801218.

[122] A. R. Raveling, S. K. Theodossiou, and N. R. Schiele, "A 3D printed mechanical bioreactor for investigating mechanobiology and soft tissue mechanics," (in eng), *MethodsX*, vol. 5, pp. 924-932, 2018, doi: 10.1016/j.mex.2018.08.001.

[123] K. Mubyana and D. T. Corr, "Cyclic Uniaxial Tensile Strain Enhances the Mechanical Properties of Engineered, Scaffold-Free Tendon Fibers," (in eng), *Tissue Eng Part A*, Aug 3 2018, doi: 10.1089/ten.TEA.2018.0028.

[124] M. T. Raimondi *et al.*, "Development and biological validation of a cyclic stretch culture system for the ex vivo engineering of tendons," (in eng), *Int J Artif Organs*, vol. 41, no. 7, pp. 400-412, Jul 2018, doi: 10.1177/0391398818774496.

[125] B. Engebretson, Z. R. Mussett, and V. I. Sikavitsas, "The effects of varying frequency and duration of mechanical stimulation on a tissue-engineered tendon construct," (in eng), *Connect Tissue Res,* vol. 59, no. 2, pp. 167-177, Mar 2018, doi: 10.1080/03008207.2017.1324431.

[126] S. Testa *et al.*, "Combination of biochemical and mechanical cues for tendon tissue engineering," (in eng), *J Cell Mol Med,* vol. 21, no. 11, pp. 2711-2719, Nov 2017, doi: 10.1111/jcmm.13186.

[127] S. Wu, Y. Wang, P. N. Streubel, and B. Duan, "Living nanofiber yarn-based woven biotextiles for tendon tissue engineering using cell tri-culture and mechanical stimulation," (in eng), *Acta Biomater,* vol. 62, pp. 102-115, Oct 15 2017, doi: 10.1016/j.actbio.2017.08.043.

[128] W. G. Grier, A. S. Moy, and B. A. Harley, "Cyclic tensile strain enhances human mesenchymal stem cell Smad 2/3 activation and tenogenic differentiation in anisotropic collagen-glycosaminoglycan scaffolds," (in eng), *Eur Cell Mater,* vol. 33, pp. 227-239, Mar 20 2017, doi: 10.22203/eCM.v033a17

10.22203/eCM.v033a14.

[129] I. Adekanmbi, N. Zargar, and P. Hulley, "An in vitro scratch tendon tissue injury model: effects of high frequency low magnitude loading," (in eng), *Connect Tissue Res,* vol. 58, no. 2, pp. 162-171, Mar 2017, doi: 10.1080/03008207.2016.1198338.

[130] J. Joo Kim, D. S. Musson, B. G. Matthews, J. Cornish, I. A. Anderson, and V. B. Shim, "Applying Physiologically Relevant Strains to Tenocytes in an In Vitro Cell Device Induces In Vivo Like Behaviors," (in eng), *J Biomech Eng,* vol. 138, no. 12, Dec 1 2016, doi: 10.1115/1.4034031.

[131] C. A. Cook *et al.*, "Characterization of a novel bioreactor system for 3D cellular mechanobiology studies," (in eng), *Biotechnol Bioeng,* vol. 113, no. 8, pp. 1825-37, Aug 2016, doi: 10.1002/bit.25946.

[132] J. Burk, A. Plenge, W. Brehm, S. Heller, B. Pfeiffer, and C. Kasper, "Induction of Tenogenic Differentiation Mediated by Extracellular Tendon Matrix and Short-Term Cyclic Stretching," (in eng), *Stem Cells Int,* vol. 2016, p. 7342379, 2016, doi: 10.1155/2016/7342379.

[133] H. Y. Nam, B. Pingguan-Murphy, A. Amir Abbas, A. Mahmood Merican, and T. Kamarul, "The proliferation and tenogenic differentiation potential of bone marrow-derived mesenchymal stromal cell are influenced by specific uniaxial cyclic tensile loading conditions," (in eng), *Biomech Model Mechanobiol,* vol. 14, no. 3, pp. 649-63, Jun 2015, doi: 10.1007/s10237-014-0628-y.

[134] D. W. Youngstrom, I. Rajpar, D. L. Kaplan, and J. G. Barrett, "A bioreactor system for in vitro tendon differentiation and tendon tissue engineering," (in eng), *J Orthop Res,* vol. 33, no. 6, pp. 911-8, Jun 2015, doi: 10.1002/jor.22848.

[135] T. W. Qin *et al.*, "Effect of mechanical stimulation on bone marrow stromal cell-seeded tendon slice constructs: a potential engineered tendon patch for rotator cuff repair," (in eng), *Biomaterials,* vol. 51, pp. 43-50, May 2015, doi: 10.1016/j.biomaterials.2015.01.070.

[136] E. Huisman, A. Lu, R. G. McCormack, and A. Scott, "Enhanced collagen type I synthesis by human tenocytes subjected to periodic in vitro mechanical stimulation," (in eng), *BMC Musculoskelet Disord,* vol. 15, p. 386, Nov 21 2014, doi: 10.1186/1471-2474-15-386.

[137] F. Qi *et al.*, "From the perspective of embryonic tendon development: various cells applied to tendon tissue engineering," (in eng), *Ann Transl Med,* vol. 8, no. 4, p. 131, Feb 2020, doi: 10.21037/atm.2019.12.78.

[138] T. Wang *et al.*, "In vitro loading models for tendon mechanobiology," (in eng), *J Orthop Res,* vol. 36, no. 2, pp. 566-575, Feb 2018, doi: 10.1002/jor.23752.

[139] G. A. Orozco, P. Tanska, M. E. Mononen, K. S. Halonen, and R. K. Korhonen, "The effect of constitutive representations and structural constituents of ligaments on knee joint mechanics," (in eng), *Sci Rep,* vol. 8, no. 1, p. 2323, Feb 2 2018, doi: 10.1038/s41598-018-20739-w.

[140] L. Chernak Slane and D. G. Thelen, "The use of 2D ultrasound elastography for measuring tendon motion and strain," (in eng), *J Biomech,* vol. 47, no. 3, pp. 750-4, Feb 7 2014, doi: 10.1016/j.jbiomech.2013.11.023.

[141] E. Guanziroli, M. Cazzaniga, L. Colombo, S. Basilico, G. Legnani, and F. Molteni, "Assistive powered exoskeleton for complete spinal cord injury: correlations between walking ability and exoskeleton control," (in eng), *Eur J Phys Rehabil Med,* vol. 55, no. 2, pp. 209-216, Apr 2019, doi: 10.23736/s1973-9087.18.05308-x.

[142] Y. Asano, K. Okada, and M. Inaba, "Design principles of a human mimetic humanoid: Humanoid platform to study human intelligence and internal body system," *Sci Robot,* vol. 2, no. 13, p. eaaq0899, 2017, doi: 10.1126/scirobotics.aaq0899.

[143] Y. Asano, K. Okada, and M. Inaba, "Musculoskeletal design, control, and application of human mimetic humanoid Kenshiro," (in eng), *Bioinspir Biomim,* vol. 14, no. 3, p. 036011, Apr 8 2019, doi: 10.1088/1748-3190/ab03fc.

[144] A. Diamond and O. E. Holland, "Reaching control of a full-torso, modelled musculoskeletal robot using muscle synergies emergent under reinforcement learning," (in eng), *Bioinspir Biomim,* vol. 9, no. 1, p. 016015, Mar 2014, doi: 10.1088/1748-3182/9/1/016015.

[145] C. Richter *et al.*, "Musculoskeletal Robots: Scalability in Neural Control," *IEEE Robot Autom Mag,* vol. 23, no. 4, pp. 128-137, 2016, doi: 10.1109/MRA.2016.2535081.

[146] L. Ricotti and A. Menciassi, "Bio-hybrid muscle cell-based actuators," (in eng), *Biomed Microdevices,* vol. 14, no. 6, pp. 987-98, Dec 2012, doi: 10.1007/s10544-012-9697-9.

[147] S. Shirafuji, S. Ikemoto, and K. Hosoda, "Development of a tendon-driven robotic finger for an anthropomorphic robotic hand," *Int J Robot Res,* vol. 33, no. 5, pp. 677-693, 2019/08/03 2014.

[148] P.-A. Mouthuy, S. Snelling, R. Hostettler, A. Kharchenko, and A. Carr. (2019). Growing human tendon cells on humanoid robots.

[149] O. Khatib, E. Demircan, V. De Sapio, L. Sentis, T. Besier, and S. Delp, "Robotics-based synthesis of human motion," (in eng), *J Physiol Paris,* vol. 103, no. 3-5, pp. 211-9, Sep-Dec 2009, doi: 10.1016/j.jphysparis.2009.08.004.

[150] E. J. Wolf, V. Q. Everding, A. A. Linberg, J. M. Czerniecki, and J. M. Gambel, "Comparison of the Power Knee and C-Leg during step-up and sit-to-stand tasks," (in eng), *Gait Posture,* vol. 38, no. 3, pp. 397-402, Jul 2013, doi: 10.1016/j.gaitpost.2013.01.007.

[151] E. E. Butler, A. L. Ladd, S. A. Louie, L. E. Lamont, W. Wong, and J. Rose, "Three-dimensional kinematics of the upper limb during a Reach and Grasp Cycle for children," (in eng), *Gait Posture,* vol. 32, no. 1, pp. 72-7, May 2010, doi: 10.1016/j.gaitpost.2010.03.011.

[152] L. J. Millar, L. Meng, and P. J. Rowe, "Routine clinical motion analysis: comparison of a bespoke real-time protocol to current clinical methods," (in eng), *Comput Methods Biomech Biomed Engin,* vol. 22, no. 2, pp. 149-158, Feb 2019, doi: 10.1080/10255842.2018.1541089.

[153] J. R. Gage and T. F. Novacheck, "An update on the treatment of gait problems in cerebral palsy," (in eng), *J Pediatr Orthop B,* vol. 10, no. 4, pp. 265-74, Oct 2001.

[154] V. Camomilla, A. Cereatti, A. G. Cutti, S. Fantozzi, R. Stagni, and G. Vannozzi, "Methodological factors affecting joint moments estimation in clinical gait analysis: a systematic review," (in eng), *Biomed Eng Online,* vol. 16, no. 1, p. 106, Aug 18 2017, doi: 10.1186/s12938-017-0396-x.

[155] A. Kontaxis, A. G. Cutti, G. R. Johnson, and H. E. Veeger, "A framework for the definition of standardized protocols for measuring upper-extremity kinematics," (in eng), *Clin Biomech (Bristol, Avon),* vol. 24, no. 3, pp. 246-53, Mar 2009, doi: 10.1016/j.clinbiomech.2008.12.009.

[156] O. Rettig, L. Fradet, P. Kasten, P. Raiss, and S. I. Wolf, "A new kinematic model of the upper extremity based on functional joint parameter determination for shoulder and elbow," (in eng), *Gait Posture,* vol. 30, no. 4, pp. 469-76, Nov 2009, doi: 10.1016/j.gaitpost.2009.07.111.

[157] V. Phadke, J. P. Braman, R. F. LaPrade, and P. M. Ludewig, "Comparison of glenohumeral motion using different rotation sequences," (in eng), *J Biomech,* vol. 44, no. 4, pp. 700-5, Feb 24 2011, doi: 10.1016/j.jbiomech.2010.10.042.

[158] C. A. Thigpen, M. T. Gross, S. G. Karas, W. E. Garrett, and B. Yu, "The repeatability of scapular rotations across three planes of humeral elevation," (in eng), *Res Sports Med,* vol. 13, no. 3, pp. 181-98, Jul-Sep 2005, doi: 10.1080/15438620500222489.

[159] M. El-Gohary and J. McNames, "Shoulder and elbow joint angle tracking with inertial sensors," (in eng), *IEEE Trans Biomed Eng,* vol. 59, no. 9, pp. 2635-41, Sep 2012, doi: 10.1109/tbme.2012.2208750.

[160] A. Vanezis, M. A. Robinson, and N. Darras, "The reliability of the ELEPAP clinical protocol for the 3D kinematic evaluation of upper limb function," (in eng), *Gait Posture,* vol. 41, no. 2, pp. 431-9, Feb 2015, doi: 10.1016/j.gaitpost.2014.11.007.

[161] E. Jaspers *et al.*, "The reliability of upper limb kinematics in children with hemiplegic cerebral palsy," (in eng), *Gait Posture,* vol. 33, no. 4, pp. 568-75, Apr 2011, doi: 10.1016/j.gaitpost.2011.01.011.

[162] E. Pirondini *et al.*, "Evaluation of the effects of the Arm Light Exoskeleton on movement execution and muscle activities: a pilot study on healthy subjects," (in eng), *J Neuroeng Rehabil,* vol. 13, p. 9, Jan 23 2016, doi: 10.1186/s12984-016-0117-x.

[163] B. Lovern, L. A. Stroud, N. A. Ferran, S. L. Evans, R. O. Evans, and C. A. Holt, "Motion analysis of the glenohumeral joint during activities of daily living," (in eng), *Comput Methods Biomech Biomed Engin,* vol. 13, no. 6, pp. 803-9, Dec 2010, doi: 10.1080/10255841003630637.

[164] J. R. Davids, L. C. Peace, L. V. Wagner, M. A. Gidewall, D. W. Blackhurst, and W. M. Roberson, "Validation of the Shriners Hospital for Children Upper Extremity Evaluation (SHUEE) for children with hemiplegic cerebral palsy," (in eng), *J Bone Joint Surg Am,* vol. 88, no. 2, pp. 326-33, Feb 2006, doi: 10.2106/jbjs.e.00298.

[165] E. Jaspers, K. Desloovere, H. Bruyninckx, G. Molenaers, K. Klingels, and H. Feys, "Review of quantitative measurements of upper limb movements in hemiplegic cerebral palsy," (in eng), *Gait Posture,* vol. 30, no. 4, pp. 395-404, Nov 2009, doi: 10.1016/j.gaitpost.2009.07.110.

[166] R. Krishnan, N. Björsell, E. M. Gutierrez-Farewik, and C. Smith, "A survey of human shoulder functional kinematic representations," (in eng), *Med Biol Eng Comput,* vol. 57, no. 2, pp. 339-367, Feb 2019, doi: 10.1007/s11517-018-1903-3.

[167] S. L. Colyer, M. Evans, D. P. Cosker, and A. I. T. Salo, "A Review of the Evolution of Vision-Based Motion Analysis and the Integration of Advanced Computer Vision Methods Towards Developing a Markerless System," (in eng), *Sports Med Open,* vol. 4, no. 1, p. 24, Jun 5 2018, doi: 10.1186/s40798-018-0139-y.

[168] A. G. Cutti, I. Parel, and A. Kotanxis, "Upper Extremity Models for Clinical Movement Analysis," in *Handbook of Human Motion*, B. Müller *et al.* Eds. Cham: Springer International Publishing, 2017, pp. 1-24.

[169] G. Wu *et al.*, "ISB recommendation on definitions of joint coordinate systems of various joints for the reporting of human joint motion--Part II: shoulder, elbow, wrist and hand," (in eng), *J Biomech,* vol. 38, no. 5, pp. 981-992, May 2005.

[170] C. Anglin and U. P. Wyss, "Review of arm motion analyses," (in eng), *Proc Inst Mech Eng H,* vol. 214, no. 5, pp. 541-55, 2000, doi: 10.1243/0954411001535570.

[171] H. O. Amadi and A. M. Bull, "A motion-decomposition approach to address gimbal lock in the 3-cylinder open chain mechanism description of a joint coordinate system at the glenohumeral joint," (in eng), *J Biomech,* vol. 43, no. 16, pp. 3232-6, Dec 1 2010, doi: 10.1016/j.jbiomech.2010.07.034.

[172] C. Maiwald, A. Arndt, C. Nester, R. Jones, A. Lundberg, and P. Wolf, "The effect of intracortical bone pin application on kinetics and tibiocalcaneal kinematics of walking gait," (in eng), *Gait Posture,* vol. 52, pp. 129-134, Feb 2017, doi: 10.1016/j.gaitpost.2016.10.023.

[173] M. Hajizadeh, B. Michaud, and M. Begon, "The effect of intracortical bone pin on shoulder kinematics during dynamic activities," *Int Biomech,* vol. 6, no. 1, pp. 47-53, 2019/01/01 2019, doi: 10.1080/23335432.2019.1633958.

[174] R. Pérez *et al.*, "Upper limb portable motion analysis system based on inertial technology for neurorehabilitation purposes," (in eng), *Sensors (Basel),* vol. 10, no. 12, pp. 10733-51, 2010, doi: 10.3390/s101210733.

[175] C. Cortés *et al.*, "Inverse Kinematics for Upper Limb Compound Movement Estimation in Exoskeleton-Assisted Rehabilitation," (in eng), *Biomed Res Int*, vol. 2016, p. 2581924, 2016, doi: 10.1155/2016/2581924.

[176] H. Zhou and H. Hu, "Human motion tracking for rehabilitation—A survey," *Biomed Signal Process Control*, vol. 3, no. 1, pp. 1-18, 2008/01/01/ 2008, doi: https://doi.org/10.1016/j.bspc.2007.09.001.

[177] G. Rau, C. Disselhorst-Klug, and R. Schmidt, "Movement biomechanics goes upwards: from the leg to the arm," (in eng), *J Biomech*, vol. 33, no. 10, pp. 1207-16, Oct 2000.

[178] S. Williams, R. Schmidt, C. Disselhorst-Klug, and G. Rau, "An upper body model for the kinematical analysis of the joint chain of the human arm," (in eng), *J Biomech*, vol. 39, no. 13, pp. 2419-29, 2006, doi: 10.1016/j.jbiomech.2005.07.023.

[179] P. Favre, J. G. Snedeker, and C. Gerber, "Numerical modelling of the shoulder for clinical applications," (in eng), *Philos Trans A Math Phys Eng Sci*, vol. 367, no. 1895, pp. 2095-118, May 28 2009, doi: 10.1098/rsta.2008.0282.

[180] B. Bolsterlee, D. H. Veeger, and E. K. Chadwick, "Clinical applications of musculoskeletal modelling for the shoulder and upper limb," (in eng), *Med Biol Eng Comput*, vol. 51, no. 9, pp. 953-63, Sep 2013, doi: 10.1007/s11517-013-1099-5.

[181] A. Erdemir, S. McLean, W. Herzog, and A. J. van den Bogert, "Model-based estimation of muscle forces exerted during movements," (in eng), *Clin Biomech (Bristol, Avon)*, vol. 22, no. 2, pp. 131-54, Feb 2007, doi: 10.1016/j.clinbiomech.2006.09.005.

[182] A. Technology, "Scapulothoracic Rhytm Affects Glenohumeral Joint Force," ed, 2019, p. https://www.youtube.com/watch?v=8uUt0qehShM.

[183] A. F. Huxley and R. Niedergerke, "Structural changes in muscle during contraction; interference microscopy of living muscle fibres," (in eng), *Nature*, vol. 173, no. 4412, pp. 971-3, May 22 1954, doi: 10.1038/173971a0.

[184] A. Hill, "The heat of shortening and the dynamic constants of muscle," *Proc R Soc London B*, vol. 126, no. 843, pp. 136-195, 1938.

[185] A. AnyBody Technology. "AnyTutorials." AnyBody Technology. (accessed July 30, 2020).

[186] K. R. Saul *et al.*, "Benchmarking of dynamic simulation predictions in two software platforms using an upper limb musculoskeletal model," (in eng), *Comput Methods Biomech Biomed Engin,* vol. 18, no. 13, pp. 1445-58, 2015, doi: 10.1080/10255842.2014.916698.

[187] U. Trinler, H. Schwameder, R. Baker, and N. Alexander, "Muscle force estimation in clinical gait analysis using AnyBody and OpenSim," (in eng), *J Biomech,* vol. 86, pp. 55-63, Mar 27 2019, doi: 10.1016/j.jbiomech.2019.01.045.

[188] Y. Kim, J. Yihwan, C. Woosung, L. Kunwoo, and K. Seungbum, "Similarities and differences between musculoskeletal simulations of OpenSim and AnyBody modeling system," *J Mech Sci Tech,* vol. 32, pp. 6037-6044, 12/01 2018, doi: 10.1007/s12206-018-1154-0.

[189] M. de Zee, L. Hansen, C. Wong, J. Rasmussen, and E. B. Simonsen, "A generic detailed rigid-body lumbar spine model," (in eng), *J Biomech,* vol. 40, no. 6, pp. 1219-27, 2007, doi: 10.1016/j.jbiomech.2006.05.030.

[190] F. C. van der Helm, "A finite element musculoskeletal model of the shoulder mechanism," (in eng), *J Biomech,* vol. 27, no. 5, pp. 551-69, May 1994, doi: 10.1016/0021-9290(94)90065-5.

[191] A. A. Nikooyan, H. E. Veeger, E. K. Chadwick, M. Praagman, and F. C. Helm, "Development of a comprehensive musculoskeletal model of the shoulder and elbow," (in eng), *Med Biol Eng Comput,* vol. 49, no. 12, pp. 1425-35, Dec 2011, doi: 10.1007/s11517-011-0839-7.

[192] M. Aurbach, J. Spicka, F. Süß, and S. Dendorfer, "Evaluation of musculoskeletal modelling parameters of the shoulder complex during humeral abduction above 90°," (in eng), *J Biomech,* vol. 106, p. 109817, Jun 9 2020, doi: 10.1016/j.jbiomech.2020.109817.

[193] L. R. Chang, P. Anand, and M. Varacallo, "Anatomy, Shoulder and Upper Limb, Glenohumeral Joint," in *StatPearls*. Treasure Island (FL): StatPearls Publishing, 2020.

[194] M. L. Ruspi, M. Palanca, C. Faldini, and L. Cristofolini, "Full-field in vitro investigation of hard and soft tissue strain in the spine by means of Digital Image Correlation," (in eng), *Muscles Ligaments Tendons J,* vol. 7, no. 4, pp. 538-545, Oct-Dec 2017, doi: 10.11138/mltj/2017.7.4.538.

[195] N. McCormick and J. Lord, "Digital Image Correlation," (in eng), *Mater Today,* vol. 13, no. 12, pp. 52-54, 2010, doi: 10.1016/S1369-7021(10)70235-2.

[196] C. C. Wang, N. O. Chahine, C. T. Hung, and G. A. Ateshian, "Optical determination of anisotropic material properties of bovine articular cartilage in compression," (in eng), *J Biomech,* vol. 36, no. 3, pp. 339-53, Mar 2003, doi: 10.1016/s0021-9290(02)00417-7.

[197] P. Sztefek, M. Vanleene, R. Olsson, R. Collinson, A. A. Pitsillides, and S. Shefelbine, "Using digital image correlation to determine bone surface strains during loading and after adaptation of the mouse tibia," (in eng), *J Biomech,* vol. 43, no. 4, pp. 599-605, Mar 3 2010, doi: 10.1016/j.jbiomech.2009.10.042.

[198] T. Luyckx, M. Verstraete, K. De Roo, W. De Waele, J. Bellemans, and J. Victor, "Digital image correlation as a tool for three-dimensional strain analysis in human tendon tissue," (in eng), *J Exp Orthop,* vol. 1, no. 1, p. 7, Dec 2014, doi: 10.1186/s40634-014-0007-8.

[199] G. Okotie, S. Duenwald-Kuehl, H. Kobayashi, M. J. Wu, and R. Vanderby, "Tendon strain measurements with dynamic ultrasound images: evaluation of digital image correlation," (in eng), *J Biomech Eng,* vol. 134, no. 2, p. 024504, Feb 2012, doi: 10.1115/1.4006116.

[200] M. Palanca, G. Tozzi, and L. Cristofolini, "The use of digital image correlation in the biomechanical area: a review," *Int Biomech,* vol. 3, no. 1, pp. 1-21, 2016/01/01 2016, doi: 10.1080/23335432.2015.1117395.

[201] D. Dynamics, "ISTRA 4D Software Manual Q-400 System," 2018.

[202] Vicon. "Plug-in Gait Reference Guide." Vicon. https://docs.vicon.com/display/Nexus29/Kinetic+modeling (accessed July, 2020).

[203] C. McCausland, E. Sawyer, B. J. Eovaldi, and M. Varacallo, "Anatomy, Shoulder and Upper Limb, Shoulder Muscles," in *StatPearls*. Treasure Island (FL): StatPearls Publishing

Copyright © 2020, StatPearls Publishing LLC., 2020.

[204] L. Weiss, D. Wang, M. Hendel, P. Buzzerio, and S. Rodeo, "Management of Rotator Cuff Injuries in the Elite Athlete," (in eng), *Current Reviews in Musculoskeletal Medicine,* vol. 11, no. 1, pp. 102-112, 2018, doi: 10.1007/s12178-018-9464-5.

[205] C. J. Durall, J. W. Matheson, J. D. Placzek, and D. A. Boyce, "Chapter 34 - Isokinetic Testing and Exercise," in *Orthopaedic Physical Therapy Secrets (Third Edition)*: Elsevier, 2017, pp. 283-292.

[206] T. S. Ellenbecker and G. J. Davies, "The application of isokinetics in testing and rehabilitation of the shoulder complex," (in eng), *J Athl Train,* vol. 35, no. 3, pp. 338-50, Jul 2000.

[207] G. E. Gorton, 3rd, D. A. Hebert, and M. E. Gannotti, "Assessment of the kinematic variability among 12 motion analysis laboratories," (in eng), *Gait Posture,* vol. 29, no. 3, pp. 398-402, Apr 2009, doi: 10.1016/j.gaitpost.2008.10.060.

[208] M. P. Kadaba, H. K. Ramakrishnan, M. E. Wootten, J. Gainey, G. Gorton, and G. V. Cochran, "Repeatability of kinematic, kinetic, and electromyographic data in normal adult gait," (in eng), *J Orthop Res,* vol. 7, no. 6, pp. 849-60, 1989, doi: 10.1002/jor.1100070611.

[209] G. Rab, K. Petuskey, and A. Bagley, "A method for determination of upper extremity kinematics," (in eng), *Gait Posture,* vol. 15, no. 2, pp. 113-9, Apr 2002, doi: 10.1016/s0966-6362(01)00155-2.

[210] Vicon. "Vicon Nexus Reference Guide." Vicon. https://docs.vicon.com/display/Nexus29/Vicon+Nexus+Reference+Guide (accessed August, 2020).

[211] P. F. Vint and R. N. Hinrichs, "Endpoint error in smoothing and differentiating raw kinematic data: An evaluation of four popular methods," *J Biomech,* vol. 29, no. 12, pp. 1637-1642, 1996, doi: https://doi.org/10.1016/S0021-9290(96)80018-2.

[212] D. Winter, "Anthropometry," *Biomechanics and Motor Control of Human Movement,* pp. 82-106, 2009/09/23 2009, doi: 10.1002/9780470549148.ch4.

[213] M. Damsgaard, J. Rasmussen, S. T. Christensen, E. Surma, and M. de Zee, "Analysis of musculoskeletal systems in the AnyBody Modeling System," *Simul Model Pract Th,* vol. 14, no. 8, pp. 1100-1111, 2006/11/01/ 2006, doi: https://doi.org/10.1016/j.simpat.2006.09.001.

[214] M. S. Andersen, M. Damsgaard, B. MacWilliams, and J. Rasmussen, "A computationally efficient optimisation-based method for parameter identification of kinematically determinate and over-determinate biomechanical systems," (in eng), *Comput Methods Biomech Biomed Engin,* vol. 13, no. 2, pp. 171-83, 2010, doi: 10.1080/10255840903067080.

[215] M. E. Lund, M. S. Andersen, M. de Zee, and J. Rasmussen, "Scaling of musculoskeletal models from static and dynamic trials," *Int Biomech,* vol. 2, no. 1, pp. 1-11, 2015/01/01 2015, doi: 10.1080/23335432.2014.993706.

[216] M. E. Lund, M. de Zee, M. S. Andersen, and J. Rasmussen, "On validation of multibody musculoskeletal models," (in eng), *Proc Inst Mech Eng H,* vol. 226, no. 2, pp. 82-94, Feb 2012, doi: 10.1177/0954411911431516.

[217] P.-A. Mouthuy, N. Baboldashti, A. Carr, and O. Hakimi, "Scaffold," United States Patent 20200155724 Patent Appl. 16/688,676, 2020.

[218] R. Winters, A. Winters, and R. G. Amedee, "Statistics: a brief overview," (in eng), *Ochsner J,* vol. 10, no. 3, pp. 213-6, Fall 2010.

[219] F. S. Nahm, "Nonparametric statistical tests for the continuous data: the basic concept and the practical use," (in eng), *Korean J Anesthesiol,* vol. 69, no. 1, pp. 8-14, Feb 2016, doi: 10.4097/kjae.2016.69.1.8.

[220] R. B. D'Agostino and A. Belanger, "A Suggestion for Using Powerful and Informative Tests of Normality," *Am Stat,* vol. 44, no. 4, pp. 316-321, 1990/11/01 1990, doi: 10.1080/00031305.1990.10475751.

[221] S. S. S. and M. B. Wilk, "An analysis of variance test for normality (complete samples)†," *Biometrika,* vol. 52, no. 3-4, pp. 591-611, 1965, doi: 10.1093/biomet/52.3-4.591.

[222] S. Shirafuji, S. Ikemoto, and K. Hosoda, "Development of a tendon-driven robotic finger for an anthropomorphic robotic hand," *The International Journal of Robotics Research,* vol. 33, no. 5, pp. 677-693, 2019/08/03 2014.

[223] P. Gulde and J. Hermsdörfer, "Smoothness Metrics in Complex Movement Tasks," (in eng), *Front Neurol,* vol. 9, p. 615, 2018, doi: 10.3389/fneur.2018.00615.

[224] S. Balasubramanian, A. Melendez-Calderon, A. Roby-Brami, and E. Burdet, "On the analysis of movement smoothness," (in eng), *J Neuroeng Rehabil,* vol. 12, p. 112, Dec 9 2015, doi: 10.1186/s12984-015-0090-9.

[225] T. Asakura, Y. Miyazawa, and S. Usuda, "The validity of an accelerometer-based method for estimating fluidity in the sit-to-walk task in a community setting," (in eng), *J Phys Ther Sci,* vol. 29, no. 1, pp. 133-137, Jan 2017, doi: 10.1589/jpts.29.133.

[226] C. L. A. Gomes *et al.*, "Low-cost equipment for the evaluation of reach and grasp in post-stroke individuals: a pilot study," (in eng), *Biomed Eng Online,* vol. 19, no. 1, p. 14, Mar 4 2020, doi: 10.1186/s12938-020-0758-7.

[227] N. Hesam-Shariati, T. Trinh, A. G. Thompson-Butel, C. T. Shiner, S. J. Redmond, and P. A. McNulty, "Improved Kinematics and Motor Control in a Longitudinal Study of a Complex Therapy Movement in Chronic Stroke," (in eng), *IEEE Trans Neural Syst Rehabil Eng,* vol. 27, no. 4, pp. 682-691, Apr 2019, doi: 10.1109/tnsre.2019.2895018.

[228] M. Walker, J. Brooks, M. Willis, and M. Frankle, "How reverse shoulder arthroplasty works," (in eng), *Clin Orthop Relat Res,* vol. 469, no. 9, pp. 2440-51, Sep 2011, doi: 10.1007/s11999-011-1892-0.

[229] R. Drillis, R. Contini, and M. Bluestein, "Body segment parameters; A survey of measurement techniques," (in eng), *Artif Limbs,* vol. 8, pp. 44-66, 1964.

[230] K. S. Saladin, *Anatomy & physiology : the unity of form and function*, Sixth edition, [International students ed. (Anatomy and physiology : the unity of form and function). New York: McGraw-Hill (in eng), 2012.

[231] J. T. Hansen, F. H. Netter, and C. A. G. Machado, *Netter's clinical anatomy*, 4th ed. (Netter basic science). Philadelphia, PA: Elsevier (in eng), 2019.

[232] J. S. Scibek and C. R. Carcia, "Assessment of scapulohumeral rhythm for scapular plane shoulder elevation using a modified digital inclinometer," (in eng), *World J Orthop,* vol. 3, no. 6, pp. 87-94, Jun 18 2012, doi: 10.5312/wjo.v3.i6.87.

[233] G. N. Drake, D. P. O'Connor, and T. B. Edwards, "Indications for reverse total shoulder arthroplasty in rotator cuff disease," (in eng), *Clin Orthop Relat Res,* vol. 468, no. 6, pp. 1526-33, Jun 2010, doi: 10.1007/s11999-009-1188-9.

[234] W. R. Dunn *et al.*, "Symptoms of pain do not correlate with rotator cuff tear severity: a cross-sectional study of 393 patients with a symptomatic atraumatic full-thickness rotator cuff tear," (in eng), *J Bone Joint Surg Am,* vol. 96, no. 10, pp. 793-800, May 21 2014, doi: 10.2106/jbjs.l.01304.

[235] C. Anglin, U. P. Wyss, and D. R. Pichora, "Mechanical testing of shoulder prostheses and recommendations for glenoid design," (in eng), *J Shoulder Elbow Surg,* vol. 9, no. 4, pp. 323-31, Jul-Aug 2000, doi: 10.1067/mse.2000.105451.

[236] C. P. Roche *et al.*, "Analysis of Glenoid Fixation with Anatomic Total Shoulder Arthroplasty in an Extreme Cyclic Loading Scenario," (in eng), *Bull Hosp Jt Dis (2013),* vol. 73 Suppl 1, pp. S57-62, Dec 2015.

[237] S. Ikemoto, Y. Kimoto, and K. Hosoda, "Shoulder complex linkage mechanism for humanlike musculoskeletal robot arms," (in eng), *Bioinspir Biomim,* vol. 10, no. 6, p. 066009, Nov 5 2015, doi: 10.1088/1748-3190/10/6/066009.

[238] C. Wu *et al.*, "Botulinum toxin type A with or without needle electromyographic guidance in patients with cervical dystonia," (in eng), *Springerplus,* vol. 5, no. 1, p. 1292, 2016, doi: 10.1186/s40064-016-2967-x.

[239] M. M. Reinold *et al.*, "Electromyographic analysis of the rotator cuff and deltoid musculature during common shoulder external rotation exercises," (in eng), *J Orthop Sports Phys Ther,* vol. 34, no. 7, pp. 385-94, Jul 2004, doi: 10.2519/jospt.2004.34.7.385.

[240] R. E. Hughes and K. N. An, "Force analysis of rotator cuff muscles," (in eng), *Clin Orthop Relat Res,* no. 330, pp. 75-83, Sep 1996, doi: 10.1097/00003086-199609000-00010.

[241] N. Wuelker, W. Plitz, B. Roetman, and C. J. Wirth, "Function of the supraspinatus muscle. Abduction of the humerus studied in cadavers," (in eng), *Acta Orthop Scand,* vol. 65, no. 4, pp. 442-6, Aug 1994, doi: 10.3109/17453679408995490.

[242] Y. Blache, M. Begon, B. Michaud, L. Desmoulins, P. Allard, and F. Dal Maso, "Muscle function in glenohumeral joint stability during lifting task," (in eng), *PLoS One,* vol. 12, no. 12, p. e0189406, 2017, doi: 10.1371/journal.pone.0189406.

[243] C. Engelhardt *et al.*, "Comparison of an EMG-based and a stress-based method to predict shoulder muscle forces," (in eng), *Comput Methods Biomech Biomed Engin,* vol. 18, no. 12, pp. 1272-9, 2015, doi: 10.1080/10255842.2014.899587.

[244] C. Flores-Hernandez, I. Eskinazi, H. R. Hoenecke, and D. D. D'Lima, "Scapulothoracic rhythm affects glenohumeral joint force," (in eng), *JSES Open Access,* vol. 3, no. 2, pp. 77-82, Jul 2019, doi: 10.1016/j.jses.2019.03.004.

[245] Y. Blache and M. Begon, "Influence of Shoulder Kinematic Estimate on Joint and Muscle Mechanics Predicted by Musculoskeletal Model," (in eng), *IEEE Trans Biomed Eng,* vol. 65, no. 4, pp. 715-722, Apr 2018, doi: 10.1109/tbme.2017.2716186.

[246] F. Saadat, A. C. Deymier, V. Birman, S. Thomopoulos, and G. M. Genin, "The concentration of stress at the rotator cuff tendon-to-bone attachment site is conserved across species," (in eng), *J Mech Behav Biomed Mater,* vol. 62, pp. 24-32, Sep 2016, doi: 10.1016/j.jmbbm.2016.04.025.

[247] G. McClanahan, "Measurement precision and reliability of supraspinatus tendon strain using speckle track analysis of ultrasound images," M.Sc., Biomechanics, School of Kinesiology, Marshall University, Huntington, West Virginia, USA, 2019.

[248] G. Tozzi, M. Peña Fernández, S. Davis, A. Karali, A. P. Kao, and G. Blunn, "Full-Field Strain Uncertainties and Residuals at the Cartilage-Bone Interface in Unstained Tissues Using Propagation-Based Phase-Contrast XCT and Digital Volume Correlation," (in eng), *Materials (Basel),* vol. 13, no. 11, Jun 5 2020, doi: 10.3390/ma13112579.

[249] C. J. Gatti, C. R. Dickerson, E. K. Chadwick, A. G. Mell, and R. E. Hughes, "Comparison of model-predicted and measured moment arms for the rotator cuff muscles," (in eng), *Clin Biomech (Bristol, Avon),* vol. 22, no. 6, pp. 639-44, Jul 2007, doi: 10.1016/j.clinbiomech.2007.02.001.

[250] F. Hug, "Can muscle coordination be precisely studied by surface electromyography?," (in eng), *J Electromyogr Kinesiol,* vol. 21, no. 1, pp. 1-12, Feb 2011, doi: 10.1016/j.jelekin.2010.08.009.

[251] G. Bergmann *et al.*, "In vivo gleno-humeral joint loads during forward flexion and abduction," (in eng), *J Biomech,* vol. 44, no. 8, pp. 1543-52, May 17 2011, doi: 10.1016/j.jbiomech.2011.02.142.

[252] B. Juul-Kristensen *et al.*, "Muscle sizes and moment arms of rotator cuff muscles determined by magnetic resonance imaging," (in eng), *Cells Tissues Organs*, vol. 167, no. 2-3, pp. 214-22, 2000, doi: 10.1159/000016784.

Abbreviations Used in Text

AAROM: assisted active range of motion
AC: acromioclavicular
ADL: activity of daily living
AMMR: AnyBody Managed Model Repository
AMS: AnyBody™ Modeling System
ASCs: adipose derived mesenchymal stem cells
ATP: adenosine triphosphate
CAD: computer assisted design software
COX-2: cyclooxygenase
CP: Cerebral Palsy
DIC: Digital Image Correlation
DMEM: Dulbecco's modified eagle medium
DoF: degrees of freedom
DSEM: Delft Shoulder and Elbow Model
ECM: extracellular matrix
EMG: electromyography
ESCs: embryonic stem cells
FEA: finite element analysis
FPGA: field programmable gate array
GAG: glycosaminoglycans
GH: glenohumeral
hBMSCs: human bone marrow mesenchymal stem cells
HDF: human dermal fibroblasts
JCS: joint coordinate system
MA: motion analysis
MMP: matrix metalloproteinase
MSK: musculoskeletal
NSAIDs: non-steroidal anti-inflammatory drugs
PDGFβ: platelet derived growth factor
PID proportional-integral-derivative
PiG: Plug-in Gait®
PLLA: polylactic acid
PROM: passive range of motion
PRP: platelet-rich plasma
ROM: range of motion
ROS: reactive oxygen species
SC: sternoclavicular
SD: standard deviation
SEM: standard error of the mean
SPI: serial peripheral interface
ST: scapulothoracic
STA: soft tissue artefact
UE: upper extremity
USA: United States of America
VEGF: vascular endothelial growth factor

Appendix A. Code for Kinematic UE Modelling

Static Code for Human Participants

```
{*---------------------------------- START OF MACRO SECTION ----------------------
------------------*}

macro DRAWBONE(Bone,BoneLabel)
{*Outputs segment definition markers in Polygon format*}
LL = Bone#Size
DD = LL/10
WW = DD
BoneLabel#O = 0(Bone)+LL*Bone#Shift*Attitude(Bone)
BoneLabel#P = BoneLabel#O+LL*2(Bone#Scale)*2(Bone)
BoneLabel#A = BoneLabel#O+DD*3(Bone#Scale)*3(Bone)
BoneLabel#L = BoneLabel#O+WW*1(Bone#Scale)*1(Bone)
OUTPUT(BoneLabel#O,BoneLabel#P,BoneLabel#A,BoneLabel#L)
endmacro

{*---------------------------------- CREATE VIRTUAL MARKERS ----------------------
------------------*}

{* Define the segment that was used to calculate the position vector of the missing
marker *}

       ThoraxCluster=[CHEA,CHEA-CHEC,CHEB-CHEA,yzx]

{* The position vector %V1 is read in from the parameter file *}

%V1 = {$%STRNLocalx,$%STRNLocaly,$%STRNLocalz}
%V2 = {$%T10Localx,$%T10Localy,$%T10Localz}
%V3 = {$%C7Localx,$%C7Localy,$%C7Localz}

{* Recreate the missing marker using the postion vector *}

STRN = (CHEA/ThoraxCluster + %V1)*ThoraxCluster
T10 = (CHEA/ThoraxCluster + %V2)*ThoraxCluster
C7 = (CHEA/ThoraxCluster + %V3)*ThoraxCluster

{* Output the trajectory of the missing marker to the C3D file *}

OUTPUT(STRN)
OUTPUT(T10)
OUTPUT(C7)

{* ----------------------------------Calculate position of ELM marker--------------
---------------- *}

{* Calculate the position vector of the medial elbow marker (ELM) relative to the
local reference
frame of the upper arm Clusters and lateral elbow marker (ELL)*}

{* Cluster markers are called UPA, UPB, UPC, UPD *}

       RightArm=[RUPA,RUPA-RUPB,RUPA-RELL,yzx]

$%RELM = RELM/RightArm

{* $%RELM are converted into its three orthogonal coordinates
- this format is needed to save as a parameter in the MP file *}

$%RELMLocalx = $%RELM(1)
$%RELMLocaly = $%RELM(2)
$%RELMLocalz = $%RELM(3)

{* $%LELM and $%RELM is written to the mp file *}

PARAM($%RELMLocalx,$%RELMLocaly,$%RELMLocalz)

{*---------------------------------------------------------------------------------
------------------*}
```

```
{*-------------------------------------- DEFINE SEGMENTS -------------------------
------------------*}

{* Global reference frame at origin *}

Gorigin = {0,0,0}
Global = [Gorigin,{0,0,1},{0,-1,0},yxz]
{*
GlobalSize = 100
GlobalScale = {3,4,5}
GlobalShift = {0,0,0}
DrawBone(Global, GLO)
*}

{*=====Thorax segment=====*}

IF EXISTATALL(CLAV)
{* Run after creating the virtual markers STRN & T10 *}

UThorax = (C7+CLAV)/2
LThorax = (T10+STRN)/2
ThoraxCentre = LThorax
Thorax = [LThorax,UThorax-LThorax,T10-STRN,yxz]

ThoraxSize = DIST(T10,C7)
ThoraxScale = {1,1,1}
ThoraxShift = {0,0,0}
ENDIF

{*========ANATOMY REFERENCE FRAME ========*}

{* Define antomical reference frame 'Anatomy' to enable patient orientation in the
laboratory to be calculated *}
{* The patient should be aligned along one of the axis of the laboratory reference
frame *}
{* Automatically detect patient orientation in laboratory and fix to the nearest
orthoganal axis of laboratory*}
{* Only calculated if thorax segmenet is present *}
{*  When correct, the blue axis is perpendicular to the floor, the red axis points
in the direction the subject
 is facing, and the green axis points to towards the subjects left side *}

IF EXISTATALL(CLAV)

ThoraxAngles = <Thorax, Global,xzy>
Rotation = -3(ThoraxAngles)

output (Rotation)

             If (Rotation > -45) AND (Rotation <= 45) Then
                    Anatomy = Global
                    $Position = 1
             ElseIf (Rotation > 45) AND (Rotation <= 135) Then
                    Anatomy = ROT(Global, 2(Global),-90)
                    $Position = 2
             ElseIf (Rotation > 135) OR (Rotation <= -135) Then
                    Anatomy = ROT(Global, 2(Global),180)
                    $Position = 3
             ElseIf  (Rotation > -135) AND (Rotation <= -45) Then
                    Anatomy = ROT(Global, 2(Global),90)
                    $Position = 4
             EndIf

       AnatomySize = 100
       AnatomyScale = {3,4,5}
       AnatomyShift = {0,0,0}

       {* Write subject orientation to MP file*}

       PARAM($Position)
ENDIF
```

```
{*=====Upper Arm Segment====*}

OptionalPoints(LSHO,RWRR,RWRU)
IF EXISTATALL(LSHO,RSHO)
{*Calculate a basic shoulder joint centre offset from acromium marker according to
Rab, G., Petuskey, K., & Bagley, A. (2002). A method for determination of upper
extremity kinematics. Gait & Posture, 15(2), 113-119. SJC = 17% of shoulder girdle
width inferior to the acromium marker *}

       ISHO = DIST(LSHO,RSHO)
       $ShoulderOffset = (ISHO*0.17)+($MarkerDiameter/2)
       PARAM($ShoulderOffset)
       RElbowWidth = DIST(RELM,RELL)
       $RElbowOS = RElbowWidth/2
       PARAM($RElbowOS)

RSJC = RSHO + ({0, -$ShoulderOffset, 0}*Attitude(Thorax))
OUTPUT(RSJC)


{*Calculate elbow and wrist joint centres as the mid point between the lateral and
medial joint markers*}
REJC = (RELM+RELL)/2
output(REJC)

RWJC = (RWRR+RWRU)/2
Output(RWJC)

UpperArmLength = dist(RSHO,REJC)
ForeArmLength = dist(REJC,RWJC)
$ArmLength = UpperArmLength + ForeArmLength
PARAM($ArmLength)

{* Model elbow as a revolute jointhinge joint*}
{* Origin: REJC; Y axis: from REJC to RSJC; Z axis: from ELL to EJC, X axis follows
*}

RHumerus = [REJC,RSJC-REJC,REJC-RELL,yzx]

RHumerusSize = DIST(REJC,RSJC)
RHumerusScale = {1,1,1}
RHumerusShift = {0,0,0}

ENDIF

{*======Forearm Segment=======*}
{*============================*}
{* Origin: RWJC; Y axis: from RWJC to REJC; x axis: from RWRU to RWRR; z axis
follows *}
RRadius = [RWJC,REJC-RWJC,RWRU-RWRR,yxz]

RRadiusSize = DIST(REJC,RWJC)
RRadiusScale = {1,1,1}
RRadiusShift = {0,0,0}


{*---------------------------------------- DRAW AXES ----------------------------
------------------*}

{*DrawBone(Anatomy,AMY)

IF EXISTATALL(LSHO,RSHO)
DrawBone(Thorax,TRX)
DrawBone(LHumerus,LHU)
DrawBone(RHumerus,RHU)
ENDIF
DrawBone(LRadius,LRA)
DrawBone(RRadius,RRA)
DrawBone(LHand,LHN)
DrawBone(RHand,RHN)*}
```

Dynamic Code for Human Participants

```
{*---------------------------------- START OF MACRO SECTION ----------------------
------------------*}

macro DRAWBONE(Bone,BoneLabel)
{*Outputs segment definition markers in Polygon format*}
LL = Bone#Size
DD = LL/10
WW = DD
BoneLabel#O = 0(Bone)+LL*Bone#Shift*Attitude(Bone)
BoneLabel#P = BoneLabel#O+LL*2(Bone#Scale)*2(Bone)
BoneLabel#A = BoneLabel#O+DD*3(Bone#Scale)*3(Bone)
BoneLabel#L = BoneLabel#O+WW*1(Bone#Scale)*1(Bone)
OUTPUT(BoneLabel#O,BoneLabel#P,BoneLabel#A,BoneLabel#L)
endmacro

{*---------------------------------- CREATE VIRTUAL MARKERS ----------------------
------------------*}

{* Define the segment that was used to calculate the position vector of the missing
marker *}

       ThoraxCluster=[CHEA,CHEA-CHEC,CHEB-CHEA,yzx]

{* The postion vector %V1 is read in from the parameter file *}

%V1 = {$%STRNLocalx,$%STRNLocaly,$%STRNLocalz}
%V2 = {$%T10Localx,$%T10Localy,$%T10Localz}
%V3 = {$%C7Localx,$%C7Localy,$%C7Localz}

{* Recreate the missing marker using the postion vector *}

STRN = (CHEA/ThoraxCluster + %V1)*ThoraxCluster
T10 = (CHEA/ThoraxCluster + %V2)*ThoraxCluster
C7 = (CHEA/ThoraxCluster + %V3)*ThoraxCluster

{* Output the trajectory of the missing marker to the C3D file *}

OUTPUT(STRN)
OUTPUT(T10)
OUTPUT(C7)


{* -----------Create position of ELM markers------------------------------ *}

{* Recreate ELM markers relative to the local reference frame of the upper arm
Clusters and lateral
elbow marker (ELL) if ELM are obstructed *}

OptionalPoints (RELM,RWRR,RWRU,LSHO)


If EXISTATALL(RELM) Then
       RELM_Obstructed = 0
       Else
       RELM_Obstructed = 1
ENDIF

       RightArm=[RUPA,RUPA-RUPB,RUPA-RELL,yzx]

{* The postion vector %LA and %RA is read in from the parameter file *}

%RA = {$%RELMLocalx,$%RELMLocaly,$%RELMLocalz}

RELM_temp = (RUPA/RightArm + %RA)*RightArm


{*Add in VIRTUAL POINTS to fill gaps*}
IF RELM_Obstructed == 1
```

```
RELM = RELM_temp
ENDIF

OUTPUT(RELM)

{*---------------------- DEFINE SEGMENTS ----------------------------------*}

{* Global reference frame at origin *}

{*Set Deadband*}
Deadband = $Deadband

Gorigin = {0,0,0}
Global = [Gorigin,{0,0,1},{0,-1,0},yxz]

{*=====Thorax segment=====*}
{*========================*}

UThorax = (C7+CLAV)/2
LThorax = (T10+STRN)/2
ThoraxCentre = LThorax
Thorax = [LThorax,UThorax-LThorax,T10-STRN,yxz]

ThoraxSize = DIST(T10,C7)
ThoraxScale = {1,1,1}
ThoraxShift = {0,0,0}

{*========ANATOMY REFERENCE FRAME ========*}

{* Read-in patient orientation from MP file, calculated during static trial*}

       If     $Position == 1 Then
                     Anatomy = Global
       ElseIf $Position == 2 Then
                     Anatomy = ROT(Global, 2(Global),-90)
       ElseIf $Position == 3 Then
                     Anatomy = ROT(Global, 2(Global),180)
       ElseIf  $Position == 4 Then
                     Anatomy = ROT(Global, 2(Global),90)
       EndIf

AnatomySize = 100
AnatomyScale = {3,4,5}
AnatomyShift = {0,0,0}

{*=====Upper Arm Segment====*}

RSJC = RSHO + ({0, -$ShoulderOffset, 0}*Attitude(Thorax))
OUTPUT(RSJC)

{*Calculate elbow and wrist joint centres as the mid point between the lateral and
medial joint markers*}
REJC = (RELM+RELL)/2
RWJC = (RWRR+RWRU)/2

{*Origin: REJC;Y axis: from REJC to RSJC; Z axis:from ELL to EJC, X axis follows *}

RHumerus = [REJC,RSJC-REJC,REJC-RELL,yzx]

RHumerusSize = DIST(REJC,RSJC)
RHumerusScale = {1,1,1}
RHumerusShift = {0,0,0}

{*======Forearm Segment=======*}

{* Origin: RWJC; Y axis: from RWJC to REJC; Z axis: from RWRU to RWRR; X axis
follows *}

RRadius = [RWJC,REJC-RWJC,RWRU-RWRR,yzx]

RRadiusSize = DIST(REJC,RWJC)
```

```
RRadiusScale = {1,1,1}
RRadiusShift = {0,0,0}

{*==========DUMMY Forearm Segments=======*}
{*Creates 2 new forearm segments using only the elbow markers and wrist markers*}
{* different axis convention:
WE:Origin: RWJC; Y axis: from LWRR to LWRU; Z axis: from LWJC to LEJC; X axis
follows
EW:Origin: REJC; Y axis: from LELM to LELL; Z axis: from LWJC to LEJC; X axis
follows *}

{*elbow to wrist segment denoted EW*}
{*Wrist to elbow segment denoted WE*}

RRadiusEW = [RWJC,RELM-RELL,RWJC-REJC,xzy]
RRadiusWE = [RWJC,RWRU-RWRR,RWJC-REJC,xzy]

RRadiusEWSize = DIST(REJC,RWJC)
RRadiusEWScale = {1,1,1}
RRadiusEWShift = {0,0,0}

RRadiusWESize = DIST(REJC,RWJC)
RRadiusWEScale = {1,1,1}
RRadiusWEShift = {0,0,0}

{*------------------------ DRAW AXES ---------------------------------*}

DrawBone(Anatomy,AMY)
DrawBone(Thorax,TRX)
DrawBone(RHumerus,RHU)
DrawBone(RRadius,RRA)

{*---------------------------- JOINT ANGLES ---------------------------------*}

{*=======Thorax=======*}

LThoraxAngles = <Thorax, Anatomy,xzy> {* Euler angles sequence: XZY. Flexion-
extension, ab-adduction, internal-external rotation*}
LThoraxAngles = <LThoraxAngles(1),-LThoraxAngles(2),-LThoraxAngles(3)>
RThoraxAngles = <LThoraxAngles(1),LThoraxAngles(2),-LThoraxAngles(3)>

{*=======Shoulders=======*}

RShoulderAngles = <Thorax,RHumerus,xzy>
RShoulderAngles = <RShoulderAngles(1),-RShoulderAngles(2),-RShoulderAngles(3)>

{*========Elbows========*}

RElbowAngles = <RHumerus,RRadius,xzy>   {* Euler angles sequence: xzy. Flexion-
extension, ab-adduction, internal-external rotation*}

RElbowAngles = <RElbowAngles(1),-RElbowAngles(2),RElbowAngles(3)+90>

IF RElbowAngles(3)>200
       RElbowAngles = <RElbowAngles(1),RElbowAngles(2),RElbowAngles(3)-360>
ENDIF

{*=======SUPINATION======*}

RSupination = <RRadiusEW,RRadiusWE, xzy>

RSupination = <RSupination(1),-RSupination(2),RSupination(3)+90>

OUTPUT(RThoraxAngles)
OUTPUT(RShoulderAngles)
OUTPUT(RElbowAngles)
OUTPUT(RSupination)
```

Static Code for Humanoid Arm

```
{*-------------------- START OF MACRO SECTION --------------------------------*}

macro DRAWBONE(Bone,BoneLabel)
{*Outputs segment definition markers in Polygon format*}
LL = Bone#Size
DD = LL/10
WW = DD
BoneLabel#O = 0(Bone)+LL*Bone#Shift*Attitude(Bone)
BoneLabel#P = BoneLabel#O+LL*2(Bone#Scale)*2(Bone)
BoneLabel#A = BoneLabel#O+DD*3(Bone#Scale)*3(Bone)
BoneLabel#L = BoneLabel#O+WW*1(Bone#Scale)*1(Bone)
OUTPUT(BoneLabel#O,BoneLabel#P,BoneLabel#A,BoneLabel#L)
endmacro

{*------------------------- CREATE VIRTUAL MARKERS ---------------------------*}


{* Define the segment that was used to calculate the position vector of the missing
marker *}

       ThoraxCluster=[CHEA,CHEA-CHEC,CHEB-CHEA,yzx]



{* ------------------------Calculate position of ELM marker-------------------- *}

{* Calculate the position vector of the medial elbow marker (ELM) relative to the
local reference
frame of the upper arm Clusters and lateral elbow marker (ELL)*}

{* Cluster markers are called UPA, UPB, UPC, UPD *}

       RightArm=[RUPA,RUPA-RUPB,RUPA-RELL,yzx]

$%RELM = RELM/RightArm

{* $%RELM are converted into its three orthogonal coordinates
- this format is needed to save as a parameter in the MP file *}

$%RELMLocalx = $%RELM(1)
$%RELMLocaly = $%RELM(2)
$%RELMLocalz = $%RELM(3)

{* $%LELM and $%RELM is written to the mp file *}

PARAM($%RELMLocalx,$%RELMLocaly,$%RELMLocalz)

{*-------------------- DEFINE SEGMENTS -------------------------------*}

{* Global reference frame at origin *}

Gorigin = {0,0,0}
Global = [Gorigin,{0,0,1},{0,-1,0},yxz]
{*
GlobalSize = 100
GlobalScale = {3,4,5}
GlobalShift = {0,0,0}
DrawBone(Global, GLO)
*}
{*=====Thorax segment=====*}

IF EXISTATALL(CLAV)
{* Run after creating the virtual markers STRN & T10 *}

UThorax = (C7+CLAV)/2
LThorax = (T10+STRN)/2
ThoraxCentre = LThorax
```

```
Thorax = [LThorax,UThorax-LThorax,T10-STRN,yxz]

ThoraxSize = DIST(T10,C7)
ThoraxScale = {1,1,1}
ThoraxShift = {0,0,0}
ENDIF

{*========ANATOMY REFERENCE FRAME ========*}

{* Define antomical reference frame 'Anatomy' to enable patient orientation in the
laboratory to be calculated *}
{* The patient should be aligned along one of the axis of the laboratory reference
frame *}
{* Automatically detect patient orientation in laboratory and fix to the nearest
orthoganal axis of laboratory*}
{* Only calculated if thorax segmenet is present *}
{*  When correct, the blue axis is perpendicular to the floor, the red axis points
in the direction the subject
 is facing, and the green axis points to towards the subjects left side *}

IF EXISTATALL(CLAV)

ThoraxAngles = <Thorax, Global,xzy>
Rotation = -3(ThoraxAngles)

output (Rotation)

              If (Rotation > -45) AND (Rotation <= 45) Then
                     Anatomy = Global
                     $Position = 1
              ElseIf (Rotation > 45) AND (Rotation <= 135) Then
                     Anatomy = ROT(Global, 2(Global),-90)
                     $Position = 2
              ElseIf (Rotation > 135) OR (Rotation <= -135) Then
                     Anatomy = ROT(Global, 2(Global),180)
                     $Position = 3
              ElseIf  (Rotation > -135) AND (Rotation <= -45) Then
                     Anatomy = ROT(Global, 2(Global),90)
                     $Position = 4
              EndIf

       AnatomySize = 100
       AnatomyScale = {3,4,5}
       AnatomyShift = {0,0,0}

       {* Write subject orientation to MP file*}

       PARAM($Position)
ENDIF

{*=====Upper Arm Segment====*}
OptionalPoints(LSHO,RWRR,RWRU)

IF EXISTATALL(LSHO)

       $ShoulderOffset = 35
       PARAM($ShoulderOffset)
       RElbowWidth = DIST(RELM,RELL)
       $RElbowOS = RElbowWidth/2
       PARAM($RElbowOS)


RSJC = RSHO + ({0, -$ShoulderOffset, 0}*Attitude(Thorax))
OUTPUT(RSJC)

{*Calculate elbow and wrist joint centres as the mid point between the lateral and
medial joint markers*}
REJC = (RELM+RELL)/2
output(REJC)

{* Model elbow as a revolute jointhinge joint*}
```

```
{* Origin: REJC; Y axis: from REJC to RSJC; Z axis: from ELL to EJC, X axis follows
*}

RHumerus = [REJC,RSJC-REJC,REJC-RELL,yzx]

RHumerusSize = DIST(REJC,RSJC)
RHumerusScale = {1,1,1}
RHumerusShift = {0,0,0}

ENDIF

{*-------------------- DRAW AXES -------------*}

{*DrawBone(Anatomy,AMY)

IF EXISTATALL(RSHO)
DrawBone(Thorax,TRX)
DrawBone(RHumerus,RHU)
ENDIF
DrawBone(RRadius,RRA)
*}
```

Dynamic Code for Humanoid Arm

```
{*------------------ START OF MACRO SECTION ----------------------*}

macro DRAWBONE(Bone,BoneLabel)
{*Outputs segment definition markers in Polygon format*}
LL = Bone#Size
DD = LL/10
WW = DD
BoneLabel#O = 0(Bone)+LL*Bone#Shift*Attitude(Bone)
BoneLabel#P = BoneLabel#O+LL*2(Bone#Scale)*2(Bone)
BoneLabel#A = BoneLabel#O+DD*3(Bone#Scale)*3(Bone)
BoneLabel#L = BoneLabel#O+WW*1(Bone#Scale)*1(Bone)
OUTPUT(BoneLabel#O,BoneLabel#P,BoneLabel#A,BoneLabel#L)
endmacro

{*----------------------- CREATE VIRTUAL MARKERS -------------------------*}

{* Define the segment that was used to calculate the position vector of the missing
marker *}

       ThoraxCluster=[CHEA,CHEA-CHEC,CHEB-CHEA,yzx]

{* The postion vector %V1 is read in from the parameter file *}

%V1 = {$%STRNLocalx,$%STRNLocaly,$%STRNLocalz}
%V2 = {$%T10Localx,$%T10Localy,$%T10Localz}
%V3 = {$%C7Localx,$%C7Localy,$%C7Localz}

{* Recreate the missing marker using the postion vector *}

STRN = (CHEA/ThoraxCluster + %V1)*ThoraxCluster
T10 = (CHEA/ThoraxCluster + %V2)*ThoraxCluster
C7 = (CHEA/ThoraxCluster + %V3)*ThoraxCluster

{* Output the trajectory of the missing marker to the C3D file *}

OUTPUT(STRN)
OUTPUT(T10)
OUTPUT(C7)


{* --------------Create position of ELM markers------------------ *}

{* Recreate ELM markers relative to the local reference frame of the upper arm
Clusters and lateral
elbow marker (ELL) if ELM are obstructed *}
```

```
OptionalPoints (RELM,RWRR,RWRU,LSHO)

If EXISTATALL(RELM) Then
       RELM_Obstructed = 0
       Else
       RELM_Obstructed = 1
ENDIF

       RightArm=[RUPA,RUPA-RUPB,RUPA-RELL,yzx]

{* The postion vector %LA and %RA is read in from the parameter file *}

%RA = {$%RELMLocalx,$%RELMLocaly,$%RELMLocalz}

RELM_temp = (RUPA/RightArm + %RA)*RightArm

{*Add in VIRTUAL POINTS to fill gaps*}
IF RELM_Obstructed == 1
       RELM = RELM_temp
ENDIF

OUTPUT(RELM)

{*---------------------- DEFINE SEGMENTS ------------------------*}

{* Global reference frame at origin *}

{*Set Deadband*}
Deadband = $Deadband

Gorigin = {0,0,0}
Global = [Gorigin,{0,0,1},{0,-1,0},yxz]

{*=====Thorax segment=====*}

UThorax = (C7+CLAV)/2
LThorax = (T10+STRN)/2
ThoraxCentre = LThorax
Thorax = [LThorax,UThorax-LThorax,T10-STRN,yxz]

ThoraxSize = DIST(T10,C7)
ThoraxScale = {1,1,1}
ThoraxShift = {0,0,0}

{*========ANATOMY REFERENCE FRAME ========*}

{* Read-in patient orientation from MP file, calculated during static trial*}

       If     $Position == 1 Then
                     Anatomy = Global
       ElseIf $Position == 2 Then
                     Anatomy = ROT(Global, 2(Global),-90)
       ElseIf $Position == 3 Then
                     Anatomy = ROT(Global, 2(Global),180)
       ElseIf  $Position == 4 Then
                     Anatomy = ROT(Global, 2(Global),90)
       EndIf

AnatomySize = 100
AnatomyScale = {3,4,5}
AnatomyShift = {0,0,0}

{*=====Upper Arm Segment====*}

RSJC = RSHO + ({0, -$ShoulderOffset, 0}*Attitude(Thorax))
OUTPUT(RSJC)

{*Calculate elbow and wrist joint centres as the mid-point between the lateral and
medial joint markers*}
REJC = (RELM+RELL)/2
```

```
{*Origin: REJC; Y axis:from REJC to RSJC;Z axis: from ELL to EJC, X axis follows *}

RHumerus = [REJC,RSJC-REJC,REJC-RELL,yzx]
RHumerusSize = DIST(REJC,RSJC)
RHumerusScale = {1,1,1}
RHumerusShift = {0,0,0}

{*-------------------- DRAW AXES ------------------------*}

DrawBone(Anatomy,AMY)
DrawBone(Thorax,TRX)
DrawBone(RHumerus,RHU)

{*------------------------- JOINT ANGLES -----------------------------*}

{*=======Thorax=======*}

LThoraxAngles = <Thorax, Anatomy,xzy> {* Euler angles sequence: XZY. Flexion-
extension, ab-adduction, internal-external rotation*}
LThoraxAngles = <LThoraxAngles(1),-LThoraxAngles(2),-LThoraxAngles(3)>
RThoraxAngles = <LThoraxAngles(1),LThoraxAngles(2),-LThoraxAngles(3)>

{*=======Shoulders=======*}

RShoulderAngles = <Thorax,RHumerus,xzy>
RShoulderAngles = <RShoulderAngles(1),-RShoulderAngles(2),-RShoulderAngles(3)>

OUTPUT(RThoraxAngles)
OUTPUT(RShoulderAngles)
```

Appendix B. Pipeline for Collection and Analysis of Motion Study Data

The steps taken for data acquisition and analysis in Chapter 4 have been summarised in this appendix.

I. Setting up the system

- Switch on desktop/cameras/ Vicon Giganet
- Connect network cable to research PC
- Perform camera calibration
- Set volume origin
- Quality assurance check (less than 2 mm error)

II. Subject preparation

- Have participant read information sheet and sign consent form
- Perform subject measurement
- Place markers according to protocol
- Check alignment/marker misplacement

III. Data collection (Nexus)

- Create subjects and sessions in data management/ subject template selection in Nexus
- Static trial collection x1 per task
- Dynamic trial collection x 1 per task
- Quality check to ensure trials are adequate

IV. Post-collection kinematic processing (Nexus)

- Label subjects according to the marker protocol
- Fill marker gaps and filter data
- Construct markers in STRN, C7, and T10 positions
- Run dynamic trial pipeline to obtain shoulder abduction angles, speeds and accelerations
- Export data as .csv and .c3d

V. Post-collection kinetic processing (AMS)

- Import kinematic data into AMS as .c3d files using the "AnyMoCap" application
- Enter height and weight to scale shoulder model for participant anthropometry
- Disable legs and left arm in body model; hardcode initial pelvis position, add driver for pelvis to compensate for markers not being placed on pelvis
- Perform parameter optimisation
- Perform inverse dynamics to obtain muscle forces
- Export muscle force, GH joint reaction force, and joint moment data as .csv and .c3d

Appendix C. Evaluation of MSK Model

Purpose

Evaluation and validation are important for developing useful and accurate models. To do this, three different approaches are typically used: direct validation, indirect validation, and trend analysis [216]. Direct validation involves comparison of model outputs with experimentally measured values for the variable of interest. Given that it is not currently possible to directly measure muscle forces during task completion, indirect validation – the use of a proxy variable that can be experimentally measured – is a popular strategy in MSK modelling. This is most commonly done using EMG [181, 216, 250]. In addition to evaluating whether a model's outputs qualitatively and quantitatively match with predicted results, it is also important to analyse trends in model outputs to ensure that the model is using reasonable assumptions and that model parameters interact appropriately with each other. This appendix provides a discussion of the MSK model used for estimating supraspinatus muscle forces and explores the effect of changing muscle recruitment algorithms in the AMS model. Muscle force estimates from other rotator

cuff muscles, the lateral segment of the deltoid, GH joint reaction forces, and GH joint moments during task completion have also been included in this section.

Analysis and Presentation of Data

The Pearson-D'Agostino test was used to evaluate the normality [220]. Data obtained from the MSK model were found to be normally distributed. Data in this section are therefore presented as mean and standard deviation (SD). For statistical comparison, *t*-tests were used.

Muscle Model and Recruitment Algorithm

It is important to use an appropriate model to reasonably approximate internal loading and force distribution across muscles during task completion. Like many MSK models, the AMS does not attempt to directly replicate the physiologic cross-bridge activity of muscles proposed in the Huxley Muscle Model, given that this would not be computationally efficient and may lead to unstable numerical solutions [183, 185]. Furthermore, a Huxley Muscle model would require detailed physiological input data which were not available from this study. Instead, inverse dynamics modelling systems such as the AMS tend to use phenomenological models based on the Hill Muscle Model, which describe muscles as contractile elements in combination with a number of elastic elements [184]. The muscle model used in this study therefore used a simple phenomenological model based on the Hill Model.

To select the appropriate recruitment pattern for muscles in this application, a balance was chosen between physiologic relevance and computational efficacy. In the AMS system, "polynomial muscle recruitment is described as an optimisation of the form:

subject to the equilibrium equation: $Cf = r$ (1)

minimise $G(f^m)$: $G = \sum_i^{n^m} \left(\frac{f_i^{(m)}}{N_i} \right)^p$ (2)

with: $f_i^m \geq 0, i = 1 \dots n^m$ (3)

where **f** is a vector of muscle and joint forces, **r** is a vector representing external and inertial forces, and **C** is a matrix of equation coefficients" [185]. In this optimisation, $\mathbf{f_i^{(m)}}$ and $\mathbf{N_i}$ represent the force and strength of the i-th muscle, respectively, and **G** represents the objective function that attempts to be minimised. As denoted by equation 3, only tensile forces are produced by muscles in this model. The power of the objective function, or **p** corresponds to the synergy of muscle recruitment within a model, whereby a value of 1 results in no synergy (i.e. the strongest muscle completes the activity alone) and a value approaching ∞ results in very high muscle synergy. Greater synergy corresponds to more efficient energy usage across the system.

While it may be desirable to arbitrarily use a high muscle power given that human muscle recruitment demonstrates coordinated synergy, use of high power in the recruitment function can be physiologically unrealistic. As described within the AMS: "[At high powers] some of the activations and de-activations of the muscles happen very quickly and perhaps faster than living muscles can manage. Muscle contraction is an electro-chemical process, and it takes some time to develop and release force in a muscle. The actual time depends somewhat on the circumstances and on the fibre composition in the muscle, but the time is finite and contraction or relaxation cannot physiologically happen in an instant. In consideration of this physiologic limitation, the power of 5 is the upper limit of the polynomial criterion in AnyBody. [185]." In addition to limitations in physiologic muscle contraction speed, it is also worth noting that higher powers in muscle recruitment are more computationally expensive. Given that there are benefits and drawbacks to changing the muscle recruitment algorithm, experimentation and good judgment are required to determine an appropriate power for the task being modelled [185]. The standard muscle recruitment pattern within the AMS is a cubic function (i.e. $\mathbf{p} = 3$). To investigate the effect of increasing and decreasing the synergy of muscle recruitment within the system, a sensitivity analysis was conducted to determine how increasing and decreasing synergy within the MSK model affects supraspinatus muscle force estimates during task completion.

Qualitative interpretation of Figure 35 shows that while each recruitment algorithm has the same trend , higher order muscle recruitment synergy corresponds to a greater force being distributed to the supraspinatus. While a relatively large difference exists between the 2nd order recruitment algorithm and the default 3rd order recruitment algorithm, there is a much smaller gap between values from the 3rd order algorithm and the 4th order recruitment algorithm.

Differences in supraspinatus muscle forces are quantitatively explored in Figure 36 and Table 18. While the 4th order recruitment algorithm's peak and average values appear to be slightly higher than the default 3rd order recruitment algorithm, the difference between values calculated using both methods were found to not be statistically significant (p=0.99 for average values and p=0.55 for maximum force values). In contrast, supraspinatus forces from the 2nd order recruitment algorithm were found to be significantly lower than the values output by the 3rd order recruitment pattern (p=0.02 for average values and p=0.01 for peak values). Given these differences, it was decided to use the default 3rd order muscle recruitment algorithm for this motion study.

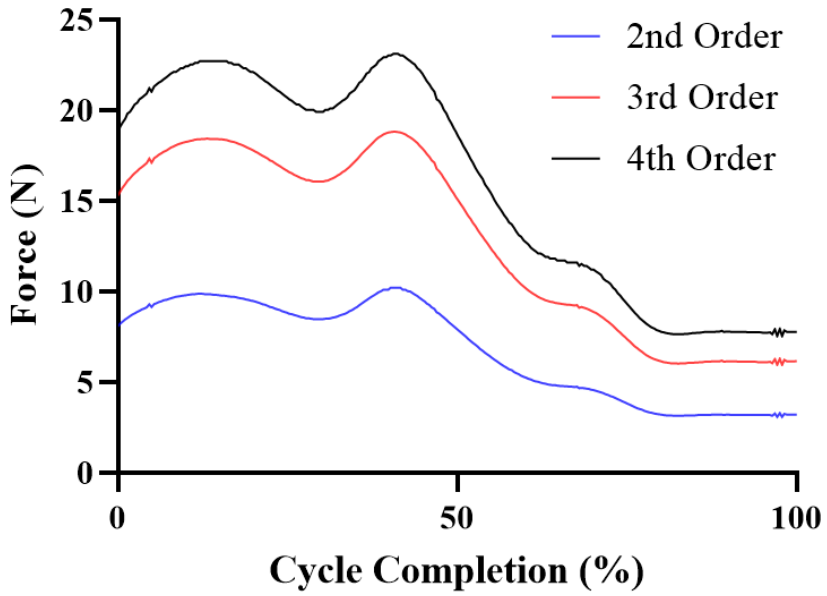


Figure 35: Differences in supraspinatus muscle force during task completion based upon muscle recruitment synergy throughout task completion. The 2nd order is quadratic a recruitment pattern (p=2), 3rd order is cubic (p=3) and 4th order quartic

(p=4) muscle recruitment. Higher power indicates greater synergy in load distribution between the supraspinatus muscle and surrounding shoulder muscles.

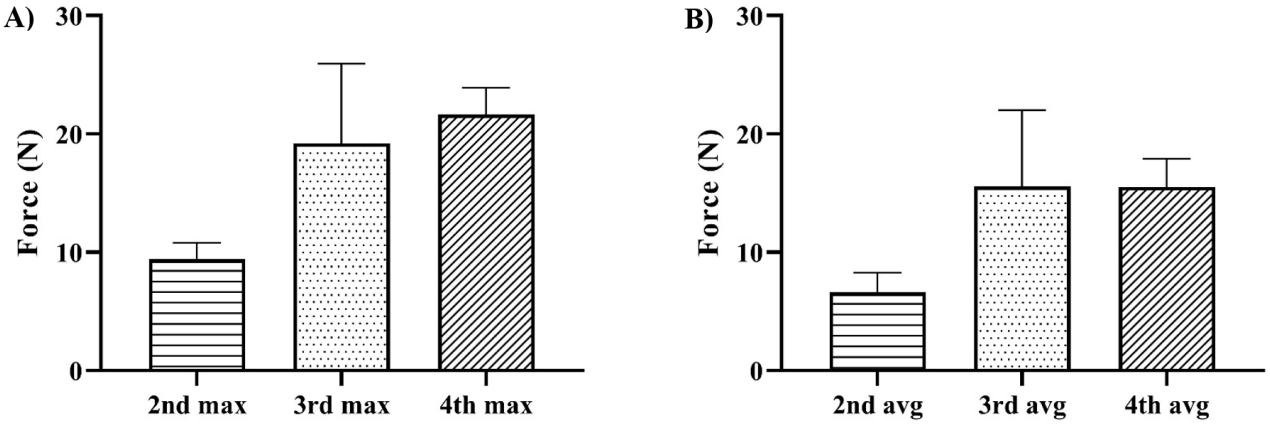


Figure 36: Supraspinatus muscle force as a function of muscle recruitment synergy during task completion. A). Represents average force values from the task cycle. B). Represents peak force values from the task cycle. Higher recruitment corresponds to greater synergy in shoulder muscle recruitment for task completion.

Table 18: Differences in peak and average supraspinatus muscle forces as a function of recruitment synergy. Higher order recruitment corresponds to increased synergy in force distribution between shoulder muscles.

Trial	2nd Order Recruitment	3rd Order Recruitment	4th Order Recruitment
Average Force (SD)	6.6 (1.7)	15.6 (6.5)	15.5 (2.4)
Peak Force (SD)	9.4 (1.4)	19.2 (6.7)	21.6 (2.3)

Evaluation of Outputs from MSK Model

GH joint reaction forces and moments obtained from this study have been provided in Table 19 and Table 20, respectively. The magnitude of GH joint moments and reaction forces during abduction/adduction tasks were within the same range as results from previous *in silico* studies [242, 245]. As discussed in Chapter 4, there are few *in vivo* and *in vitro* studies available to directly compare with MSK model data. A landmark study conducted by Bergmann et al. was the first study to measure *in vivo* GH joint reaction forces using load cells embedded in a surgical implant [251]. This study reported peak reaction forces between 375-500 N during abduction tasks to 90º with no external load [251]. These values are similar to the 345 (SD 56) peak joint reaction force obtained from the AMS model in our study. Consistency

between model results and directly measured *in vivo* data lends support to the validity of the AMS model for providing reasonable joint loading estimates.

Table 19: Peak and average GH joint reaction forces obtained from the AMS during task completion

Joint Reaction Force	30º Abduction	90º Abduction
Average (SD), N	55 (18)	236 (35)
Peak (SD), N	108 (28)	345 (56)

Table 20: Peak and average GH joint moments obtained from the AMS during task completion

Joint Moment	30º Abduction	90º Abduction
Average (SD), N·m	3.13 (0.43)	5.74 (1.10)
Peak (SD), N·m	4.45 (0.50)	8.02 (1.64)

In addition to joint moments and reaction forces, muscle forces for the rotator cuff (i.e. supraspinatus, teres minor, infraspinatus, and subscapularis) and lateral deltoid were obtained. As shown in Table 21, peak and average forces and moments during task completion are consistently higher in the "abduction to 90º" task. This is intuitively expected from studies examining muscle activation and is in line with trends from MSK models which have been previously published in literature [191, 239, 242, 243].

A widely held view is that the supraspinatus is responsible for initiating abduction of the shoulder and that it is the muscle which has greatest activation during this task [37]. Given this view, the results in Table 21 that show relatively similar contributions from the subscapularis and higher force contributions from the infraspinatus compared to the supraspinatus may seem inconsistent with expected results. There are several explanations for this discrepancy, however. Firstly, it is worth noting that muscle activation measured from EMG is a fraction of activation based upon a muscle's maximum voluntary isometric contraction, rather than a direct representation of force contributions from each muscle. It would therefore be logical that because the subscapularis and infraspinatus muscles are larger than the supraspinatus, the magnitude of force provided is larger, even if their proportional contribution is lower. The volume of the supraspinatus is estimated to be approximately one third that of subscapularis and less than half the size of the infraspinatus [252]. Another point worth noting is that the subscapularis and infraspinatus attach anterior and posteriorly to the supraspinatus, respectively [230, 231]. In a task such as abduction, these

muscles' force contributions would likely be used for joint stabilisation rather than contributing to movement, although this cannot be directly confirmed as the AMS does not provide reasonable force direction vectors for the shoulder at this point in time.

Confirming the validity of supraspinatus force estimates from the model is a challenging task, given that these values cannot be readily compared to directly measured *in vivo* data. Using an EMG-based predictive model, Engelhardt et al.'s *in silico* study predicted the peak supraspinatus muscle force to be approximately 20 N for abduction to 30º and 40 N for abduction to 90º [243]. *In vitro* studies have also attempted to characterise supraspinatus forces during abduction tasks. Hughes and An estimated that the maximum supraspinatus force in abduction tasks to 90º would be 40 N, while Wuelker et al.'s study reported supraspinatus forces of less than 20 N for abduction to 30º and 50 (SD 8) N for abduction to 90º [240, 241]. Collectively, these results are systematically higher than the outputs from the AnyBody MSK model, but within a range where the values are comparable. Although the results from the MSK model need to be interpreted with caution and should not be used for clinical decision-making at this point in time, comparison of results from this study with expected findings in literature indicate that the AMS provides supraspinatus force estimates which are useful for comparison with the humanoid robot proposed in our pilot study.

Table 21: Peak and average muscle force estimates obtained from the AMS during task completion

Muscle	30º Abduction		90º Abduction	
	Average (SD), N	Peak (SD), N	Average (SD), N	Peak (SD), N
Teres Minor	0.1 (0.2)	0.2 (0.6)	2.8 (2.6)	8.6 (6.9)
Supraspinatus	15.5 (6.5)	19.2 (6.7)	18.9 (6.3)	25.7 (8.4)
Infraspinatus	18.3 (9.5)	24.3 (9.9)	30.4 (11.2)	43.4 (17.3)
Subscapularis	11.7 (7.2)	15.0 (8.6)	14.6 (7.9)	23.5 (10.5)
Deltoid (L)	58.7 (22.3)	77.3 (24.6)	83.6 (25.6)	107.2 (34.9)